Review Article

Advances by the Marie Curie project TANGO in thermoacoustics

Maria Heckl ⓘ

Abstract

This paper gives an overview of the research performed by the project TANGO – an Initial Training Network (ITN) with an international consortium of seven academic and five industrial partners. TANGO is the acronym for 'Thermoacoustic and Aeroacoustic Nonlinearities in Green combustors with Orifice structures'). The researchers in TANGO studied many of the intricate physical processes that are involved in thermoacoustic instabilities. The paper is structured in such a way that each section describes a topic investigated by one or more researchers. The topics include:

- transition from combustion noise to thermoacoustic instability
- development of an early-warning system by detecting the precursor of an instability
- analytical flame models based on time-lags
- Green's function approach for stability predictions from nonlinear flame models
- intrinsic thermoacoustic modes
- transport phenomena in swirl waves
- model of the flame front as a moving discontinuity
- development of efficient numerical codes for instability predictions
- heat exchanger tubes inside a combustion chamber

A substantial amount of valuable new insight was gained during this four-year project.

1. Introduction

Thermoacoustic instabilities represent a serious problem for combustion-driven devices, such as gas turbine engines and domestic burners. These instabilities can cause intense pressure oscillations, which in turn causes excessive structural oscillations, fatigue and even catastrophic damage to combustor hardware. In recent years, the development of clean combustion systems with reduced pollution of the environment has become a priority; however, such systems are particularly prone to combustion instabilities. There is an urgent need to understand the physical processes that are responsible so that methods to predict and prevent these instabilities can be developed.

The basic mechanism driving a thermoacoustic instability is a feedback between the heat release from a heat source (typically a flame) and the acoustic field in the cavity that houses the heat source. A mutual enhancement of the heat release fluctuations and the acoustic field ensues, resulting in oscillations with growing amplitude. This basic mechanism occurs in tandem with other physical and chemical processes, leading to a complex web of interactions, most of which are nonlinear. Research to

School of Chemical and Physical Sciences, Keele University, Staffordshire, UK

Corresponding author:
Maria Heckl, School of Chemical and Physical Sciences, Keele University, Staffordshire ST5 5BG, UK.
Email: m.a.heckl@keele.ac.uk

unravel this web has been going on intensively for decades. One can get an overview in the review articles,[1–3] in the books,[4,5] and in Culick.[6] However, there are still many open questions. The aim of the network 'Thermoacoustic and Aeroacoustic Nonlinearities in Green combustors with Orifice structures' (TANGO) was to answer a large range of these questions and to develop a large amount of new understanding.

TANGO was a Marie Curie Initial Training Network (http://www.scm.keele.ac.uk/Tango/) coordinated by Maria Heckl at Keele University (UK) and composed of seven universities and five companies throughout Europe and India. During the four years of its lifetime (2012–2016), a total of 15 young researchers were funded by this network. The majority had three-year PhD positions; there were also two post-doctoral researchers and two short-term graduate researchers. Further information about the project participants can be found in the Appendix 1.

The research in TANGO was interdisciplinary and involved numerical, analytical and experimental approaches. It can be roughly divided into two parts: thermoacoustics and aeroacoustics, although there was considerable interaction across this divide. The thermoacoustic research is summarised in the current paper. The companion paper[7] by Lopez Arteaga and Bodén gives an overview over the aeroacoustics research. Both papers draw heavily on the December 2018 issue of the International Journal of Spray and Combustion Dynamics, which features several research papers produced by TANGO members.

Given the number of researchers involved and their various backgrounds, it was inevitable that different notations were used in TANGO. This paper strives to have consistent notation:

- The time dependence is described by $e^{-i\omega t}$ throughout, unless indicated otherwise.
- Field quantities generally have a mean part and a fluctuating part, and the notation for these is as follows: the mean part is denoted by an overbar, the fluctuating part is denoted by a prime (′) in the time domain and by a hat (ˆ) in the frequency domain. To give an example, the total pressure at a point $\mathbf{x}$ and time t is written as $p(\mathbf{x}, t) = \bar{p}(\mathbf{x}) + p'(\mathbf{x}, t)$, where $p'(\mathbf{x}, t)$ is the pressure fluctuation in the time-domain, and $\hat{p}(\mathbf{x}, \omega)$ is its frequency-domain equivalent.
- A list of symbols for commonly used quantities is given at the end of the paper.

The emphasis in this paper is on the physical insight gained by TANGO into thermoacoustic processes. This is described in the next nine sections. Section 2 describes the transitions from combustion noise to thermoacoustic instability and looks at bifurcations in the flame dynamics and in the emitted sound. Section 3 presents a very applied study relevant to annular combustors: by in-situ monitoring, a thermoacoustic instability is detected in its initial stage, before the amplitude has had time to grow to high levels. The purpose of section 4 is to develop analytical flame models based on time-lags; this is motivated by the phenomenon that travelling times of certain disturbances (such as convected vortices or mixture inhomogeneities) play an important role in thermoacoustic instabilities. Section 5 presents a Green's function approach, which is then used for stability predictions with nonlinear flame models; also, a hybrid approach for fast predictions is developed from it. In section 6, several aspects of intrinsic thermoacoustic (ITA) modes are investigated, including the interplay with ordinary thermoacoustic modes and the role of the flame model. Section 7 presents several theoretical studies on transport phenomena occurring in swirl flames, in particular vorticity waves and the propagation of mixture inhomogeneities. In section 8, the flame front is treated as a moving, rather than stationary discontinuity, and the generation of acoustic waves and entropy waves is examined. The aim of the work described in section 9 is to develop an efficient numerical code (based on the Navier–Stokes equations) and to use this code for the prediction of thermoacoustic instabilities. Section 10 focuses on combustion appliances which include not only a heat source (e.g. flame), but also a heat sink (e.g. heat exchanger or HEX for short); it presents a fundamental study into various physical mechanisms involving the HEX, with the ultimate aim to develop strategies that exploit the HEX for instability control. A summary and conclusions are given in section 11. The Appendix 1 gives information about the TANGO fellows (their supervisor, host institution and country, their time in TANGO); it also lists the sections in which the work of the individual fellows is described in the current paper.

2. Transition from combustion noise to thermoacoustic instability

Nonlinear interactions between heat release rate fluctuations and the acoustic field lead to a variety of nonlinear dynamics phenomena. Of particular interest to the TANGO project were bifurcations, i.e. transitions of the thermoacoustic system from one dynamical state to another as a control parameter is varied.

Experimental studies were carried out at IIT Madras on two fundamental test rigs:

- a laminar premixed ducted V-flame, where the position of the flame within the duct was used as bifurcation parameter (section 2.1);

– a combustor with swirl flame and turbulence generator, where the equivalence ratio was used as bifurcation parameter (section 2.2).

2.1. Laminar premixed ducted V-flame – Variation of flame position

Mukherjee et al.[8] performed studies on the experimental set-up (a modified version of the conical flame rig developed originally by Kabiraj et al.[9] at IIT Madras, which i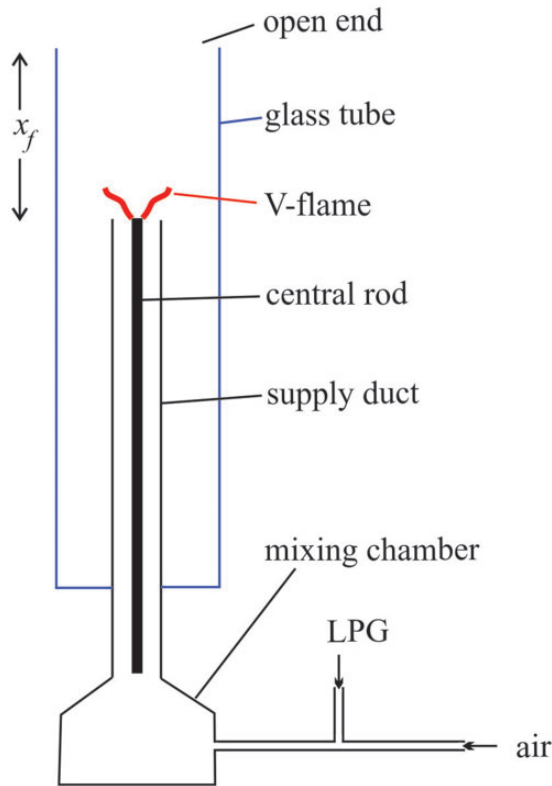s shown in Figure 1. It is effectively a quarter-wave tube with a premixed V-flame. It consists of a vertical glass tube of length $L = 0.75$ m with the bottom end closed and the top end open. Centred on the axis of the glass tube is a narrow premix supply duct, and centred on the supply duct is a solid rod, whose top end acts as the flame holder. The glass tube can be moved up and down with a traverse mechanism, thus changing the axial position of the flame within the glass tube.

The control parameter was the position x_f of the flame, measured from the top of the glass tube. During the experiment, the flame position was moved from the top end to the bottom end of the glass tube in steps of 1 cm, allowing enough time after each step for the tube to settle at a constant temperature. At each position, two types of measurement were acquired:

– The acoustic pressure was recorded as a time history, and from this the root mean square (rms) value of the pressure, p_{rms} was calculated.
– Images of the flame were acquired using a high-speed camera.

The flame passed through several dynamical states on its way; these are listed in Table 1, together with the p_{rms} values.

Figure 2 depicts snapshots of the flame for the limit cycles with low amplitude (Figure 2(a)) and those with high amplitude (Figure 2(b)); the images were taken at 12 equally spaced time instances and cover one cycle of the oscillation. A wave can be seen travelling towards the tip of the flame.

The frequency of the high-amplitude limit cycle experienced a slight decrease as x_f was increased: between $x_f = 44$ and 60 cm, it dropped from about 200 to 184 Hz. This is surprising, given that the size of the hot region downstream of the flame increases as x_f increases, so one would expect a frequency *increase*, rather than a decrease. An explanation for this observation was offered by Sujith:[10] acoustic oscillations are known to enhance transport processes. So

Figure 1. Schematic illustration of the laminar premixed ducted V-flame (after Figure 1(a) in Mukherjee et al.[8]).

Table 1. Dynamical states observed in the flame.

x_f (cm)	p_{rms} (Pa)	Observed flame dynamics
0 . . . 33	<5	**Stable flame**
33 . . . 38	≈15	**Low-amplitude limit cycle** Moderate flame oscillations; flame remains attached to the flame holder (see Figure 2(a))
38 . . . 44	≈15	**Transitional stage** Stronger flame oscillations reminiscent of flapping; flame remains attached to the flame holder
44 . . . 70	100 . . . 150	**High-amplitude limit cycle** Very strong flame oscillations: top part of flame periodically separates from the rest of the flame and then gets extinguished; base of flame periodically lifts off the flame holder and then reattaches (see Figure 2(b))

when the amplitude in the duct increases, the heat transfer from the flame increases; this will lead to lower temperatures, and subsequently to lower natural frequencies.
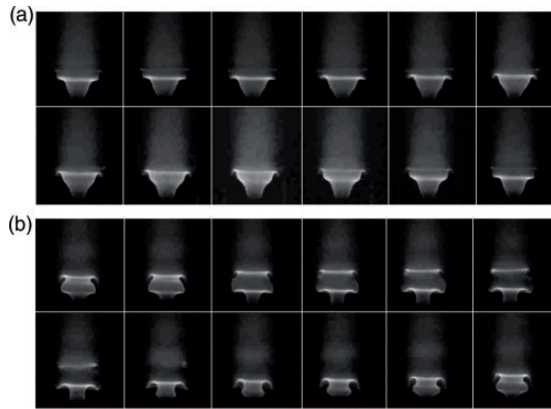

Figure 2. Flame dynamics over one period. (a) Low-amplitude limit cycle; $x_f = 34$ cm (from Figure 7 in Mukherjee et al.[8]) and (b) High-amplitude limit cycle; $x_f = 45$ cm (from Figure 9 in Mukherjee et al.[8]).
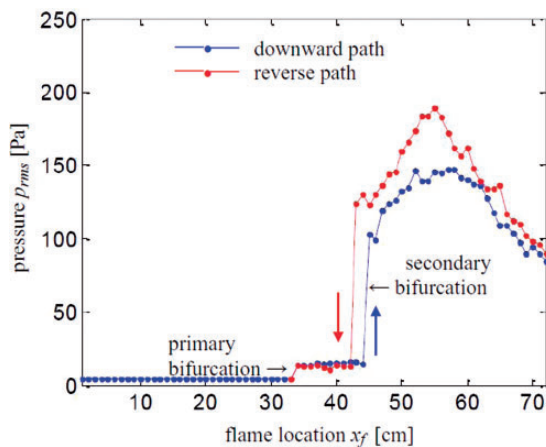

Figure 3. Bifurcation diagram showing the effect of flame location on the rms pressure (from slide 13 in Mukherjee[11]).

After the flame position reached the lowest point ($x_f = 70$ cm) in the glass tube, the movement was then reversed, back towards the top end ($x_f = 0$). Figure 3 shows the bifurcation diagram. Blue markers denote the downward path, and red markers denote the reverse path.

The blue curve in Figure 3 shows two bifurcations:

– at $x_f = 33$ cm (labelled 'primary bifurcation'), there is a sharp transition from the stable state to a low-amplitude limit cycle
– at $x_f = 44$ cm (labelled 'secondary bifurcation'), the transitional state changes abruptly to a high-amplitude limit cycle.

Secondary bifurcations involving large-amplitude limit cycles have been reported in other research areas, for example in mechanical systems;[12] this is the first time they have been observed in thermoacoustics.

Figure 3 also indicates the presence of a hysteresis: along the downward path, the jump between transient state and high-amplitude limit cycle occurs at $x_f = 44$ cm. This jump is delayed, at $x_f = 42$ cm, along the reverse path.

2.2. Combustor with swirl flame and turbulence generator – Variation of equivalence ratio

George et al.[13,14] performed studies on the experimental setup (an adapted version of the test rig originally developed by Komarek and Polifke[15]) shown schematically in Figure 4.

It is a swirl-stabilised turbulent combustor with a backward-facing step. The combustion chamber, which is fitted with quartz windows for optical access, has a length of 1.1 m and a cross-section of 90×90 mm^2. Turbulence is generated not only by the swirler, but also by a flow restrictor just upstream of a contoured nozzle. The flow restrictors block the flow and thus create vortices; these impinge on the
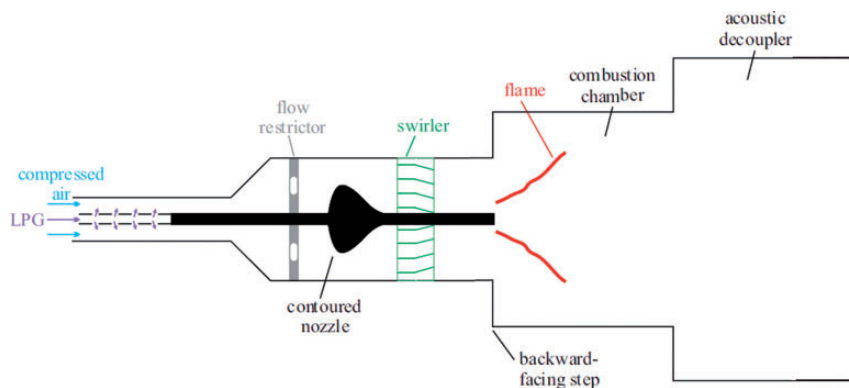

Figure 4. Schematic illustration of the turbulent swirl combustor (not to scale; after Figure 1(a,b) in George et al.[14]).

contoured nozzle and disintegrate into smaller vortices, producing fine-scale turbulence. The turbulence intensity was varied by using different flow restrictors with specific blockage ratios:

1. no blockage (baseline case);
2. turbulence generator with 75% blockage ratio (see Figure 5(a));
3. turbulence generator with 85% blockage ratio (see Figure 5(b)).

The fuel was LPG, and the equivalence ratio ϕ served as bifurcation parameter. This was varied between 0.9 and 0.4 by adjusting the air flow rate.

The dynamical states that were observed are listed in Table 2.

The bifurcation diagram depicting the rms pressure as a function of ϕ for the three turbulence generators is shown in Figure 6. It reveals that the turbulence generators cause an advanced onset of the limit cycle oscillations, but weaken their amplitude.

In order to find an explanation for the effect of the turbulence generators, the distribution of the local Rayleigh index (RI) was measured. The local RI is defined by the time average $\mathrm{RI} = \overline{p'(t)q'(x,y,t)}$, where $p'(t)$ is the acoustic pressure (assumed uniform in the combustion region), and $q'(x, y, t)$ is the local heat release rate, i.e. the rate of heat released by a flame element at position (x, y). The RI represents the acoustic energy gain, averaged over time, due to the interaction between a flame element and the acoustic field. A flame element with positive RI acts as a sound source, and one with a negative RI acts as a sound absorber. Maps of $\mathrm{RI}(x, y)$ were produced from the measurements of $p'(t)$ and $q'(x, y, t)$ (by CH* chemiluminescence); Figure 7 shows the map for $\phi = 0.46$ for the three different turbulence generators.

For the baseline case, the RI is positive in large regions of the combustor. For the two cases with turbulence generator, the regions of positive RI become smaller when compared to the baseline case. The role of the turbulence is to change the spatial distribution of $q'(x, y, t)$, and hence the phase relationship between p' and q'. This weakens the overall strength of the flame as an acoustic source, and as a consequence, the limit cycle amplitudes are lower when turbulence is present.
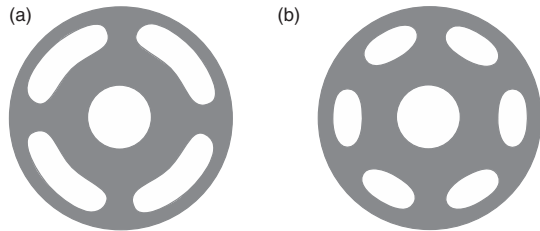

Figure 5. Flow restrictors acting as turbulence generators. (a) 75% blockage ratio and (b) 85% blockade ratio (after Figure 1(c,d) in George et al.[14]).
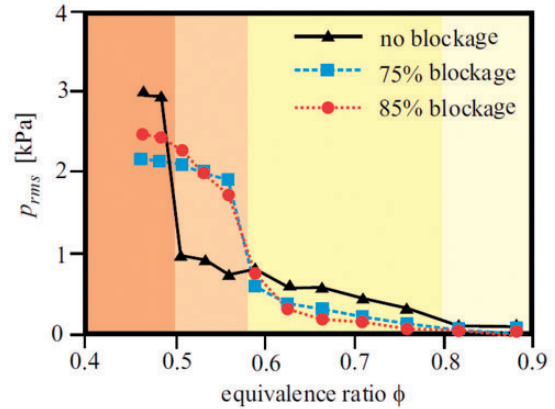

Figure 6. Bifurcation diagram showing the effect of equivalence ratio ϕ on the rms pressure for three flow restrictors: no blockage (black curve), 75% blockage ratio (blue curve), and 85% blockage ratio (red curve; after Figure 3 in George et al.[14]).

Table 2. Dynamical states observed in the turbulent swirl combustor.

| ϕ	Observations
0.89...0.82	**All 3 cases**: aperiodic dynamics; low rms pressure
0.76...0.59	**All 3 cases**: intermittent aperiodic/periodic dynamics
	As ϕ decreases: duration of periodic epochs increases; rms pressure increases slowly
0.56...0.51	**No blockage**: intermittent aperiodic/periodic dynamics
	As ϕ decreases: rms pressure increases slowly
	75% and 85% blockage: periodic oscillations
	As ϕ decreases: rms pressure increases rapidly
0.48...0.46	**All 3 cases**: periodic oscillations (limit cycle); high rms pressure
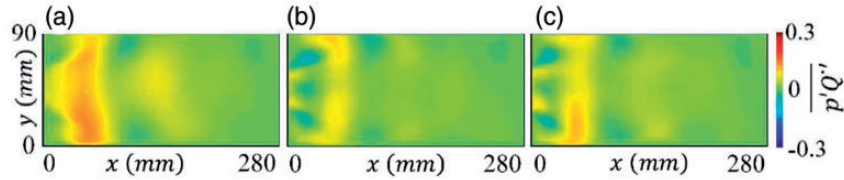
Figure 7. Maps of the local Rayleigh index. (a) No blockage (baseline case), (b) 75% blockage ratio and (c) 85% blockage ratio (from Figure 6 in George et al.[14]).

There is an advanced onset of large amplitude oscillations for cases where the turbulence generator is present. Using spatial variance statistics, George et al.[14] observed that the spatial variance of the instantaneous RI increases in the cases with turbulence generator when compared to the baseline case. The increase in the spatial variance occurs because there are regions in the field of instantaneous RI where the values are different from the mean of the spatial field. This indicates that the coherent spatial structures form earlier in the cases with the turbulence generator when compared to the baseline case. The earlier formation of coherent spatial structures in the field of the RI for the cases with the turbulence generator could be due to the advanced formation of large scale vortices which enhances coherence of the field of the heat release rate.

In a further study, George et al.[16] looked in more detail into the spatio-temporal dynamics of a bluff-body stabilised turbulent combustor. They used an armoury of diagnostic equipment to measure the instantaneous local acoustic power production, $p'(t) q'(x, y, t)$, of the flame, and applied the Mie scattering technique to reveal the interaction of vortices. Three distinctly different dynamical states were induced by adjusting the equivalent ratio:

- combustion noise (disordered dynamics);
- intermittency (epochs of ordered behaviour randomly appearing amidst disordered dynamics);
- thermoacoustic instability (ordered behaviour).

During *combustion noise*, incoherent regions were observed in the field of $p'(t) q'(x, y, t)$; images produced with the Mie scattering technique revealed small-scale vortices perturbing the flame front, causing aperiodic dynamics. During *thermoacoustic instability*, collective interaction of the small-scale vortices led to sustained periodic emergence of large-scale vortex structures. These gave rise to large regions of coherence with substantial values of $p'(t) q'(x, y, t)$, and caused self-sustained periodic pressure oscillations.

Thus, the onset of thermoacoustic instability was described as the emergence of mutually sustained patterns, namely, the standing wave pattern in the acoustic field, the large-scale flow pattern in the flow field, and the localised coherent patterns of the flame.

3. In-situ monitoring of annular thermoacoustic modes

Nonlinear dynamics in combustion systems can be exploited in order to detect an instability *before* the amplitude has reached dangerously high levels.[17] TANGO explored the possibility of detecting an impending instability even earlier, based on *linear* modelling.

The underlying idea, which was first proposed by Lieuwen[18] is this: under stable conditions, any disturbance of the acoustic field dies down; the damping coefficient is positive. In contrast, under unstable conditions, the damping coefficient is negative. Hence the damping coefficient represents a 'stability margin', i.e. it is a measure of how close the thermoacoustic system is to the point where stability gives way to instability. The noise inherent in a combustion system provides ongoing disturbances, which then decay. The decay rates can be ascertained through signal processing of in-situ measurements of the acoustic pressure. Thus they provide a real-time measure for the stability margin before the amplitude starts to grow, and while the thermoacoustic interaction is still linear.

This strategy was adapted by Rouwenhorst et al. to monitor specifically annular combustors, which are commonly found in industrial applications. The work was performed in two parts: first the special features of annular combustion systems were studied (section 3.1), and subsequently, the monitoring strategy was developed (section 3.2).

3.1. Effect of cylindrical symmetry breaking in annular combustion systems

In a *longitudinal* resonator (axial variable x, length L) there are two boundary conditions for the acoustic field: one at the upstream end and one at the downstream end, and thus the field is fully determined. For the basic case of a tube with two open ends, the acoustic pressure at position x and time t is described by the equation

$$p'(x, t) = \left(F e^{im\pi x/L} + F e^{-im\pi x/L} \right) e^{-i\omega_m t} \qquad (1)$$

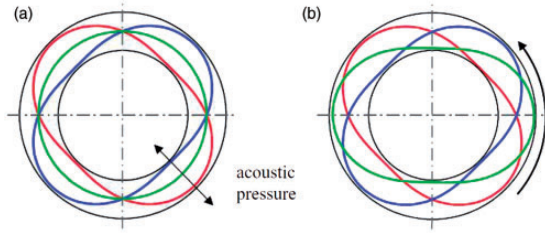where F is an arbitrary amplitude, and $\omega_m = m\pi c/L$ is the resonance frequency.

Figure 8. Waves in annular geometry. The pressure p' of mode 2 is shown at three successive time intervals t_1, t_2, t_3. (a) Standing wave and (b) Travelling wave (from slide 19 in Rouwenhorst et al.[19]).

In an *annular* resonator (azimuthal variable θ, radius a) there is only *one* condition in terms of the variable θ: the acoustic field must be 2π-periodic, $p'(\theta, t) = p'(\theta + 2\pi, t)$, otherwise the field in a given position would not be single-valued. There is no second boundary condition, and as a consequence, the azimuthal dependence is not fully determined. The acoustic pressure is described by the equation

$$p'(x, t) = \left(Fe^{im\theta} + Ge^{-im\theta}\right)e^{-i\omega_m t} \tag{2}$$

where F and G are complex amplitudes, and $\omega_m = mc/a$.

In mathematical terms, one speaks of 'degenerate modes'. The acoustic field can take the form of a standing wave $((|F| = |G|))$, shown in Figure 8(a), a travelling wave ($F = 0$ or $G = 0$; shown in Figure 8(b)), or a combination of both.

Exactly how the solution (2) manifests itself in an annular combustion chamber depends on deviations from the rotational symmetry. Rotational symmetry can be broken by various mechanisms. Within the TANGO project, the focus was on the following two mechanisms:[20]

– symmetry breaking by a heat release rate distribution with non-uniform azimuthal dependence;
– symmetry breaking by an azimuthal bulk flow.

A low-order model was developed with the following assumptions:

– The thermoacoustic feedback is given by a linear relationship between the rate of heat release and the acoustic field.
– The time-scales can be separated into a fast one (acoustic cycle, described by $e^{-i\omega_m t}$) and a slow one (amplitude growth/decay due to thermoacoustic feedback, described by two time-dependent (complex) amplitudes $F(t)$, $G(t)$).

The solution strategy adopted by Rouwenhorst et al.[20] was based on the Rayleigh criterion, from which the following equation was derived

$$\frac{d}{dt}\begin{bmatrix} F \\ G \end{bmatrix} = \mathbf{M}\begin{bmatrix} F \\ G \end{bmatrix} \tag{3}$$

$\mathbf{M}$ is the system matrix; it includes all system parameters (the coupling coefficients describing the thermoacoustic interaction, the azimuthal bulk velocity, the eigenfrequency without thermoacoustic interaction, acoustic attenuation, mode order m and a geometrical non-uniformity parameter). The eigenvalues of the system matrix were calculated, and from these the growth rates and frequency shift (difference in eigenfrequencies with and without thermoacoustic feedback) were deduced. The corresponding eigenvectors, which reveal the mode shape, were also calculated.

It was found that the two mechanisms of symmetry breaking counter-act one another: the θ-dependence of the heat release rate promotes standing wave behaviour, while the azimuthal bulk flow rotates the acoustic field with respect to the coordinate fixed to the combustion chamber.

3.2. In-situ monitoring of decay rates of annular thermoacoustic modes

This section outlines the monitoring strategy described by Rouwenhorst et al.[21–23]

During *stable* operation, combustion noise constantly excites a pair of near-degenerate eigenmodes, and these are typically strongly underdamped, i.e. their damping is *positive*. When the point of marginal stability (i.e. zero damping) is crossed, a transition to limit cycle operation will occur. The decay rates of the modes can therefore serve as stability margin. The monitoring strategy involves N pressure sensors, based at various azimuthal locations in the annular combustion chamber. The sensor data is processed quickly to give the decay rates in real time.

The modelling is based on two equations. The first is

$$\frac{d}{dt}\begin{bmatrix} F \\ G \end{bmatrix} = \mathbf{M}\begin{bmatrix} F \\ G \end{bmatrix} + \mathbf{w}_x \tag{4}$$

this is (3) with an additional forcing term in the form of the vector $\mathbf{w}_x$, which describes the stochastic noise present in a turbulent combustion system. The second equation is

$$\begin{bmatrix} p'(\theta_1) \\ \vdots \\ p'(\theta_N) \end{bmatrix} = \begin{bmatrix} e^{im\theta_1} & e^{-im\theta_1} \\ \vdots & \vdots \\ e^{im\theta_N} & e^{-im\theta_N} \end{bmatrix} \begin{bmatrix} F \\ G \end{bmatrix} + \mathbf{w}_y \tag{5}$$
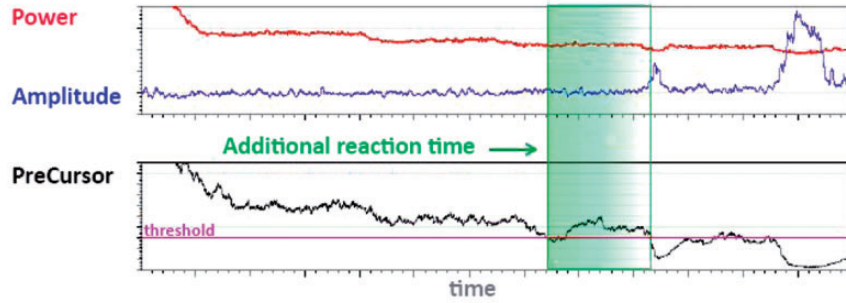
Figure 9. Performance of the IfTA precursor as early warning of an impending instability (after slide 28 in Rouwenhorst et al.[19]).

which describes the measurements of the N pressure sensors at azimuthal locations $\theta_1, \ldots \theta_N$; the vector $\mathbf{w}_y$ represents any measurement noise that might be present.

Equations (4) and (5) can be written more compactly as

$$\dot{\mathbf{x}} = \mathbf{M}\mathbf{x} + \mathbf{w}_x \tag{6a}$$

$$\mathbf{y} = \mathbf{C}\mathbf{x} + \mathbf{w}_y \tag{6b}$$

by using the following terminology: $\mathbf{x}$ is the state vector, $\mathbf{y}$ is the sensor output vector, and $\mathbf{C}$ is the output matrix.

The determination of the decay rates from the sensor data is done in several steps.

1. The sensor data is pre-processed by applying a band-pass filter centred around the frequency of interest and transformed back into the time domain.
2. The filtered signals are sampled at suitable time steps Δt.
3. Equations (6) are discretised with the same time step.
4. Output-only system identification is used to estimate the eigenvalues of the system matrix $\mathbf{M}$, from the discretised versions of (6), i.e. the system matrix is treated effectively as a black box.
5. The decay rate is obtained from the real part of the eigenvalues.

The method has been tested on surrogate data.[22] It has been successfully applied to a laboratory-size annular combustor, where an instability was deliberately induced by varying the equivalence ratio.[23]

Since then it has also been applied to a can-annular industrial-size combustor operated near the stability margin while decreasing its power.[19] Figure 9 shows the time histories of the power, amplitude and 'PreCursor' (a normalised decay rate). A comparison of the amplitude curve and the precursor curve shows that an impending instability is predicted well before

high amplitudes are reached. The method has been patented (filing date: 20 November 2015, patent number EP3104078) and is now marketed as the 'IfTA PreCursor'.

4. Analytical flame models based on time-lag distributions

Analytical studies of thermoacoustic effects require an analytical model for the thermoacoustic interaction. This is often not available, but what is available (from experiments or numerical simulations) is a series of data points for the flame transfer function (FTF); the FTF is a frequency-domain concept and relates oscillations of the heat release rate with oscillations of the flow velocity in the linear domain.

Nonlinear thermoacoustic interactions can be modelled by the flame describing function (FDF), which is an extended version of the FTF in that it depends not only on the frequency, but also on the amplitude of the velocity oscillations. Typically, the FDF is available only for a limited number of frequency and amplitude values.

This section summarises the methods developed in TANGO to construct analytical flame models from data points for the FTF or FDF, both in the time domain and in the frequency domain. The underlying idea is motivated by an effect inherent in most flames: perturbations (e.g. vortex structures), which modulate the flame's heat release rate, arrive at the flame surface over a time interval (rather than in an instant of time), giving rise to a *distribution* of time-lags. This suggests that a flame's heat release rate can be approximated in terms of basis functions (building blocks) in which a time-lag distribution is incorporated.

For the linear case, this will be shown with two types of building blocks: top-hat functions will be used in section 4.1, and Gaussian functions in section 4.2. Section 4.3 treats the nonlinear case and uses building blocks represented by Gaussian functions. The method from section 4.3 is applied in the following section 4.4, to construct an analytical representation for the heat release rate of a swirl flame in a specific laboratory burner.

4.1. Discrete linear flame models

Gopinathan et al.[24,25] presented a systematic method to convert a given FTF into an analytical heat release law in the time-domain. Their starting point was an integral representation of the heat release rate by which the contributions from all possible time-lags are effectively added

$$\frac{Q'(t)}{\bar{Q}} = \frac{1}{\tau_{max}} \int_0^{\tau_{max}} n(\tau) \frac{u'(t-\tau)}{\bar{u}} d\tau \qquad (7)$$

Q' and $\bar{Q}$ are the fluctuating and mean heat release rates, respectively, and u' and $\bar{u}$ are the fluctuating and mean velocities at a fixed position upstream of the flame (the 'reference position', which is commonly taken to be the exit plane). τ is the time-lag, and τ_{max} is the largest time-lag value in the system. n is the coupling coefficient, which is not a constant, but a function of the time-lag; n is real and can be positive or negative. A generic example of the function $n(\tau)$ is shown by the red curve in Figure 10.

The $n(\tau)$ dependence was approximated by a piecewise constant function, shown by the blue curve in Figure 10, where the integration range has been divided into k equal intervals of width $\Delta\tau$, and n takes constant values $n_1, \dots n_k$ in each of these intervals. With this representation for $n(\tau)$, the integral in (7) was approximated by a sum of k integrals

$$\frac{Q'_k(t)}{\bar{Q}} = \frac{1}{\tau_{max}} \left[n_1 \int_0^{\Delta\tau} \frac{u'(t-\tau)}{\bar{u}} d\tau + n_2 \int_{\Delta\tau}^{2\Delta\tau} \frac{u'(t-\tau)}{\bar{u}} d\tau + \cdots \right. $$
$$\left. + n_k \int_{(k-1)\Delta\tau}^{k\Delta\tau} \frac{u'(t-\tau)}{\bar{u}} d\tau \right] \qquad (8)$$

The coupling coefficients, $n_1, n_2, \dots n_k$, were treated as fitting parameters that were determined in the frequency domain. This was done in terms of the FTF, defined by

$$\mathcal{T}(\omega) = \frac{\hat{Q}(\omega)/\bar{Q}}{\hat{u}(\omega)/\bar{u}} \qquad (9)$$

where $\hat{Q}$ and $\hat{u}$ denote the frequency-domain equivalents of $Q'(t)$ and $u'(t)$, respectively. The FTF corresponding to (8) was calculated analytically by Fourier transform; the result was

$$\mathcal{T}_k(\omega) = \frac{1}{\tau_{max}} e^{-i\omega\frac{\Delta\tau}{2}} \frac{2}{\omega} \sin\left(\omega\frac{\Delta\tau}{2}\right) \sum_{j=1}^k n_j e^{ij\omega\Delta\tau} \qquad (10)$$

The fitting parameters $n_1, \dots n_k$ are unknowns that were determined by minimising the discrepancy between the original FTF, $\mathcal{T}(\omega)$, and its approximation $\mathcal{T}_k(\omega)$. Mean square error minimisation led to a linear set of equations for the coupling coefficients, which was solved. Once they were known, the time-domain representation (8) and the frequency-domain representation (9) were fully determined and given in analytical form. The same set of parameters ($n_1, n_2, \dots n_k$) were used in the time-domain representation (8) as well as in the frequency-domain representation (9).

The method was validated by applying it to a conical flame and a V-flame for which the FTF is known (calculated from the G-equation in Schuller et al.[26]). It was shown to be more robust than methods used by earlier researchers to approximate a given FTF by an analytical expression. This is not surprising, given that here the approximation was motivated by physical insight. It was also shown that the distribution $n(\tau)$ is directly proportional to the impulse response (IR) of the flame.

4.2. Continuous linear flame models

The underlying idea was motivated by a physical consideration in the time domain: different types of perturbation in a burner travel with different speeds, and the arrival of each perturbation at the flame front is spread out over time. An example is the swirl burner shown in Figure 13: two types of perturbations emerge from the swirler,

- an acoustic wave, which travels with the speed of sound,
- an inertial wave, which travels more slowly with a speed similar to that of convection.

Both waves travel downstream towards the flame. The acoustic wave arrives well before the inertial wave, and each wave in turn interacts with the flame over a time *interval*, rather than just for an instant of time.
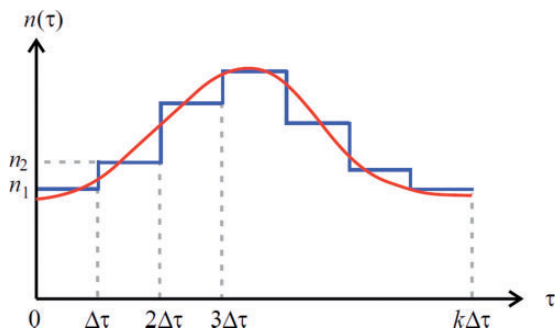

Figure 10. Coupling coefficient as a function of time-lag (red curve) and its piecewise approximation (blue curve; after Figure 2 in Gopinathan et al.[25]).

When calculating the IR from measured FTFs, a typical pattern is found: it looks like a Gaussian curve centred at a particular time-lag, or like a superposition of several Gaussian curves centred at discrete time-lags.

Motivated by this observation, Gopinathan et al.[27] assumed a generic heat release rate law with k discrete time-lags, $\tau_1, \ldots \tau_k$ and with a Gaussian distribution D around each of them

$$
\begin{aligned}
\frac{Q'_k(t)}{\bar{Q}} = n_1 \int_0^\infty \frac{u'(t-\tau)}{\bar{u}} D(\tau - \tau_1) \mathrm{d}\tau + \cdots \\
+ n_k \int_0^\infty \frac{u'(t-\tau)}{\bar{u}} D(\tau - \tau_k) \mathrm{d}\tau
\end{aligned}
\tag{11}
$$

where D is given by

$$
D(\tau - \tau_j) = \frac{1}{\sigma_j \sqrt{2\pi}} \mathrm{e}^{-(\tau-\tau_j)^2/(2\sigma_j^2)}, \quad j = 1, 2, \ldots k
\tag{12}
$$

This heat release rate law contains $3k$ parameters: $n_1, \ldots n_k$, $\tau_1, \ldots \tau_k$, $\sigma_1, \ldots \sigma_k$. They were treated as fitting parameters.

4.3. Amplitude-dependent flame models

Amplitude-dependent flame models are most commonly expressed in terms of a FDF. For a given burner, the FDF can be measured experimentally by the following procedure: the flame is excited with a sound wave of different frequencies ω and velocity amplitudes a, the global heat release rate is measured, and the FDF is determined from

$$
\mathcal{T}(\omega, a) = \frac{\hat{Q}(\omega, a)/\bar{Q}}{\hat{u}(\omega, a)/\bar{u}}
\tag{13}
$$

The FDF can also be determined by numerical simulations in which the experimental procedure described

above is mimicked. Either way, the result for the FDF is an array of complex numbers at discrete frequencies and amplitudes.

Gopinathan et al.[27] have developed a method to represent an FDF by analytical expressions, both for the frequency dependence *and* the amplitude dependence. The amplitude dependence of the FDF was modelled by allowing these fitting parameters to be amplitude-dependent.

Again, the fitting parameters were determined in the frequency domain. To this end, the FDF corresponding to (11) was calculated analytically (this was done by Fourier transform, assuming that the heat release rate is zero or close to zero for negative time-lags), and the result was

$$
\begin{aligned}
\mathcal{T}_k(\omega, a) = n_1(a) \mathrm{e}^{-\omega^2 \sigma_1(a)^2/2} \mathrm{e}^{\mathrm{i}\omega\tau_1(a)} + \cdots \\
+ n_k(a) \mathrm{e}^{-\omega^2 \sigma_k(a)^2/2} \mathrm{e}^{\mathrm{i}\omega\tau_k(a)}
\end{aligned}
\tag{14}
$$

A nonlinear optimisation routine was used, in which the discrepancy between the given $\mathcal{T}(\omega, a)$ and the approximation $\mathcal{T}_k(\omega, a)$ was minimised. The outputs were sets of $3k$ parameters, $n_1(a), \ldots n(a)_k$, $\tau_1(a), \ldots \tau_k(a)$, $\sigma_1(a), \ldots \sigma_k(a)$ for the discrete amplitude values at which $\mathcal{T}(\omega, a)$ is available. In order to get an idea of the number k of Gaussian distributions needed for the approximation, it is advisable to calculate the $n(\tau)$ distribution as outlined in section 4.1.

The fitting parameters were assumed to change smoothly with amplitude a, so that their amplitude dependence could be represented by low-order polynomials, e.g. τ_1 was approximated by a quadratic function of a.

The method was validated by applying it to Noiray's matrix burner.[28] Data for the gain and phase of the FDF of this burner were available in the frequency range $0, \ldots 1200$ Hz, at five different amplitudes $a/\bar{u} = 0.13, 0.23, 0.40, 0.48, 0.54$ (see markers in Figure 11).

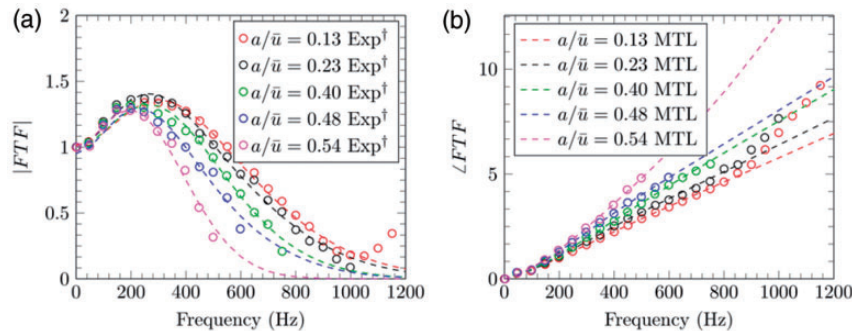Figure 12 shows the corresponding IR of the matrix flame for each of the five amplitudes, calculated by

Figure 11. FDF of Noiray's matrix flame vs. frequency. Markers: measured values (after Figure 6 in Noiray et al.[28]). Dashed curves: Gopinathan's approximation based on (11) with linear fitting functions for $n_1(a), \ldots n_k(a)$, $\sigma_1(a), \ldots \sigma_k(a)$, and quadratic fitting functions for $\tau_1(a), \ldots \tau_k(a)$. (a) Gain and (b) Phase (after Figure 3 in Gopinathan et al.[27]).

using the inverse *z*-transform (described in Polifke[29]). There is a dominant Gaussian-shaped peak in the τ-interval $\left[0.4 \times 10^{-3}\,\text{s} \ldots 2 \times 10^{-3}\,\text{s}\right]$. Its exact position and peak value depend on the amplitude $a/\bar{u}$. This peak is followed by a smaller, inverted peak in the τ-interval $\left[1.6 \times 10^{-3}\,\text{s} \ldots 3.6 \times 10^{-3}\,\text{s}\right]$. Subsequent peaks are considerably smaller, and this suggested that two Gaussian distributions are sufficient in this case for the analytical approximation.

The approximations $\mathcal{T}_k(\omega, a)$ are shown for $k = 2$ by the continuous dashed curves in Figure 11. The agreement is clearly very good, both in terms of the frequency dependence and in terms of the amplitude dependence.

This analytical FDF was also used to make stability predictions for Noiray's matrix burner. Reasonable
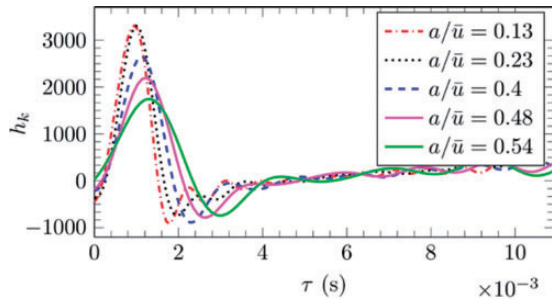

Figure 12. Impulse response corresponding to the measured FTFs shown in Figure 11 (after Figure 4 in Gopinathan et al.[27]).
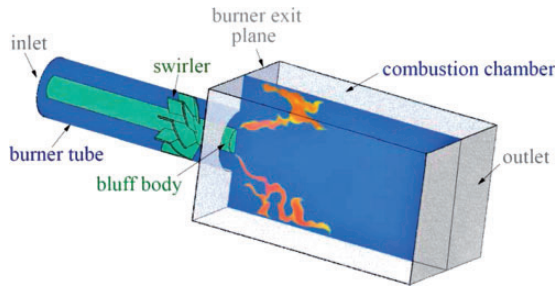

Figure 13. The BRS test rig (from Bigongiari et al.[31]).

qualitative agreement was obtained, even if some mismatches are still present and most likely due to other factors, such as the damping model; this is still a topic of ongoing research.

4.4. Application to a laboratory test rig with a swirl flame

The procedure described in section 4.2 was applied by Bigongiari et al.[30] to find an analytical description for the heat release rate in a specific laboratory test rig developed by Komarek and Polifke[15] at TU Munich. The rig is called the 'BRS test rig' and is shown schematically in Figure 13.

It is a swirl-stabilised atmospheric burner with a central bluff body. A perfectly premixed methane–air mixture with equivalence ratio of 0.77 passes through a swirler with eight blades and enters the combustion chamber, where it is burnt in a non-compact flame.

The FDF of this burner was determined with 3D combustion computational fluid dynamics (CFD; URANS), which was implemented in an OpenFOAM environment. The turbulence was modelled with an SST k–ω turbulence model. The combustion was modelled with the flame-speed closure model proposed in Lipatnikov and Chomiak.[32] This model does not resolve the combustion chemistry, but it takes into account the dependence of turbulent diffusivity and turbulent flame speed on the time it takes a fluid particle to propagate from the flame holder (downstream end of the bluff body) to the flame front.

The flame dynamics was determined from transient numerical simulations. A velocity signal emerging from a reference position was imposed, and the ensuing total heat release rate was calculated. This was done with single-frequency signals for four different frequency values (100, 160, 240 and 320 Hz) and four different amplitude values ($a/\bar{u} = 0.1$, 0.3, 0.5, 0.7). The results for the gain and phase of the FDF are shown by the markers in Figure 14.

An analytical approximation was developed for these results, based on the expression (14) with three
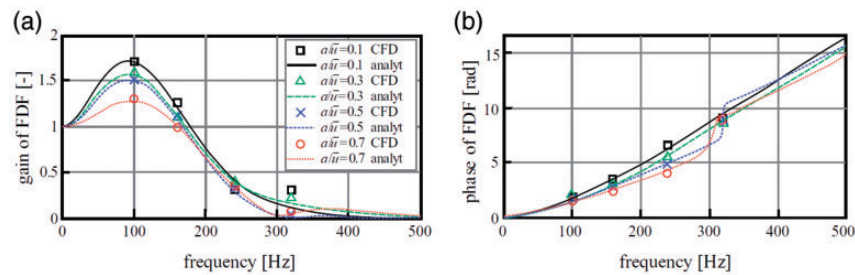

Figure 14. Gain and phase of the FDF of the BRS burner. Markers: Results from transient CFD simulations. Curves: Analytical approximations based on equation (14) (after Figure 1 in Bigongiari et al.[30]).

terms ($k = 3$) included. The time-lags τ_1, τ_2, τ_3 and the standard deviations σ_1, σ_2, σ_3 were treated as fitting parameters. A clear trend in their amplitude-dependence was observed. The amplitude-dependence of the time-lags was approximated by decreasing quadratic functions, and that of the standard deviations by linear functions. The coupling coefficients were kept constant. The resulting analytical approximations of the FDF are shown by the curves in Figure 14.

This analytical FDF was subsequently used successfully[33] in a stability analysis of the BRS burner, which was modelled as a low-order network. Limit cycle amplitudes and frequencies were predicted for various combustion chamber lengths. The results of this analysis were consistent with experimental observations. Moreover, unstable ITA modes were identified.

A slightly simplified version of the approach described in section 4.2 was taken by Iurashev et al.[34] In order to model the swirl burner in Figure 13, they assumed an FDF of the form

$$
\begin{aligned}
\mathcal{T}_3(\omega, a) = {}& e^{-\omega^2 \sigma_1(a)^2/2}\, e^{i\omega\tau_1(a)} + \\
& 1.05\Big[e^{-\omega^2 \sigma_2(a)^2/2}\, e^{i\omega\tau_2(a)} - e^{-\omega^2 \sigma_3(a)^2/2}\, e^{i\omega\tau_3(a)}\Big]
\end{aligned}
\tag{15}
$$

This is a special case of (14) with $k = 3$ and with pre-determined coupling coefficients ($n_1 = 1$, $n_2 = 1.05$, $n_3 = -1.05$). The number of fitting parameters was therefore reduced to τ_1, τ_2, τ_3, σ_1, σ_2, σ_3; these were again assumed to be amplitude-dependent. An expression similar to (15), but with only two terms, was subsequently used to model an industrial-sized premixed combustion test rig.[35]

5. Green's function approach applied to thermoacoustic instabilities

The Green's function is the response to an impulsive point source perceived by an observer. The *tailored* Green's function is the Green's function, which satisfies the boundary conditions of the cavity (e.g. combustion chamber) in which the source is located. Physical insight suggests that the tailored Green's function is a superposition of the acoustic modes of the cavity. The frequencies and amplitudes of the cavity modes can be calculated analytically for basic geometries.

The tailored Green's function is a powerful tool to solve problems that can be described mathematically by a nonhomogeneous wave equation. Thermoacoustic problems are in this category, including cases, where the heat release rate is *nonlinear*. An outline of the solution strategy is given in section 5.1. The subsequent sections show several applications developed by TANGO researchers: Section 5.2 demonstrates the Green's function approach for a selection of nonlinear heat release laws and gives results for the ensuing limit cycles. Section 5.3 applies a Green's function method to predict stability maps and hysteresis behaviour. Nonlinear interactions between two thermoacoustic modes are studied in section 5.4. Finally, section 5.5 introduces a hybrid analytical/numerical approach, where CFD calculations of the heat release rate from a flame are combined with a Green's function approach in order to make fast and accurate stability predictions.

5.1. Outline of the approach

The sound field generated by a heat source with heat release rate $q(x, t)$ (per unit mass) is governed by the acoustic analogy equation. In terms of the velocity potential $\varphi(x, t)$, this equation reads

$$
\frac{1}{c^2}\frac{\partial^2 \varphi}{\partial t^2} - \frac{\partial^2 \varphi}{\partial x^2} = -\frac{\gamma - 1}{c^2} q(x, t)
\tag{16}
$$

Its solution is subject to the boundary conditions of the combustion chamber and to two initial conditions, for $\varphi(x, t)|_{t=0}$ and $\dot{\varphi}(x, t)|_{t=0}$.

A commonly used method for finding a solution to this equation is the Galerkin expansion, which goes back to Zinn and Lores.[36] The acoustic field in the combustion chamber is written as a sum of basis functions termed 'Galerkin modes', with time-varying coefficients. Typically, the basis functions of a half-wave resonator or quarter-wave resonator, $\sin(n\pi x/L)$ and $\cos(n\pi x/L)$, are used because of their simple analytical form. However, for many combustion chamber geometries, the eigenmodes have a different profile. The Galerkin approach can still be used, but one needs to include a lot of terms in the Galerkin series to get useful results, and the physical interpretation of Galerkin modes as eigenfunctions gets lost.

A more accurate and physically representative method is an expansion in terms of *actual* modes of the combustion chamber. These are the modes that are excited by an impulsive point source. The tailored Green's function, which is the response of an acoustic resonator to an impulsive point source, is a superposition of exactly these modes. It is denoted here by $G(x, x', t, t')$, where x', t' are the source position and firing time, respectively, and x, t are the observer position and observer time, respectively. Its governing equation for the 1D case is the nonhomogeneous wave equation

$$
\frac{1}{c^2}\frac{\partial^2 G}{\partial t^2} - \frac{\partial^2 G}{\partial x^2} = \delta(x - x')\delta(t - t')
\tag{17}
$$

subject to the boundary conditions of the acoustic resonator. The solution can be determined analytically and has the form

$$G(x, x', t, t') = \text{H}(t - t')\text{Re}\left\{\sum_{n=1}^{\infty} g_n(x, x')e^{-i\omega_n(t-t')}\right\}$$

(18)

$\text{H}(t - t')$ denotes the Heaviside function; this ensures that the response before the impulse is zero (causality). The modal amplitudes of the tailored Green's function are $g_n(x, x')$, and ω_n are the modal frequencies. These frequencies are identical with the eigenfrequencies of the combustion chamber without thermoacoustic feedback.

Analytical expressions for g_n and ω_n can be obtained for quasi-1D geometries with the following features:

– jump in mean temperature,
– jump in cross-sectional area,
– orifice or other localised blockage,
– general reflection coefficients describing the boundary conditions at the resonator ends.

The governing differential equations (16) for the sound field in a combustion chamber and (17) for the tailored Green's function, have exactly the same structure, and their solutions satisfy the same boundary conditions. These features can be exploited mathematically to derive a governing integral equation for the acoustic field in terms of the tailored Green's function. This has been done by Heckl and Howe.[37] They considered a compact heat source at position x_q, described by

$$q(x, t) = q(t)\delta(x - x_q)$$

(19)

and initial conditions localised also at position x_q, described by

$$\varphi(x, t)|_{t=0} = \varphi_0\delta(x - x_q) \text{ and } \dot{\varphi}(x, t)|_{t=0} = \dot{\varphi}_0\delta(x - x_q)$$

(20a, b)

with specified values of φ_0 and $\dot{\varphi}_0$. The resulting integral equation is

$$u_q(t) = -\frac{\gamma - 1}{c^2}\int_{t'=0}^{t} \frac{\partial G(x, x', t, t')}{\partial x}\bigg|_{\substack{x=x_q \\ x'=x_q}} q(t')dt'$$

$$-\frac{\varphi_0}{c^2}\frac{\partial^2 G}{\partial x \partial t'}\bigg|_{\substack{x=x_q \\ x'=x_q \\ t'=0}} + \frac{\dot{\varphi}_0}{c^2}\frac{\partial^2 G}{\partial x}\bigg|_{\substack{x=x_q \\ x'=x_q \\ t'=0}}$$

(21)

where u_q is the velocity at the heat source. If the heat release rate $q(t)$ is known in terms of u_q, the problem is closed, and the solution of (21) gives the evolution of an initial perturbation.

The solution is best obtained numerically by discretising (21) and performing an iteration stepping forward in time with time steps Δt. The procedure works not just for linear heat release laws; it works equally well for *nonlinear* heat release laws and thus provides an important and convenient tool for nonlinear studies.

5.2. Nonlinear predictions – Limit cycle properties

Crespo Anadón et al.[38] have applied this method to predict the limit cycle amplitudes and frequencies of an atmospheric test rig. This was modelled as a tube with uniform cross-section (area S) and with two zones: a cold zone ($\bar{T}_1 = 304$ K) and a hot zone ($\bar{T}_2 = 632$ K), separated by a compact flame at the axial position $x = x_q$. The boundary conditions at the ends were described by pressure reflection coefficients R_0 and R_L. A schematic of the modelled test rig is shown in Figure 15. Only the first mode was considered, i.e. only the $n = 1$ term was included in the Green's function (18).

Three different nonlinear heat release laws were studied

$$q(t) = \frac{\bar{Q}}{S\bar{\rho}\bar{u}}\left\{n_0 + n_1\left[\frac{u_q(t - \tau)}{\bar{u}}\right]^2 + n_2\left[\frac{u_q(t - \tau)}{\bar{u}}\right]^4\right\}$$
$$\times u_q(t - \tau)$$

(22a)

(Van der Pol polynomial)

$$q(t) = \frac{\bar{Q}}{S\bar{\rho}\bar{u}}\left\{n_0 + n_1\left|\frac{u_q(t - \tau)}{\bar{u}}\right|\right\}u_q(t - \tau)$$

(22b)

(Levine–Baum heat release law), and

$$q(t) = \begin{cases} -\frac{\bar{Q}}{S\bar{\rho}\bar{u}}u_q(t - \tau) & \text{for } |q(t)| < q_{max} \\ \pm q_{max} & \text{for } |q(t)| \geq q_{max} \end{cases}$$
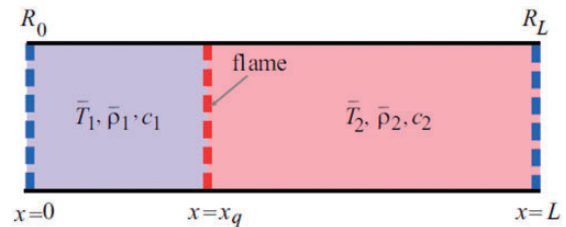
(22c)

(capped linear heat release rate).

Figure 15. Schematic of the combustion test rig under consideration (after Figure 1 in Bigongiari and Heckl[39]).
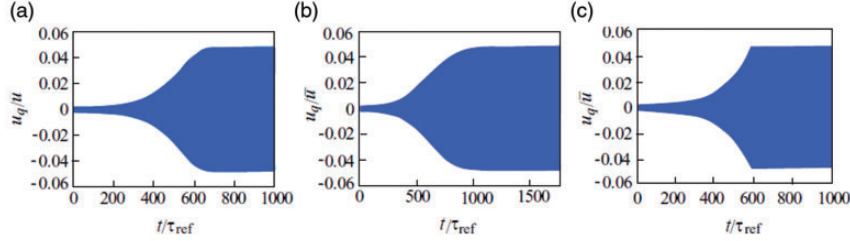
Figure 16. Time evolution of the acoustic velocity for nonlinear heat release laws. (a) Van der Pol polynomial with $n_0 = 1$, $n_1 = -10$, $n_2 = -3 \times 10^8$. (b) Levine-Baum heat release law with $n_0 = 1$, $n_1 = -17.3$ and (c) Capped linear heat release rate with $q_{max} = 0.007\bar{Q}/(S\bar{\rho}\bar{u})$ (after Figures 3, 5, 7 in Crespo Anadón et al.[38]).

The evolution of the (normalised) velocity, $u_q/\bar{u}$, with time is shown in Figure 16 for the three heat release laws (22a,b,c). The time-lag was taken to be $\tau = 1.8\tau_{ref}$, with $\tau_{ref} = L/c_2$ for all three laws. The time histories all follow the same pattern: starting from a small perturbation, the oscillation grows exponentially. As the amplitude increases, the growth slows down, and eventually a limit cycle forms.

The limit cycle frequency was found to be slightly different from the eigenfrequency of the combustion chamber without thermoacoustic feedback; the frequency shift was between -3% and $+3\%$, depending on the value of the time-lag τ.

5.3. Nonlinear predictions – Stability maps and hysteresis

The Green's function method described in section 5.1 was applied by Bigongiari and Heckl[39] to predict non-linear stability maps and to identify hysteresis behaviour. Two geometries were studied: a half-wave resonator (Rijke tube) with $R_0 = R_L = -1$, and a quarter-wave resonator with $R_0 = 1$, $R_L = -1$. There was a temperature jump at x_q from 304 K to 460 K. The tube length was $L = 2$m in both cases. Only the first mode was considered.

A generic amplitude-dependent heat release law was assumed

$$q(t) = \frac{\bar{Q}}{S\bar{\rho}\bar{u}}\left[n_1 u_q(t - \tau) - n_0 u_q(t)\right] \quad (23)$$

where the time-lag τ increased quadratically with amplitude, and the coupling coefficients n_1, n_0 decreased linearly with amplitude.

The heat source position x_q was chosen as control parameter. Equation (21) was again solved iteratively by stepping forward in time (as in section 5.2), but now the control parameter was varied during the time history calculation.

Figure 17 shows the stability map in the parameter plane of x_q and $a/\bar{u}$ (non-dimensional amplitude).

Unstable regions are shaded in grey; stable regions are white.

In the stability map for the Rijke tube, there is a vertical transition line just before $x_q = L/2$. This is due to the phase jump between the acoustic pressure and velocity. The alternating regions of stability and instability along the amplitude axis are due to the fact that the lime-lag increases with amplitude and crosses the critical values $\tau = T_1/2$, T_1, where T_1 is the period of the first mode. In the stability map for the quarter-wave resonator, the vertical transition line is absent. There is a region of stability at low amplitudes, followed by a region of instability at higher amplitudes.

If the system is at a point in an unstable (grey) zone in Figure 17(a) or (b), the perturbation amplitude grows until the border with a stable region is reached. On the other hand, if the system is in a stable (white) zone, the amplitude drops down to the border with the neighbouring unstable zone. The curved interfaces at the top of the grey zones represent stable limit cycles: any small variation of $a/\bar{u}$ from the interface will bring the perturbation back to the original amplitude.

In order to study hysteresis effects, the control parameter was varied in one direction and then in the reverse direction *during* the calculation of the time history. The results are illustrated here for the Rijke tube where the control parameter is the heat source position x_q, which was moved from the outlet of the tube in the upstream direction (from right to left) to just beyond the half-way point; there the motion was reversed (from left to right). The iteration calculating the time history simply continues at the point of reversal, i.e. no new initial conditions are introduced. The paths are shown in Figure 18, superimposed on the map in Figure 17(a); only a part of Figure 17(a) is displayed (the bottom right section).

The dashed green line shows the right-to-left path (indicated by green arrows); the solid blue line shows the left-to right path (indicated by blue arrows). The forward and reverse paths are clearly different, indicating that hysteresis is present. This is in exact qualitative
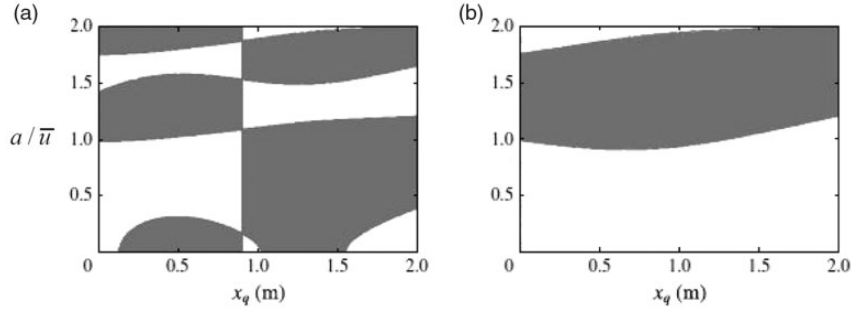
Figure 17. Stability maps depicting the dependence on the heat source position x_q of the amplitude $a/\bar{u}$. Stable regions are white; unstable regions are grey. (a) Rijke tube and (b) Quarter-wave resonator (from Figure 4 in Bigongiari and Heckl[39]).
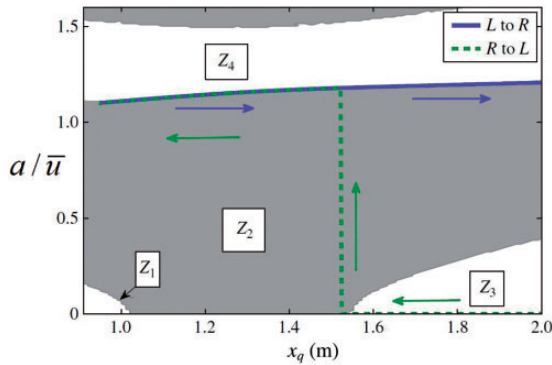

Figure 18. Hysteresis in the stability map of the Rijke tube with the heater position x_q as control parameter. Stable regions (white) are labelled Z_1, Z_3, Z_4; the unstable region (grey) is Z_2 (from Figure 11 in Bigongiari and Heckl[39]).

agreement with the experimental observations reported in Gopalakrishnan and Sujith.[40]

Stability maps were calculated not just with the heater position as control parameter, but also with tube length and heater power. Again, hysteresis behaviour was observed.

5.4. Nonlinear predictions – Interaction between two modes

The Green's function method described in section 5.1 was applied in Bigongiari and Heckl[41] to study the interaction between two modes. The combustion chamber was again modelled as shown in Figure 15 with a temperature jump at the heater position ($x_q = 0.2$m) from $\bar{T}_1 = 300$K to $\bar{T}_2 = 1700$K. Two sets of boundary conditions were considered (Rijke tube and quarter-wave resonator); the length of the tube was varied. The heat release rate was described by a generic FDF of the form given in equations (12) and (13) with two terms ($k = 2$) and with amplitude-dependent parameters n_1, n_2, τ_1, τ_2, σ_1, σ_2.

The Green's function is now assumed to have *two* modes: $n = 1$ and $n = 2$ in equation (18); all other modes have zero amplitude (i.e. $g_3 = g_4 = \ldots = 0$). The time history was calculated by solving (21) iteratively, staring with the initial condition $u_q(t)\big|_{t=0} = 0.01\bar{u}$.

The time history for the Rijke tube with length 1.2 m is displayed in Figure 19.

The amplitude increases exponentially at first, then grows less rapidly; beyond about $t = 2$s, a limit cycle is established with the final amplitude $a/\bar{u} = 0.1$. The corresponding frequency spectrum was calculated for two time windows of the evolution: for $[0,1\,\text{s}]$ (exponential growth stage), and $[9\,\text{s}, 10\,\text{s}]$ (limit cycle stage). These are shown in Figure 20.

Other interactions between the two modes have been found for other tube lengths. For example, for $L = 2$m, mode 2 is dominant during the initial stage $[0,1\,\text{s}]$, but mode 1 takes over later in the evolution. These are results, which cannot be found by analysing the stability of modes 1 and 2 in isolation. They are a manifestation of the non-normality of thermoacoustic modes.

5.5. Hybrid approach for fast predictions

A hybrid approach, combining the accuracy of numerical CFD simulations with the fast prediction speed of a Green's function approach, was taken by Bigongiari et al.[30] They applied this to the BRS test rig described in section 4.3 and shown in Figure 13.

To this end, the burner is idealised as shown in Figure 21. The burner tube is described as a tube of uniform cross-section with constant temperature; the combustion chamber has a larger cross-section and a higher constant temperature. The swirler is ignored. The flame is assumed to be compact and located at the position x_q; this is downstream of the burner exit plane, which is located at x_j. The boundary conditions at the tube ends are described by reflection coefficients R_0 and R_L.

The tailored Green's function has the form given in (18). Analytical expressions for the Green's function
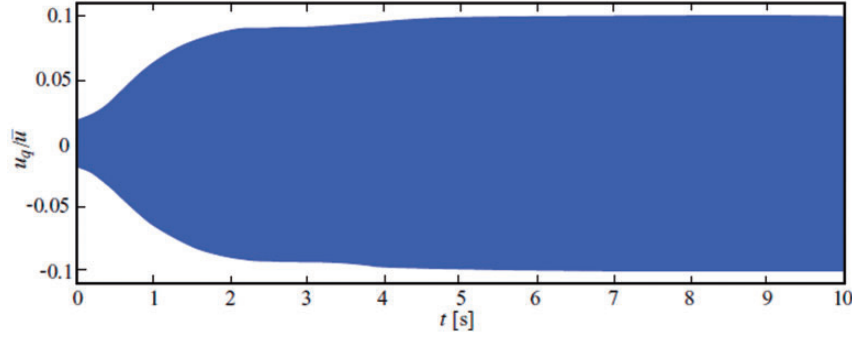
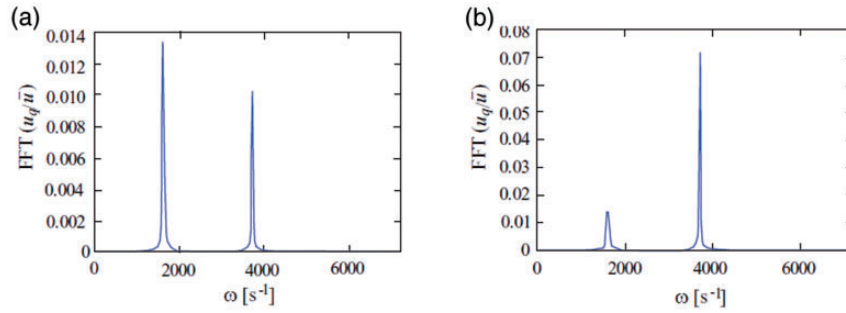**Figure 19.** Time history of $u_q(t)/\bar{u}$ in a Rijke tube with $L = 1.2$m (after Figure 5 in Bigongiari and Heckl[41]).

Figure 20. Fourier transform of the time history $u_q(t)$ shown in Figure 5.5. (a) Time-window [0,1 s] and (b) Time-window [9 s, 10 s] (after Figure 6 in Bigongiari and Heckl[41]).

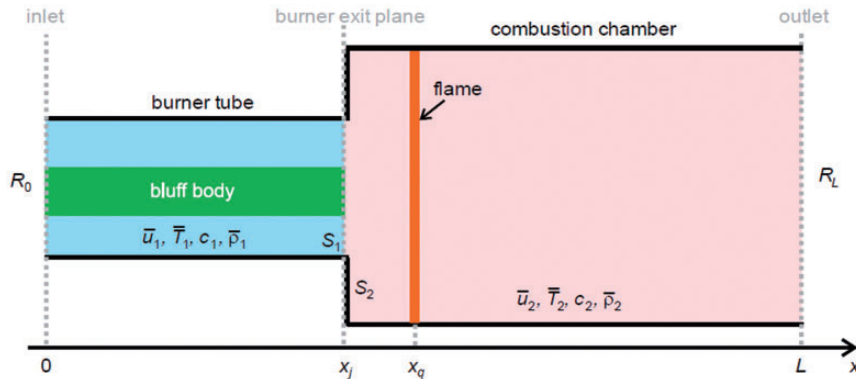**Figure 21.** Idealised version of the BRS test rig shown in Figure 4.4 (from Figure 2 in Bigongiari et al.[30]).

amplitudes g_n and frequencies ω_n for the test rig in Figure 21 can be found in Bigongiari et al.[30]

The flame is modelled by an FDF similar to the one in section 4.3

$$\frac{Q'(t)}{\bar{Q}} = n_1 \int_0^\infty \frac{u'(t-\tau)}{\bar{u}} D_1(\tau - \tau_1)\, \mathrm{d}\tau$$
$$+ n_2 \int_0^\infty \frac{u'(t-\tau)}{\bar{u}} D_2(\tau - \tau_2)\mathrm{d}\tau \quad (24)$$

with D_1, D_2 given by (12).

Instead of solving the integral equation (21) directly, it is used as a basis for a modal analysis. To this end, the acoustic velocity is expressed as a sum of *thermo-acoustic* modes with complex amplitudes u_m and complex frequencies Ω_m

$$u_q(t) = \sum_{m=1}^\infty \left(u_m \mathrm{e}^{-i\Omega_m t} + u_m^* \mathrm{e}^{i\Omega_m^* t} \right) \quad (25)$$

where * denotes the complex conjugate. Equations for the unknowns Ω_m and u_m are derived (procedure
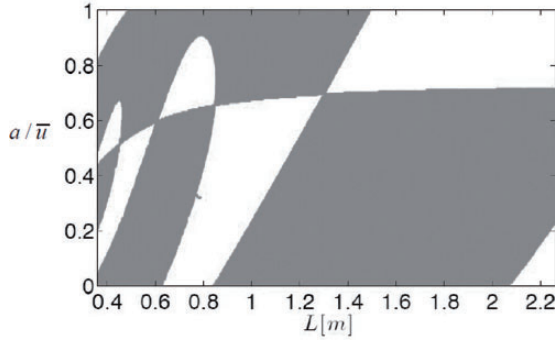
Figure 22. Stability map for the control parameter *L. Grey* areas are regions of instability; white areas are regions of stability (from Figure 3 in Bigongiari et al.[30]).

similar to that described in Bigongiari and Heckl[39]); the equation for Ω_m is

$$e^{i\Omega_m\tau}\int_{\tau=0}^{\infty}[n_1 D_1(\tau) - n_2 D_2(\tau)]d\tau$$
$$\times \sum_{n=1}^{\infty}\left[\frac{G_n}{i(\omega_n - \Omega_m)} - \frac{G_n^*}{i(\omega_n^* - \Omega_m)}\right] = -\frac{2c^2}{K(\gamma-1)}$$

(26)

with G_n given by

$$G_n = \frac{\partial g_n(x,x')}{\partial x}\bigg|_{\substack{x=x_q\\x'=x_q}}$$

(27)

By solving (26) for Ω_m (e.g. by the Newton/Raphson method) and then determining the sign of ImΩ_m, the stability behaviour of the individual modes can be determined very quickly. Figure 22 shows the results for mode 1 (assuming reflection coefficients $R_0 = 1$, $R_L = -1$) in the parameter space L (tube length) and $a/\bar{u}$ (velocity amplitude).

This hybrid approach combines the best of both worlds:

– accurate description of the flame dynamics (from the world of CFD calculations);
– fast stability prediction with a minimum of numerical effort (from the world of analytical methods based on the tailored Green's function). Once the flame dynamics is known, it takes just a few seconds (on a standard PC or laptop) to produce a stability map like the one in Figure 22.

6. Intrinsic thermoacoustic modes

Many flames are velocity-sensitive and follow a time-lag law, the simplest being the well-known $n\tau$-law

$$\frac{Q'(t)}{\bar{Q}} = n\frac{u'(t-\tau)}{\bar{u}}$$

(28)

where u' is the velocity perturbation at some reference position upstream of the flame, and Q' is the rate of heat release at the flame position. Typically, τ is the time it takes a kinematic or vortical perturbation to travel from the reference position to a point along the flame. This time-lag gives rise to *two* feedback loops, which are outlined below for a basic 1D combustion system comprising a single cavity of length L.

Thermoacoustic feedback. A flame with an unsteady heat release rate acts like an acoustic monopole source, generating acoustic waves; these are reflected at the boundaries of the combustion chamber to return to the flame and influence its heat release rate. The modes generated by this mechanism are called 'thermoacoustic modes' (or TA modes). The time-lag τ is an important quantity, which determines whether this feedback is constructive or destructive, and whether a particular mode becomes unstable. The frequencies of these modes are generally similar to the resonance frequencies of the combustion chamber. For the special cases where the combustion chamber is a half-wave or quarter-wave resonator, they are, respectively

$$f_{\lambda/2} = m_{TA}\frac{c}{2L} \quad \text{and} \quad f_{\lambda/4} = \left(m_{TA} - \frac{1}{2}\right)\frac{c}{2L} \quad \text{(29a, b)}$$

where $m_{TA} = 1, 2, \ldots$ is the mode number. These frequencies have a strong dependence on the length L of the combustion chamber and on the speed of sound c, which in turn depends strongly on the temperature.

Intrinsic thermoacoustic feedback. A velocity disturbance impinging on the flame modulates the heat release rate, which in turn generates an acoustic wave. The upstream-travelling part of this wave influences the velocity at the reference position and thus closes the feedback loop.[42] The modes generated by this mechanism are called 'intrinsic thermoacoustic modes'. Again, the time-lag is an important quantity in that it influences the frequency and growth rate of an intrinsic mode. These properties are known for the special case, where the flame is situated in an acoustically anechoic 1D environment (such as an infinitely long tube)[43]

$$f_{ITA} = \left(m_{ITA} - \frac{1}{2}\right)\frac{1}{\tau}$$

(30a)

$$\delta_{ITA} = -\frac{1}{\tau}\ln\frac{\xi+1}{nT_{21}}$$

(30b)

where $m_{ITA} = 1, 2, \ldots$ is the mode number; T_{21} is a measure for the temperature jump across the flame

$$T_{21} = \frac{\bar{T}_2 - \bar{T}_1}{\bar{T}_1}$$

(31a)

and ξ is the impedance ratio

$$\xi = \frac{\bar{\rho}_1 c_1}{\bar{\rho}_2 c_2} \qquad (31b)$$

The frequencies f_{ITA} depend only on the time-lag and the mode number; the growth rate is the same for all modes and depends on τ, n and the mean heat release, which determines T_{21} and ξ.

The two feedback loops are likely to interact with one another because the acoustic waves emitted by the unsteady flame play a role in both feedback loops.

The subsequent sections give highlights of the research in the TANGO project on ITA modes. Sections 6.1 and 6.2 present fundamental studies, considering single-cavity resonators, enclosing a flame described by an $n\tau$-law. Section 6.1 is predominantly analytical and focuses on the role of the interaction index n. Section 6.2 gives a detailed parameter study, exploring the role of the time-lag τ on the interplay between the two mode types. Sections 6.3 and 6.4 consider a more complex system, motivated by the BRS burner (shown in Figure 13 without the plenum). A network model is developed, with the following elements: The flame is described by an FTF (rather than a simple $n\tau$-law); the combustion system comprises two or three cavities (rather than just a single one); a swirler in the burner tube adds another level of complexity. The study in section 6.3 is largely analytical and makes use of the FTF data gathered by earlier researchers; it focuses on the influence of time delays generated by convective processes. The study in section 6.4 is predominantly numerical and calculates the FTF by CFD.

6.1. Fundamental study of intrinsic modes in a 1D resonator

Mukherjee et al.[44,45] have performed a fundamental study of intrinsic modes in a quarter-wave resonator. The resonator is a tube of length L; the upstream end is closed, the downstream end is open, and the temperature is uniform throughout the tube. The flame, which is compact, is situated at the axial position x_q and described by a basic time-lag law. The flame divides the tube into two regions. Pairs of upstream and downstream travelling waves are present in each of the two regions. The following conditions across the flame are assumed:

– the pressure is continuous;
– the velocity jumps by $\tilde{n}e^{i\omega\tau}\hat{u}(x_q)$, where $\hat{u}$ is the velocity (in the frequency domain) on the upstream side of the flame; $\tilde{n}$ is a non-standard interaction index, which is proportional to n in (28).

An eigenvalue analysis leads to the characteristic equation

$$2\left[e^{ikL} + e^{-ikL}\right] \\ + \tilde{n}e^{i\omega\tau}\left[e^{-ikL} - e^{ik(L-2x_q)} - e^{-ik(L-2x_q)} + e^{ikL}\right] = 0 \qquad (32)$$

where $k = \omega/c$ is the wave number.

It is possible to draw conclusions analytically about the properties of the eigenfrequencies for the special case where the interaction index $\tilde{n}$ is very small, i.e. for weak thermoacoustic coupling. In this case, there are two sets of solutions for the complex eigenfrequencies $\omega = \omega_r + i\omega_i$: weakly damped solutions and strongly damped solutions.

Weakly damped solutions are characterised by $\omega_i \approx 0$. In this case, the exponential term $e^{i\omega\tau}$ in (32) is of order 1, as are the terms $e^{\pm ikL}$ and $e^{\pm ik(L-2x_q)}$. Hence, in the limit $\tilde{n} \to 0$, all that remains of equation (31) is

$$\cos kL = 0 \qquad (33)$$

This is the well-known formula for the eigenfrequencies of a quarter-wave resonator with solutions (29b).

Strongly damped solutions are characterised by $\omega_i \ll 0$, with large $|\omega_i|$. In order to analyse this case, equation (32) is multiplied by e^{-ikL}. The ensuing equation has complex exponential terms, which all become very small as $\omega_i \to -\infty$. All that remains of equation (32) in this limit is

$$2 + \tilde{n}e^{i\omega\tau} = 0 \qquad (34)$$

The solutions of this equation are

$$\omega = (2m_{ITA} - 1)\frac{\pi}{\tau} - i\frac{1}{\tau}\ln\frac{2}{\tilde{n}} \qquad (35)$$

which is equivalent with (30a,b).

In summary, for the case of small $\tilde{n}$, there are two sets of infinitely many modes: TA modes with mode numbers, $m_{TA} = 1, 2, \ldots$, and ITA modes with mode numbers $m_{ITA} = 1, 2, \ldots$.

The analytical studies were extended in Mukherjee and Shrira[45] to the case of larger $\tilde{n}$. They found that any ITA mode becomes unstable above a certain threshold value of $\tilde{n}$, provided that τ is within a certain range. They determined the 'neutral curve', i.e. the curves separating regions of stability and instability in the $\tilde{n}\tau$-plane in terms of an explicit function $\tilde{n} = \tilde{n}(\tau)$. For a given ITA mode, the oscillation frequency on the neutral curve was found to coincide with the frequency of that mode in an anechoic tube. The growth rates in
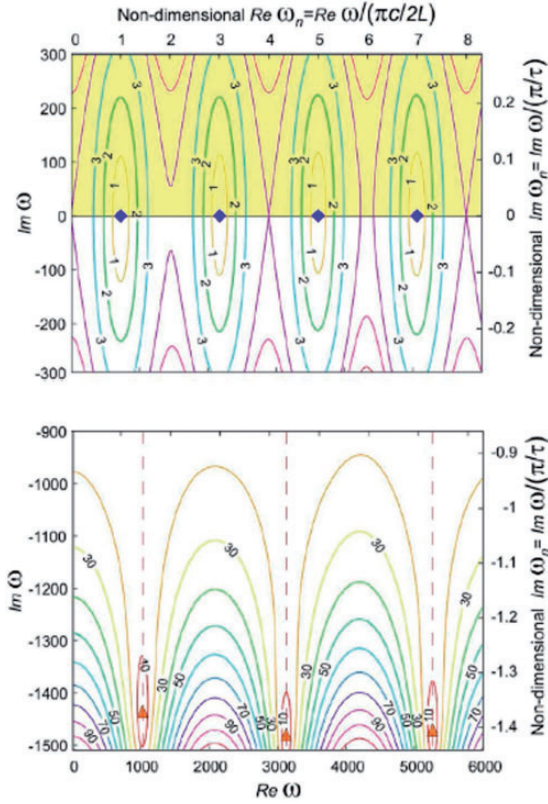
Figure 23. Contour plot of $|f(\omega)|$ in the complex frequency plane for $\tilde{n} = 0.025$, $\tau = 3$ ms. The two sections are parts of the same plot. Yellow shading indicates instability (from Figure 3 in Mukherjee and Shrira[45]).

Figure 24. Contour plot of $|f(\omega)|$ in the complex frequency plane for $\tilde{n} = 1$, $\tau = 3$ ms. Yellow shading indicates instability (from Figure 4 in Mukherjee and Shrira[45]).

the vicinity of the neutral curve have also been found analytically.

Mukherjee et al.[44,45] also performed *numerical* studies to investigate how the complex eigenfrequencies are affected when $\tilde{n}$ is increased. They displayed their numerical results in the form of contour plots of $|f(\omega)|$ in the complex ω-plane, where $f(\omega)$ is the left hand side of (32). The eigenfrequencies are situated at points where $|f(\omega)| = 0$; these are surrounded by closed loops, where $|f(\omega)|$ has values close to zero.

Figure 23 shows such a plot for a small $\tilde{n}$ value: $\tilde{n} = 0.025$; the other parameters were $\tau = 3 \times 10^{-3}$s, $L = 0.75$m, $x_q = L/2$, $c = 345$ms^{-1}. For reasons of scale, this plot has been split into two sections. The TA modes (marked by blue diamonds) all have growth rates around zero and are shown in the top-section of the plot. The ITA modes (marked by red triangles) have highly negative growth rates, between -1400 s^{-1} and -1500 s^{-1}, and they are shown in the bottom section.

The effect of increasing $\tilde{n}$ is illustrated in Figure 24, which shows the contour plot of $|f(\omega)|$ for $\tilde{n} = 1$, while the other parameters are the same as in Figure 23. The frequencies of the ITA modes have not changed much,
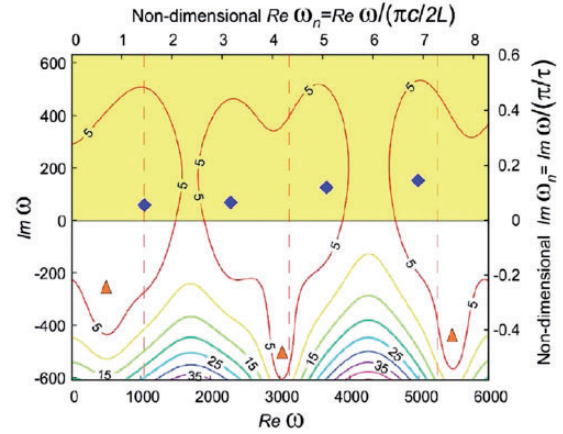
but their growth rate has increased considerably. The TA modes have also been affected in that they have become unstable and experienced a slight frequency shift.

Further increase of $\tilde{n}$ leads to a further increase in the growth rates of the ITA modes, and eventually the growth rates become positive (this is in line with the analytical results in Mukherjee and Shrira[45].

All studies made for the quarter-wave resonator were repeated in Mukherjee[46] for the half-wave resonator. No significant differences were found. Again, two sets of modes were identified for the case of small $\tilde{n}$: undamped TA modes with the eigenfrequencies of a half-wave resonator, given by (29a), and highly damped ITA modes with the same complex eigenfrequencies as those in a quarter-wave resonator. It is not surprising that the ITA modes have the same frequencies irrespective of the resonator boundaries: These modes are highly damped and hence highly localised, i.e. they do not 'feel' the boundaries of the resonator. Non-ideal boundary conditions, described by $|R| < 1$ were also considered in Mukherjee.[46] Such boundary conditions describe tube ends, where acoustic energy is lost from the tube. The ITA modes and TA modes could not be decoupled analytically for such a case. This is in contrast to the case of ideal boundary conditions ($R = 1$ or $R = -1$), where the decoupling was possible for small values of $\tilde{n}$.

6.2. Interplay between ITA modes and TA modes in a Rijke burner

Hosseini et al.[47] performed extensive parameter studies on a Rijke burner, similar to the combustion system depicted in Figure 15. The tube had a length of $L = 1$m, and the flame was situated at $x_q = 0.25$ m.
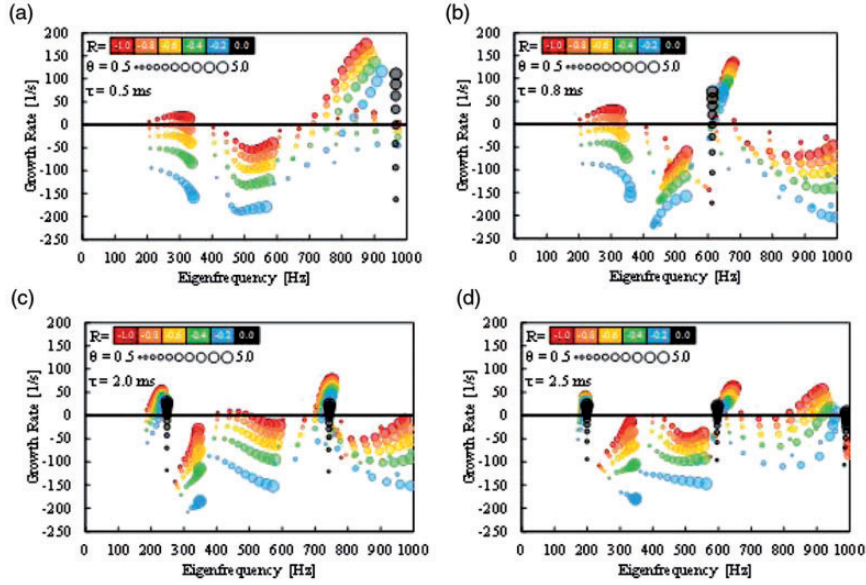
Figure 25. Eigenfrequencies and growth rates for all modes in the frequency window $[0, \ldots 1000\,\text{Hz}]$. The temperature jump, expressed in terms of T_{21} (denoted by θ in the figures) is scaled by marker size; the reflection coefficient R is scaled by colour. (a) $\tau = 0.5\,\text{ms}$. (b) $\tau = 0.8\,\text{ms}$. (c) $\tau = 2.0\,\text{ms}$ and (d) $\tau = 2.5\,\text{ms}$ (from Figures 5(b, c), 8(a, b) in Hosseini et al.[47]).

The temperature upstream of the flame was constant ($\bar{T}_1 = 300\,\text{K}$). The flame had a heat release rate with a fluctuating part (described by the $n\tau$-law in (28) with $n = 1$), and a mean part (which produced a temperature jump across the flame from $\bar{T}_1$ to $\bar{T}_2$). The ends of the tube were open and allowed for acoustic losses.

The focus was on the following three parameters:

– time-lag (varied in the range $\tau = 0, \ldots 5\,\text{ms}$)
– downstream temperature (varied in the range $\bar{T}_2 = 450, \ldots 1800\,\text{K}$, i.e. $T_{21} = 0.5, \ldots, 5$)
– reflection coefficients (same at both ends, purely real, varied in the range $R = -1, \ldots 0$)

The eigenfrequencies and growth rates were calculated from a linear acoustic network model, for all the modes that were present in the frequency window $[0, \ldots 1000\,\text{Hz}]$. By performing parameter sweeps in the ranges indicated above, Hosseini et al.[47] built up a detailed picture of the interplay between ITA modes and TA modes, simulating many practically relevant operating conditions. Figure 25 shows a selection of their results.

Their observations are summarised in the three points below.

– The TA modes are roughly equally spaced along the frequency axis; their frequency values increase with increasing temperature jump, and their growth rates decrease (becoming more and more negative) as $R \to 0$.

– The special case $R = 0$ gives the ITA modes. Their frequency decreases with τ (in line with (30a)); their growth rate increases with increasing temperature jump, becoming positive above a certain T_{21} threshold (in line with (30b)). For $\tau \leq 0.5 \times 10^{-3}\,\text{s}$, the ITA modes all have frequencies beyond 1000 Hz, i.e. they are outside the considered frequency window. As τ increases beyond $0.5 \times 10^{-3}\,\text{s}$, the first ITA mode enters the window from the right and moves to the left. As τ increases further, higher ITA modes follow.

– A notable interplay between the two modes occurs when the frequency of an ITA mode becomes close to that of a TA mode. The ITA mode attaches itself to the TA mode and the ensuing mode (a mixed mode) becomes unstable if the temperature jump is large enough. As τ increases further, the mixed mode is dragged towards lower frequencies. The ITA mode eventually detaches, i.e. the mixed mode splits up into a TA mode and an ITA mode. The ITA mode continues its path to the left, where it meets the next TA mode and repeats the same process with that mode.

The whole process has been visualised in a high-resolution animation, which can be found in a video file supplementing the paper.[47] The overall conclusion is that a detailed parameter study is essential to explore the behaviour of the various modes.

6.3. ITA modes in a laboratory swirl burner – Flame modelled by measured FTF

Fundamental studies of ITA modes tend to consider a highly idealised geometry with a straight duct of uniform cross-section. However, even laboratory burners tend to have more complex shapes; in particular they may have a constriction in cross-sectional area, for example due to the presence of a burner tube (see Figure 26).

The configuration in Figure 26, which had been studied experimentally by Komarek and Polifke[15] in 2010, before ITA modes were recognised, was revisited by Albayrak et al.[48] with a fundamental study on ITA modes.

Following the approach in Silva et al.,[49] a network model was developed. Non-reflective boundary conditions were assumed at the inlet and outlet. The nodes of the network are shown schematically in Figure 26 (in grey). There are four nodes: (1)–(2), (2)–(3), (3)–(4), (4)–(5). The corresponding transitions are listed in Table 3, together with equations describing 'jump conditions' for the acoustic velocity and pressure across the nodes. The acoustic field in the burner tube was modelled as a superposition of forward and backward travelling waves with velocity amplitudes f and g, respectively. The flame was modelled by a FTF $\mathcal{T}(\omega)$. This FTF was taken from measurements.[15] It included not only the effect of the flame, but also the effect of a swirler (not shown in Figure 26), which was located in the burner tube. Experimental data for different swirler positions were available. This showed that the FTF is strongly dependent of the swirler position, which determines how long it takes a swirl wave to travel the
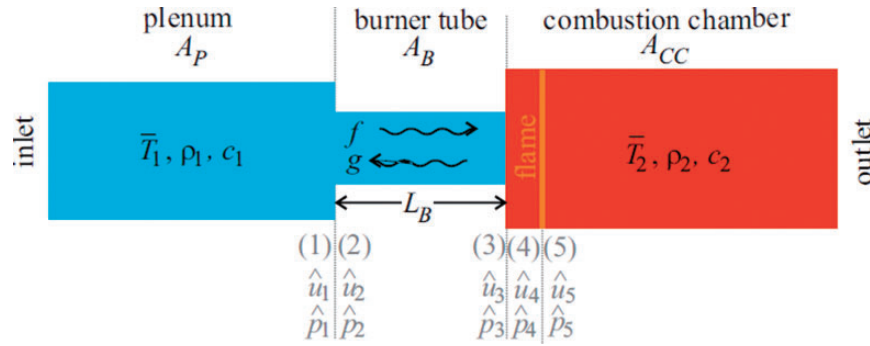

Figure 26. Schematic of a combustion system comprising three cavities: plenum (cold), burner tube (cold), and combustion chamber (hot). Points (4) and (5) are infinitesimally close; they are drawn with a distance between them to visually separate the flame from the jump in cross-section.

Table 3. Details of the network model for the configuration shown in Figure 26.

Node	Type of transition	Equation for velocity jump	Equation for pressure jump
(1)–(2)	Area jump between plenum and burner tube $A_P \rightarrow A_B$ $\beta_{PB} = A_P/A_B > 1$	$\hat{u}_2 = \beta_{PB}\,\hat{u}_1$	$\hat{p}_2 = \hat{p}_1$
(2)–(3)	Acoustic wave propagation with speed of sound c_c along the burner tube	$\hat{u}_2 = f - g$ $\hat{u}_3 = f\,e^{ikL_B} - g\,e^{-ikL_B}$	$\hat{p}_2 = \frac{1}{\rho_1 c_1}(f+g)$ $\hat{p}_3 = \frac{1}{\rho_1 c_1}\left(f\,e^{ikL_B} + g\,e^{-ikL_B}\right)$
(3)–(4)	Area jump between burner tube and combustion chamber $A_B \rightarrow A_{CC}$ $\beta_{BC} = A_B/A_{CC} < 1$	$\hat{u}_4 = \beta_{BC}\,\hat{u}_3$	$\hat{p}_4 = \hat{p}_3$
(4)–(5)	Flame described by measured FTF $\mathcal{T}(\omega) = \frac{\hat{Q}(\omega)/\bar{Q}}{\hat{u}_3(\omega)/\bar{u}_3}$	$\hat{u}_5 = \hat{u}_4 + \beta_{BC}T_{12}\mathcal{T}(\omega)\,\hat{u}_3$	$\hat{p}_5 = \hat{p}_4$

L_B: length of the burner tube.

distance from the swirler to the entrance of the combustion chamber. The reference position for the FTF was point (3) (downstream end of burner tube, see Figure 26).

The characteristic equation resulting from this network model (and from the additional assumption of a compact burner tube, i.e. $\omega L_B/c_c \ll 1$), was found to be

$$T_{21}\mathcal{T}(\omega) + 1 + \frac{\xi}{\beta_{PB}\beta_{BC}} - i\frac{\omega}{c_1}L_I\xi = 0 \qquad (36)$$

where

$$L_I = \frac{\beta_{PB}^2 - 1}{\beta_{PB}^2\beta_{BC}}L_B \qquad (37)$$

is the "inertial length" of the burner tube. This length is a measure of the constriction in the cross-section imposed by the burner tube. It can be larger than the actual length L_B of the burner tube if $\beta_{PB} \gg 1$ and $\beta_{BC} < 1$, i.e. when the burner tube has a much smaller cross-section than the plenum and the combustion chamber.

Various combustor configurations were investigated over a range of operating conditions. Frequencies (not the growth rates) of ITA modes were predicted approximately by finding the frequency values at which the magnitude of the left hand side of (36) has a local minimum. The key parameters of interest were:

– travel time of swirl waves;
– mean velocity in the burner tube (due to its effect on the convective time associated with the flame), related to the thermal powers (30, 50, 70 kW) of the burner;
– inertial length of the burner tube (a measure of the constriction formed by the burner tube).

The effect of the travel time of swirl waves is illustrated in Figure 27, which shows the measured sound pressure level (SPL) as a function of frequency (green curves) and the predicted ITA frequencies (vertical dashed lines) for an unstable configuration. Results are given for two different travel times, which were achieved by changing the swirler position, and hence the travel distance of the swirl waves. In Figure 27(a), the distance from the swirler to the entrance of the combustion chamber was short (0.03 m); in Figure 27(b), that distance was more than four times larger (0.13 m).

Generally, the peaks in Figure 27(a) are at higher frequencies than those in Figure 27(b). This is what one would expect, given that an increase in travel time must lead to an increase in the intrinsic period, and hence to a decrease in frequency. Also, this finding is in line with the early results in Hoeijmakers et al.[43] and Bomberg et al.[42] (given by the inverse relationship (30a) between ITA frequencies and time-lag).

The mean velocity $\bar{u}_3$ in the burner tube affects the flame in that an increase in $\bar{u}_3$ leads to a decrease of the convective time associated with the flame. This additional, independent, time-lag affects the ITA frequencies in a similar way as the time-lag due to swirl wave propagation as discussed above.

As can be expected from the dispersion relation (36), the inertial length L_I also has an effect on the ITA frequencies. The two limiting cases $L_I \to 0$ (no constriction) and $L_I \to \infty$ (substantial constriction) were examined analytically. For $L_I \to 0$, the ITA frequencies followed the previously found criterion,[43] which states that the phase of the FTF has to be π. For $L_I \to \infty$, the criterion has to be modified, requiring a phase of $\pi/2$.

The discrepancies between the peaks in the measured frequency spectrum and the predicted ITA frequencies (see Figure 27) was due to oversimplified modelling assumptions: non-reflective inlet and outlet, and uniformly cold and hot conditions in the components of the combustion rig.
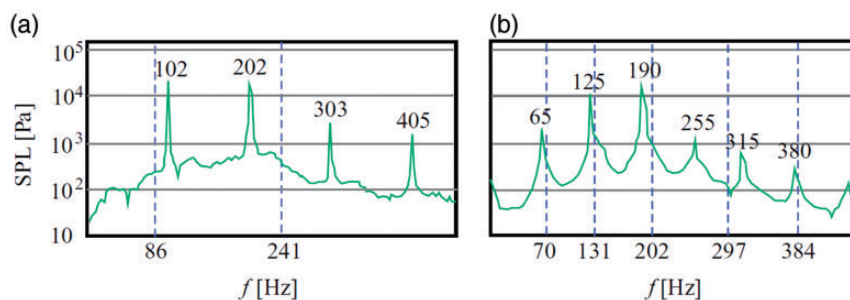

Figure 27. Green curve: measured SPL as a function of frequency. Dashed vertical lines: predicted ITA frequencies. Results are shown for two distances between swirler and combustion chamber: (a) 0.03 m and (b) 0.13 m (after Figure 4 in Albayrak et al.[48]).

6.4. Intrinsic modes in a laboratory swirl burner – Flame modelled by FTF from CFD simulations

Iurashev et al.[50] studied the BRS burner shown in Figure 13 with a hybrid approach: first, the FTF of the flame was calculated with CFD, giving data points in the frequency range [0,...500 Hz]. This FTF data was approximated by an analytical expression representing a low-pass filter with damping and a time-lag τ. The analytical expression for the FTF was incorporated in a low-order network model from which the frequency and growth rate of the dominant mode were calculated. This work was subsequently extended in Iurashev:[35] the effects of various parameters were investigated, in particular of the combustion chamber length L and of the reflection coefficient R_{out} at the outlet.

Figures 28(a) and (b) show, respectively, the frequency and growth rate as a function of L, for three boundary conditions at the outlet: $R_{out} = -0.4$ (lossy open end), $R_{out} = 0.4$ (lossy closed end), $R_{out} = 0$ (non-reflective end).

For $R_{out} = -0.4$, we observe the following behaviour. As the length of the combustion chamber increases, the dominant frequency first increases and then decreases smoothly until $L = 2.2$m. There, the frequency jumps from 100 to 132 Hz and then decreases again until $L = 5.8$m. This pattern repeats along the L-axis at intervals of $\Delta L = 3.6$ m (apart from a slight reduction of the maximum and minimum frequency values). The growth rate fluctuates between negative (stable) and positive (unstable) values, and it, too, behaves in a repetitive manner with intervals of 3.6 m. This interval is significant: it corresponds to half the acoustic wavelength at 118 Hz, which is the frequency of the dominant mode for the non-reflective outlet (see red line in Figure 28). Similar behaviour is observed for $R_{out} = 0.4$, except that the curves are shifted by $\Delta L/2$ along the L-axis.

The rather limited variation of the frequency (only between 100 and 134 Hz), over a large range of combustion chamber lengths, is a clear indication that the modes in Figure 28 are ITA modes.

The case $R_{out} = 0$ is of particular interest, because it represents an anechoic end, i.e. the combustion chamber ceases to be an acoustic resonator. Modes driven by thermoacoustic feedback cannot be sustained in this case. However, there is clearly an unstable mode; this can only be an ITA mode.

Simulations with more elaborate flame models (three time-lags, rather than just a single time-lag; amplitude-dependent FTF) were performed in Iurashev et al.[33] Parameter studies again gave clear evidence for the presence of an unstable ITA mode: its frequency was almost independent of the temperature in the combustion chamber.

In his thesis,[35] Iurashev performed many parametric studies to explore possible ways of suppressing an ITA mode in the BRS burner. He found that the most promising strategy is to reduce the cross-section of the burner tube. Further simulations with different R_{out} and different L gave results similar to those shown in Figure 28. This suggests that modifying the length or end conditions of the combustion chamber are ineffective strategies to control ITA modes. The same explanation was offered in Emmert et al.[51]

7. Transport phenomena in premixed flames

This section considers various aspects relating to the propagation of fluctuations in two flow quantities:

- components of the velocity vector,
- equivalence ratio.

When such fluctuations meet the flame, they induce fluctuations Q' in the flame's rate of heat release. Velocity fluctuations $\mathbf{u}'$ distort the flame shape, thereby inducing fluctuations A' in the flame surface area. The effect of equivalence ratio fluctuations ϕ' is more complex and divides into direct and indirect effects. The direct effects are the fluctuations in heat release rate due to fluctuations $\Delta H'$ in the heat of reaction and fluctuations S'_L
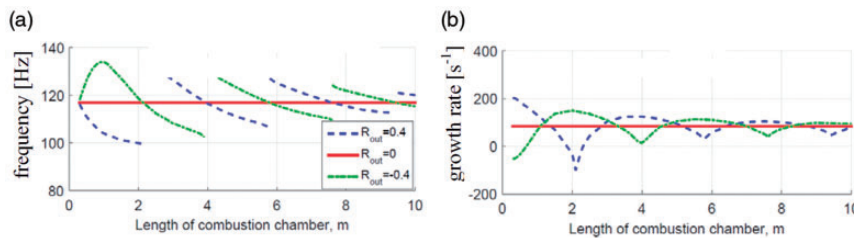

Figure 28. Frequency and growth rate of the dominant mode for various lengths of the combustion chamber and for three outlet boundary conditions. (a) Frequency and (b) Growth rate (from Figure 3.29 in Iurashev[35]).
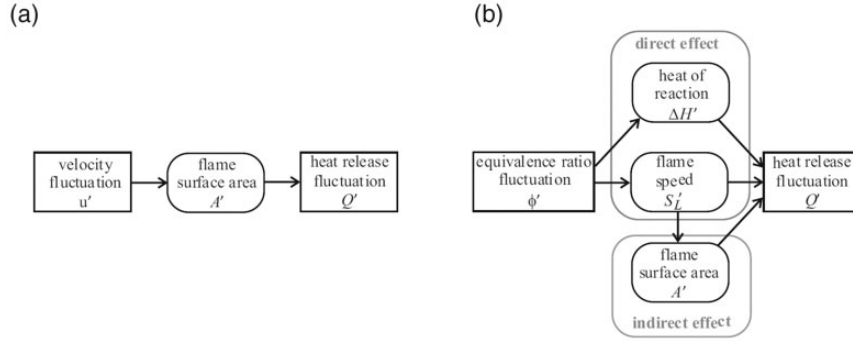
Figure 29. Processes generating fluctuations in heat release rate caused by (a) velocity fluctuations **u**′, and (b) equivalence ratio fluctuations ϕ' (after Figure 3 in Cho and Lieuwen[52]).

in the flame speed, both of which are induced by fluctuations ϕ'. The indirect effect arises because S'_L also generates changes in the flame surface area.

Figure 29 summarises how fluctuations **u**′ in velocity and fluctuations ϕ' in equivalence ratio induce fluctuations Q' in the heat release rate.

Albayrak et al.[53–57] have studied these processes from a fundamental perspective. Their work is described in the following three subsections. Section 7.1 presents an initial study, which investigates the intricacies of swirl wave propagation in a cylindrical duct; it does not include a flame. This piece of work is largely analytical. Section 7.2 considers a swirl flame exposed to a flow with a fluctuating velocity vector. This study is predominantly numerical. Section 7.3 considers a conical flame exposed to fluctuations in equivalence ratio. This study is predominantly analytical. It calculates the response of the heat release rate to a superposition of three disturbances ($\Delta H'$, S'_L, A'), each excited by an impulsive perturbation of the equivalence ratio. This time-domain approach is well-suited to the identification of the time delays introduced by various transport phenomena. A cylindrical geometry is considered throughout, as well as incompressible flow.

7.1. Propagation of swirl waves in a cylindrical duct

Swirl waves are generated when an acoustic wave passes through a swirler. These travel much more slowly than the acoustic wave. It is commonly assumed (in particular in 1D models) that their speed is equal to the speed of the mean flow, i.e. that swirl waves travel with convection. Albayrak and Polifke[53,54] scrutinise this assumption with an approach, based on the 3D incompressible flow equations. They consider the flow field downstream of a swirler in a cylindrical duct (see Figure 30, with $b = 0$ (no inner cylinder)).

The velocity components are u_z, u_r, u_θ; these have a mean part (denoted by an overbar) and a fluctuating part (denoted by a prime).
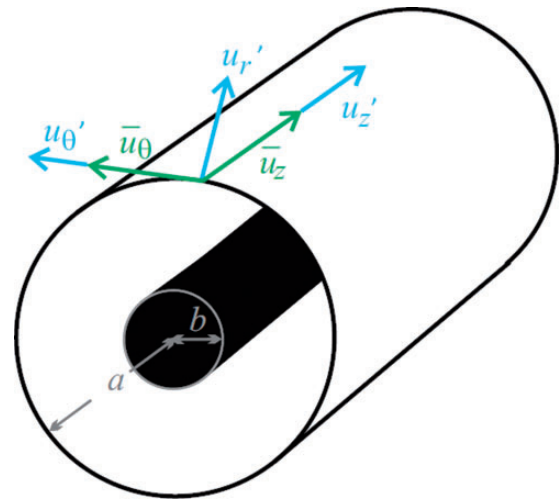

Figure 30. Annular cylindrical duct with outer radius a and inner radius b.

The principal assumptions of the analysis were:

– inviscid and incompressible flow,
– axisymmetric flow, i.e. $\frac{\partial}{\partial\theta} = 0$,
– no mean flow in the radial direction, i.e. $\bar{u}_r = 0$,
– $\bar{u}_z$ is uniform,
– the fluctuating velocities u'_z, u'_r, u'_θ are small compared with the mean velocities $\bar{u}_z$, $\bar{u}_\theta$.

Under these assumptions, the flow field can be described by the linearised Euler equations, which can be simplified to give the partial differential equations (PDEs) shown below

$$\frac{u'_r}{r} + \frac{\partial u'_r}{\partial r} + \frac{\partial u'_z}{\partial z} = 0 \qquad (38)$$

$$\frac{\partial u'_z}{\partial t} + \bar{u}_z \frac{\partial u'_z}{\partial z} = -\frac{1}{\rho}\frac{\partial p'}{\partial z} \qquad (39)$$

$$\frac{\partial u_r'}{\partial t} + \bar{u}_z \frac{\partial u_r'}{\partial z} - \frac{2\bar{u}_\theta u_\theta'}{r} = -\frac{1}{\rho}\frac{\partial p'}{\partial r} \quad (40)$$

$$\frac{\partial u_\theta'}{\partial t} + \bar{u}_z \frac{\partial u_\theta'}{\partial z} + u_r' \frac{\partial \bar{u}_\theta}{\partial r} + \frac{u_r'\bar{u}_\theta}{r} = 0 \quad (41)$$

Equations (38) to (41) form a set of four coupled first-order PDEs for the fluctuating quantities $u_r', u_\theta',$ u_z' and p'; the independent variables are r, z and t. By applying the Fourier transform with respect to the variables t and z, $u'(t, z, r)\mathrm{e}^{-\mathrm{i}\omega t + \mathrm{i}k_z z} \rightarrow \hat{u}(\omega, k_z, r)$, the PDEs can be turned into ordinary differential equations (ODEs) with independent variable r. Again, the ODEs are coupled and first-order. By a string of manipulations (differentiation with respect to r, successive elimination), they can be decoupled, resulting in four separate second-order ODEs for $\hat{u}_r$, $\hat{u}_\theta$, $\hat{u}_z$ and $\hat{p}$. These ODEs are Bessel equations; the ones for $\hat{u}_z$ and $\hat{p}$ are zero-order, and the ones for $\hat{u}_r$ and $\hat{u}_\theta$ are first-order Bessel equations. For example, the ODE found for $\hat{u}_r$ is

$$\frac{\mathrm{d}^2 \hat{u}_r}{\mathrm{d}r^2} + \frac{1}{r}\frac{\mathrm{d}\hat{u}_r}{\mathrm{d}r} - \hat{u}_r \left[\frac{1}{r^2} - k_r^2\right] = 0 \quad (42)$$

In order to take this further, the dependence of $\bar{u}_\theta$ on r is required. Albayrak and Polifke[54] chose $\bar{u}_\theta = \Gamma r$ (solid body rotation with circulation strength Γ) because then the above ODE simplifies, giving

$$\frac{\mathrm{d}^2 \hat{u}_r}{\mathrm{d}r^2} + \frac{1}{r}\frac{\mathrm{d}\hat{u}_r}{\mathrm{d}r} - \hat{u}_r \left[\frac{1}{r^2} - k_r^2\right] = 0 \quad (43)$$

with

$$k_r = k_z \frac{\sqrt{4\Gamma^2 - (\omega - \bar{u}_z k_z)^2}}{\omega - \bar{u}_z k_z} \quad (44)$$

The Bessel functions of first order, $J_1(k_r r)$ (first kind) and $Y_1(k_r r)$ (second kind) form a basis of solutions. The quantity k_r, defined by (44) can be interpreted as wave number in the radial direction.

The analysis is simplified for the special case, where $b = 0$ (i.e. the inner cylinder is absent, see Figure 30). In this case, the point $r = 0$, where $Y_1(k_r r)$ has a singularity, is inside the domain of interest; therefore only the solution $J_1(k_r r)$ is included

$$\hat{u}_r(r) \sim J_1(k_r r) \quad (45)$$

The allowed values of k_r are determined from the boundary condition at the cylinder wall, which is rigid

$$\hat{u}_r(r)\big|_{r=a} = 0 \quad (46)$$

This leads to the implicit equation

$$J_1(k_r a) = 0 \quad (47)$$

which has discrete solutions $k_{rn} = j_n/a$ ($n = 1, 2, 3, \ldots$), where j_n denotes the nth zero of the Bessel function, i.e. $J_1(j_n) = 0$. n is the mode number; it gives the number of nodal circles in a cross-section of the cylinder.

The phase speed, $v_p = \omega/k_z$, can then be calculated from (44); there are two results

$$v_{p,n} = \bar{u}_z \pm 2\Gamma \frac{a}{\sqrt{k_z^2 a^2 + j_n^2}} \quad (48)$$

This indicates that there are *two* inertial waves propagating downstream: one is faster and the other one is slower than convection. The difference in their propagation speed is given by the term $4\Gamma a/\sqrt{k_z^2 a^2 + j_n^2}$, which depends on the circulation strength Γ, the frequency and the mode number n:

– The difference increases with circulation strength, i.e. with the mean tangential velocity.
– The difference also depends on frequency: it is maximal for $\omega = 0$ and then decreases monotonically; for large frequencies, the speed of both waves tends to $\bar{u}_z$ (concluded from numerical evaluation of (48)).
– With increasing mode number n, $j_n \rightarrow (n + \frac{1}{4})\pi$, and the speed of both waves tends to $\bar{u}_z$.

The results have been successfully validated with numerical simulations.

In further work, Albayrak[58] considered an annular duct with outer radius a and inner radius b (see Figure 30). They derived the dispersion relation and obtained an expression, which is an extended version of (48). The same conclusions apply: there are two inertial waves propagating downstream; one has a phase speed greater than the convection speed $\bar{u}_z$, and the other has a phase speed lower than that. The deviation from $\bar{u}_z$ is largest at low frequencies ($v_{p,n} = \bar{u}_z \pm 50\%$ for $\omega \approx 0$ and $n = 1$). In the limits $\Gamma \rightarrow 0$, $\omega \rightarrow \infty$, $n \rightarrow \infty$, the speed of both waves tends to $\bar{u}_z$.

Albayrak et al. also calculated the radial profile of the three velocity components of the swirl wave and found the following results[55]

$$\hat{u}_r(r) \sim M_1(k_r r) = J_1(k_r r) - \frac{J_1(k_r a)}{Y_1(k_r a)} Y_1(k_r r) \quad (49a)$$

$$\hat{u}_\theta(r) \sim M_1(k_r r) = J_1(k_r r) - \frac{J_1(k_r a)}{Y_1(k_r a)} Y_1(k_r r) \quad (49b)$$

$$\hat{u}_z(r) \sim M_0(k_r r) = J_0(k_r r) - \frac{J_1(k_r a)}{Y_1(k_r a)} Y_0(k_r r) \quad (49c)$$

The allowed values of k_r are the roots of the equation

$$M_1(k_r r)\big|_{r=b} = 0 \qquad (50)$$

Important results, which will be used in section 7.2, are summarised below.

- When an acoustic wave travels across a swirler, a swirl wave is generated. This wave acquires velocity components in all three spatial directions (r, θ, z) as it travels along an annular duct.
- Each velocity component has a distinctive profile in the r-direction, described by Bessel functions.
- The swirl wave is dispersive: an initial velocity impulse loses its sharp spike-shaped profile and develops a wider profile as the wave travels along the z-axis.

7.2. Effect of swirl waves and vorticity waves on a swirl flame

When a swirl wave with velocity components u'_r, u'_θ, u'_z meets a rotationally symmetric flame, the azimuthal component u'_θ has no effect, but the radial and axial components do: they modulate the rate of heat released by the flame. In order to investigate this in detail, Albayrak et al.[55] developed a fast and accurate numerical tool to calculate the heat release rate. Their starting point was the set of reacting flow equations given below

$$\nabla \cdot \mathbf{u} = \frac{1}{\rho c_p T}[\nabla \cdot (\kappa \nabla T) + q] \qquad (51a)$$

$$\frac{D\mathbf{u}}{Dt} = -\frac{1}{\rho}\nabla p + \frac{1}{\rho}\nabla \cdot (\mu \nabla \mathbf{u}) \qquad (51b)$$

$$\frac{DY_F}{Dt} = \frac{1}{\rho c_p}[\nabla \cdot (\kappa \nabla Y_F) + \dot{\omega}_F] \qquad (51c)$$

$$\frac{DT}{Dt} = \frac{1}{\rho c_p}[\nabla \cdot (\kappa \nabla T) + q] \qquad (51d)$$

The following notation has been used. $\mathbf{u}$ is the velocity vector, ρ is density, p is pressure, Y_F is the mass fraction of the fuel, T is temperature, $\dot{\omega}_F$ is the reaction rate, q is the heat release rate per unit volume, c_p is the heat capacity at constant pressure, κ is the thermal conductivity and μ is the dynamic viscosity.

The governing equations above are valid for the following conditions:

- incompressible flow of low Mach number,
- binary air–fuel mixture,
- heat capacity of the mixture independent of temperature and close to the value for air,
- fuel with Lewis number 1.

The density was calculated from the perfect gas equation

$$p = R\rho T \qquad (52)$$

where R is the specific gas constant. Given that the flow is assumed to be incompressible, the density was treated as a function of temperature only, not of pressure.

The reaction rate, heat release rate, viscosity and thermal conductivity were modelled by the following equations

$$\dot{\omega}_F = -A_r \rho Y_F e^{-T_a/T}$$
(irreversible one-step Arrhenius law) $\qquad (53a)$

$$q = -\Delta h_f^0 \, \dot{\omega}_F \qquad (53b)$$

$$\mu = \frac{A_S T^{3/2}}{T + T_S} \qquad (53c)$$
(Sutherland's viscosity model)

$$\kappa = \kappa_1 \frac{T}{T_1} \qquad (53d)$$

A_r is the pre-exponential factor; this was treated as a fitting parameter to give the correct values for the laminar flame speed ($A_r = 2.25 \times 10^9 \, \text{s}^{-1}$). T_a is the activation temperature ($T_a = 18,584 \, \text{K}$), and Δh_f^0 is the mass enthalpy of formation of fuel ($\Delta h_f^0 = 2.44 \times 10^6 \, \text{J/kg}$). A_S and T_S are the constants in Sutherland's viscosity model ($A_S = 1.672 \times 10^{-6} \, \text{kg}/(\text{sm}\sqrt{\text{K}})$, $T_S = 170 \, \text{K}$). κ_1 is the thermal conductivity of the fluid at inlet temperature T_1 ($\kappa_1 = 0.0257 \, \text{W}/(\text{mK})$, $T_1 = 293 \, \text{K}$). For R, the value of air was used ($R = 287 \, \text{m}^2/(\text{s}^2\text{K})$).

The set of equations (51) was split into two sets: one for the steady-state quantities and one for the fluctuating quantities. The steady-state equations, which are nonlinear, determine the fields $\bar{\mathbf{u}}$, $\bar{Y}_F$, $\bar{T}$ and $\bar{p}$. The other set of equations was linearised with respect to the fluctuating quantities, and so the 'linearised reactive flow' (LRF) equations were obtained; they form a set of four equations for $\mathbf{u}'$, Y'_F, T' and p'.

Both sets of equations were discretised in space with finite elements (Freefem++ with P2–P1 Taylor-Hood elements). $\mathbf{u}$, Y_F, T were discretised by second-order polynomials, and p by first-order polynomials. The steady-state equations were solved with Newton's method. The LRF equations were solved in the time domain by using an implicit backwards Euler scheme to advance in time.

Boundary conditions for both steady-state and fluctuating quantities were prescribed at the inlet. The global heat release rate was obtained by integrating $\bar{q}$ and q' over the volume of the flame, e.g. $\bar{Q} = \int \bar{q} \, dV$.

This numerical tool was tested extensively by comparing its predictions for the FTF with measurements on a lean methane–air Bunsen flame. It was then applied to an academic setup with a laminar swirling V-flame, which is shown in Figure 31. The geometry is cylindrical, and the flow field is rotationally symmetric. The length of the annular duct was 5 mm, and that of the combustion chamber was 10 mm.

First the steady-state equations were solved. The inlet velocity

$$\bar{\mathbf{u}}(r,z)\big|_{z=0} = \begin{bmatrix} \bar{u}_r \\ \bar{u}_\theta \\ \bar{u}_z \end{bmatrix}_{z=0} = \begin{bmatrix} 0 \\ \Gamma r \\ \bar{u}_z \end{bmatrix} \tag{54}$$

was imposed (describing axial bulk flow with solid-body rotation), with $\Gamma = 1000 \text{ s}^{-1}$, $\bar{u}_z = 2$ m/s. This gave the mean heat release $\bar{Q}$.

Next, the LRF equations were solved. The inlet conditions were chosen so as to simulate an impulsive perturbation, comprising an 'acoustic wave' and a swirl wave, coming from the swirler. The acoustic impulse was described by the inlet boundary condition

$$u_z'(r,\theta,z,t)\big|_{z=0} = \bar{u}_z \varepsilon \delta(t) \tag{55}$$

where ε is a small dimensionless quantity and gives the relative strength of the perturbation. (Given that an incompressible fluid is considered here, the term 'acoustic wave' denotes an axial wave with a propagation speed that tends to infinity.) The swirl impulse at the inlet was described by

$$\mathbf{u}'(r,\theta,z,t)\big|_{z=0} = \begin{bmatrix} u_r' \\ u_\theta' \\ u_z' \end{bmatrix}_{z=0} \sim \bar{u}_z \, \varepsilon \, \delta(t)(\tan\alpha) \begin{bmatrix} 0 \\ M_1(k_{r1}r) \\ 0 \end{bmatrix} \tag{56}$$
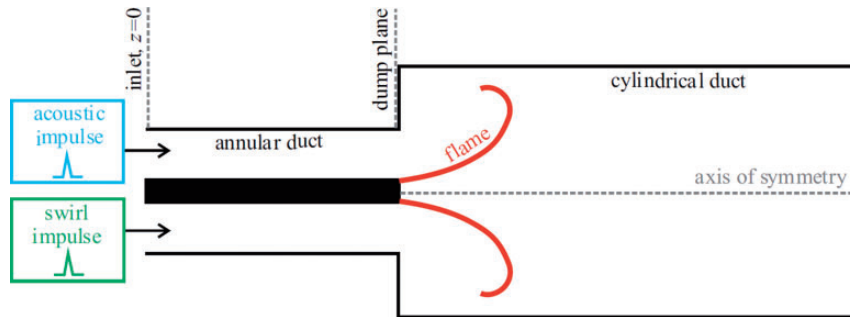
where α denotes the swirl angle, which determines the strength of the swirl wave. $M_1(k_{r1}r)$ is given by (49a), i.e. the r-dependence of u_θ' at the inlet corresponds to the first radial mode identified in section 7.1. k_{r1} is the radial wave number of this mode and given by the lowest positive root of (50). For simplicity, higher-order modes have been neglected. The global heat release rate Q' was obtained by integrating q' over the volume of the flame.

Given that the flame was excited by an impulsive velocity field, the resulting heat release rate fluctuations are the flame's IR, denoted by

$$h(t) = \frac{Q'(t)}{\bar{Q}\varepsilon} \tag{57}$$

Predicted results are shown in Figure 32. Part (a) shows the response, $h_A(t)$, to excitation with the acoustic wave impulse described by (55), and part (b) shows
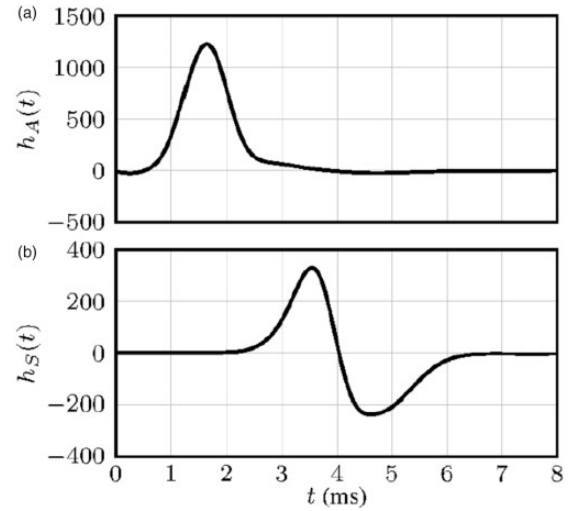
Figure 32. Impulse responses of the flame. (a) Response to the acoustic impulse (55) and (b) Response to the swirl impulse (56) (from Figure 7(c) in Albayrak et al.[55]).

Figure 31. Academic configuration of a laminar swirl flame in a dump combustor.

the response, $h_S(t)$, to excitation with the swirl wave impulse described by (56).

Three time-lags are observed:

– When the acoustic wave crosses the dump plane, a vorticity wave (with fluctuating velocity components in the axial and radial direction) is generated due to jet formation and vortex roll-up. The maximum at about 1.6×10^{-3}s in Figure 32(a) corresponds to the time for the vorticity wave to travel from the dump plane to the flame surface.
– The maximum at about 3.5×10^{-3}s in Figure 32(b) corresponds to the time it takes the swirl wave to travel from the inlet to the flame surface.
– The minimum at about 5.5×10^{-3}s in Figure 32(b) is due to the flame restoration mechanism suggested in Blumenthal et al.[59]

The result shown in Figure 32(b) clearly shows that the flame reacts to a swirl wave. This may be surprising at first, because the flame is rotationally symmetric and the swirl wave has only an azimuthal component when it leaves the swirler (see (56)). The findings from section 7.1 can resolve this apparent conundrum: As the swirl wave travels along the annular duct, from the swirler to the dump plane, it acquires velocity components in the *radial and axial* direction (u'_r and u'_z), and it is these components that distort the flame surface and hence perturb the heat release rate. The physical mechanisms behind the generation of the components u'_r and u'_z are thought to be Coriolis forces, but further research is needed to substantiate this theory.

7.3. Analytical models for the effect of equivalence ratio fluctuations on premixed flames

Premixed flame dynamics is not only driven by velocity fluctuations, but also by fluctuations of the equivalence ratio ϕ. In Albayrak et al.,[56] the response of a conical premixed flame to an impulsive perturbation of ϕ was studied analytically. The investigation was based on the equation

$$Q(t) = \int_A \rho\, \Delta H\, S_L \, \mathrm{d}A \qquad (58)$$

which expresses the global heat release rate of the flame in terms of an integral over the instantaneous flame surface. ρ is the density of the unburnt gas (considered constant), ΔH is the heat of reaction, S_L is the laminar flame speed, and $\mathrm{d}A$ is an infinitesimal area element of the flame surface. ΔH, S_L and the flame surface area A

depend on the local values of the equivalence ratio ϕ. Hence, if ϕ fluctuates, Q fluctuates, as described by

$$\frac{Q'(t)}{\bar{Q}} = \int_f \frac{\Delta H'}{\Delta \bar{H}} \frac{\mathrm{d}A}{\bar{A}} + \int_f \frac{S'_L}{\bar{S}_L} \frac{\mathrm{d}A}{\bar{A}} + \frac{A'(t)}{\bar{A}} \qquad (59)$$

The mechanisms by which ϕ-fluctuations induce Q-fluctuations are shown in Figure 29(b).

A rotationally symmetric conical flame was considered. Its motion was modelled with a flame-tracking approach (the G-equation), which was linearised and simplified for the case where the flame displacement can be described by a single-valued function of r (radial coordinate). The flame base (at $z = 0$) was assumed to be permanently anchored on the flame holder. An impulsive ϕ-perturbation was imposed at $z = 0$, and its propagation (due to convection with the bulk velocity $\bar{u}_z$ in the axial direction) was modelled by

$$\phi'(z, t) = \bar{\phi}\, \varepsilon\, \delta\!\left(t - \frac{z}{\bar{u}_z}\right) \qquad (60)$$

The analysis was performed in the time domain. The IR was determined individually for the three contributions from ΔH, S_L and A (see (59) and Figure 29(b)).

Two principal delay mechanisms, each with its own time-scale, were revealed:

– a *convective* time-scale τ_c; this is associated with the transport of ϕ-perturbations, travelling from the flame base to the flame tip, with axial velocity $\bar{u}_z$.
– a *restorative* time-scale τ_r; this is associated with the restoration mechanism (identified by Blumenthal et al.[59]), which re-establishes the original, unperturbed flame shape after the ϕ-perturbation has passed.

Albayrak et al.[56] found that contributions from ΔH and S_L are governed only by τ_c, whereas the contribution from A is controlled by both, τ_c and τ_r.

The model was extended to simulate the case, where the base of the flame is perturbed by a Gaussian, rather than a δ-shaped distribution, i.e. (60) was replaced by

$$\phi'(z, t) = \bar{\phi}\varepsilon \sqrt{\frac{1}{\pi \tau_d t}}\, e^{-\frac{1}{\tau_d t}\left(t - \frac{z}{\bar{u}_z}\right)^2} \qquad (61)$$

Such a distribution arises when a δ-shaped ϕ-impulse, imposed some distance upstream of the flame, experiences molecular diffusion and hence changes its shape to become wider and flatter with time, i.e. is subject to dispersion. $\tau_d = 4D/\bar{u}_z^2$ is the diffusive time-scale, where D denotes the diffusion coefficient. In contrast to τ_c and τ_r, τ_d is not associated with the travelling time of some
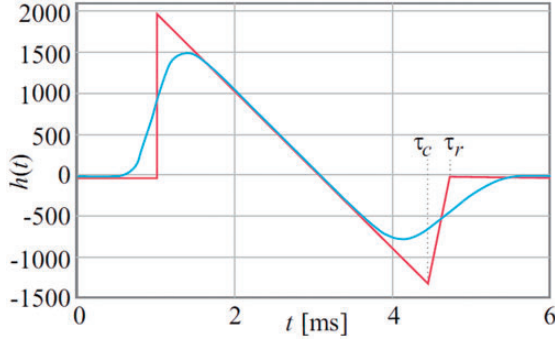
Figure 33. Impulse response combining the perturbations in ΔH, S_L and A. Red curve: without diffusion. Blue curve: with diffusion (after Figure 7 in Albayrak et al.[56]).

Figure 34. Overall impulse response. Solid line: uniform profile. Dashed line: parabolic profile (from Figure 4 in Albayrak and Polifke[54]).

perturbation, but it is a measure how quickly the wave profile gets distorted by diffusion.

Again, the IR was calculated analytically. This was done individually for the effects on ΔH, S_L and A. The sum of the individual IRs is shown in Figure 33 for the following parameter values: $r_0 = 10^{-3}$ m, $\bar{\phi} = 0.8$, $\bar{u}_z = 1$ m/s, $\bar{S}_L = 0.278$ m/s, $\varepsilon = 0.05$, $D = 0.22 \times 10^{-4}$ m^2/s; the length of the mixing duct was 1 mm.

The red curve denotes the case *without* diffusion, i.e. $\phi'(z,t)$ is given by (60); the blue curve denotes the case *with* diffusion, i.e. $\phi'(z,t)$ is given by (61). The effect of the diffusion is to make the response smoother and longer-lasting.

Validation against numerical simulations gave very good qualitative agreement with the analytical results predicted from the model with diffusion.

The studies described so far in this section assume that the ϕ-fluctuations are uniform all over the plane perpendicular to the flame axis. This assumption becomes invalid for combustion systems, where the air and fuel are not perfectly mixed (technically premixed flames), and hence some degree of non-uniformity arises in the ϕ-fluctuations.

Albayrak and Polifke[54] extended their analytical model to include such non-uniformities. A simplistic profile, given by the quadratic expression

$$\phi'(r,z,t) = \bar{\phi}\varepsilon 2\left(1 - \frac{r}{r_0}\right)\left(1 + \frac{r}{r_0}\right)\delta\left(t - \frac{z}{\bar{u}_z}\right) \quad (62)$$

(where r_0 is the radius of the flame base) was assumed because this case could be handled analytically. It represents an upside-down parabola with its maximum at the centre ($r = 0$). This could serve as a model for a technically premixed case with the fuel injector located at the centre of a mixing duct that is too short to achieve perfect mixing. Predictions for the IR are shown in Figure 34 for the non-dissipative case ($D = 0$), otherwise
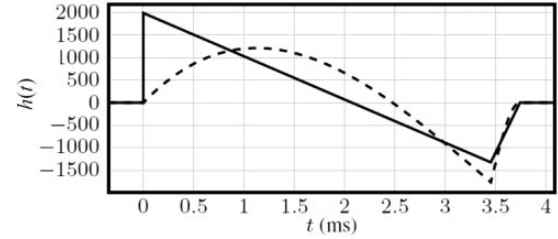
the parameters were the same as for Figure 33. The dashed curve is for the parabolic profile, and the solid curve for the uniform profile described by (60). The impulse was applied at the end of the mixing duct, so there was no time delay before it reached the flame.

The initial response to the parabolic profile is less steep because the ϕ-perturbation is weaker at the periphery than at the centre. The key time-lags, however, are the same: $\tau_c = 3.45 \times 10^{-3}$ s (flame distortion due to convection) and $\tau_r = 3.75 \times 10^{-3}$ s (flame restoration).

Also, the corresponding FTFs were calculated. The gain curves turned out to be quite similar. However, considerable deviation was observed for the phase curves; this is significant, because the phase of the FTF has a major influence on the thermoacoustic stability behaviour.

8. Moving heat sources and their effect on acoustic waves and entropy waves

In 1D analytical modelling, the flame is commonly assumed to be a compact heat source and treated as a planar interface, which separates the reactants from the combustion products. An additional assumption, which has been scrutinised by Strobio Chen et al.[60–63] is the following: the heat source is fixed in space, and mass, momentum and energy satisfy conservation equations across the fixed interface. This assumption is justified for stationary heat sources, such as the hot gauze in a Rijke tube. A flame, however, is dynamic, and it moves even in a 1D environment.

Strobio Chen et al.[60,61] detected contradictions and unphysical behaviours predicted from models that treat a premixed flame as a stationary discontinuity. In order to resolve these issues, they revisited Chu's conservation equations across a moving heat source[64,65] for the 1D setting shown in Figure 35. The velocity of the heat source was denoted by $u_s(t)$; the key field quantities were u (velocity), p (pressure) and ρ (mass density). $q(t)$ is the heat release rate per cross-sectional area (units W/m^2); it plays two roles: it generates a jump in mean temperature, from $\bar{T}_1$ to $\bar{T}_2$, and it acts as a source of waves.
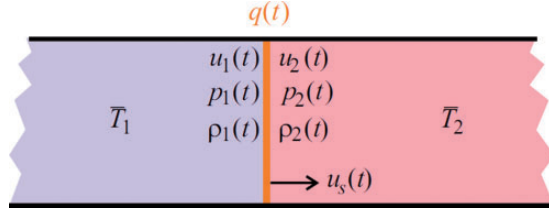
Figure 35. Compact heat source moving with velocity $u_s(t)$ and heat release rate q, separating the upstream field quantities $u_1(t)$, $p_1(t)$, $\rho_1(t)$ from the downstream ones, $u_2(t)$, $p_2(t)$, $\rho_2(t)$ (after Figure 1 in Strobio Chen et al.[61]).

Chu's conservation equations read

$$\rho_2(u_2 - u_s) = \rho_1(u_1 - u_s) \quad \text{(mass)} \tag{63}$$

$$\rho_2 u_2(u_2 - u_s) + p_2 = \rho_1 u_1(u_1 - u_s) + p_1 \quad \text{(momentum)} \tag{64}$$

$$\rho_2 E_2(u_2 - u_s) + u_2 p_2 = \rho_1 E_1(u_1 - u_s) + u_1 p_1 + q \quad \text{(energy)} \tag{65}$$

where E_1, E_2 are the mass-specific total (internal plus kinetic) energy.

For $u_s = 0$, these conservation equations reduce to the standard jump conditions, prevalent in one-dimensional analytical models (e.g. in Dowling[66]).

Strobio Chen et al.[60,61] simplified Chu's conservation equations (63) to (65) by making the following assumptions:

- The gas mixtures on either side of the flame are perfect gases.
- The specific heats c_p, c_v are uniform across the heat source.
- The field quantities, e.g. $u_2(x, t) = \bar{u}_2(x) + u_2'(x, t)$, have small fluctuating parts (denoted with a prime $'$), and only linear terms in the fluctuating parts need to be included in the conservation equations.
- The heat source oscillates around a mean position, i.e. $u_s(t) = \bar{u}_s + u_s'(t)$ with $\bar{u}_s = 0$.
- The Mach number is low, i.e. terms of order $O(M^2)$ can be neglected.

This leads to a set of three linear equations, relating the downstream quantities u_2', p_2', ρ_2' to their upstream counterparts u_1', p_1', ρ_1', as well as to the heat release rate q' and to the heat source velocity u_s'.

Two types of wave can potentially be generated (as well as reflected and transmitted) by the heat source:

- acoustic waves, characterised by velocity and pressure fluctuations, u' and p'

- entropy waves (or convected hot spots) characterised by entropy fluctuations s'

Density fluctuations are involved in both wave types; in order to be able to distinguish between acoustic waves and entropy waves, the density fluctuations were split up

$$\frac{\rho'}{\bar{\rho}} = \frac{p'}{\gamma \bar{p}} - \frac{s'}{c_p} \tag{66}$$

The resulting equations were non-dimensionalised and written in matrix form

$$\begin{bmatrix} \frac{u_2'}{\bar{u}_2} \\ \frac{p_2'}{\bar{p}_2} \\ \frac{s_2'}{c_p} \end{bmatrix} = \begin{bmatrix} T_{12} & T_{12} - 1 & 0 \\ 0 & 1 & 0 \\ T_{12} - 1 & T_{12} - 1 & 1 \end{bmatrix} \begin{bmatrix} \frac{u_1'}{\bar{u}_1} \\ \frac{p_1'}{\bar{p}_1} \\ \frac{s_1'}{c_p} \end{bmatrix}$$

$$+ \begin{bmatrix} 1 - T_{12} \\ 0 \\ 1 - T_{12} \end{bmatrix} \frac{q'}{\bar{q}} + \begin{bmatrix} 0 \\ 0 \\ 1 - T_{12} \end{bmatrix} \frac{u_s'}{\bar{u}_1} \tag{67}$$

where

$$T_{12} = \frac{\bar{T}_1}{\bar{T}_2} \tag{68}$$

is a measure of the temperature jump. This equation describes how the downstream fluctuations u_2', p_2', s_2' respond to

- fluctuations of the upstream field quantities u_1', p_1', s_1',
- heat release rate fluctuations q',
- heat source movement u_s'.

The fluctuations in heat release rate do not come from an autonomous heat source, but they depend on the properties of the flame and the flow field. In order to take the interpretation of (67) further, Strobio Chen et al.[61] considered a ducted premixed flame and modelled its heat release rate analytically by the quasi-1D relationship

$$q = \rho_1 \, \dot{V} \, \Delta H \tag{69}$$

This is based on the following rationale: $\dot{V}$ is an effective 1D flame speed (the rate of volume consumption of the premix per duct cross-sectional area; units m/s), defined by $A_d \dot{V} = A_f S_L$, where A_d is the cross-sectional area of the duct, A_f is the area of the (wrinkled) flame surface, and S_L is the laminar flame speed. ΔH is the heat of reaction per unit mass of mixture (units J/kg)

and depends on the equivalence ratio; for small fluctuations, one can write

$$\frac{\Delta H'}{\overline{\Delta H}} = \frac{\phi'}{\bar{\phi}} \qquad (70)$$

By combining (69) with (70) and (66), the fluctuations of q can be written as

$$\frac{q'}{\bar{q}} = \frac{\dot{V}'}{\overline{\dot{V}}} + \frac{\phi'}{\bar{\phi}} + \frac{1}{\gamma}\frac{p'_1}{\bar{p}_1} - \frac{s'_1}{c_p} \qquad (71)$$

The difference between the effective flame speed $\dot{V}$ and the upstream flow velocity u'_1 causes the flame to move from its mean position. This is expressed by the kinematic balance at the premixed flame front

$$\dot{V}(t) = u_1(t) - u_s(t) \qquad (72)$$

After use of (72) to substitute for $\dot{V}$, the matrix equation (67) becomes

$$\begin{bmatrix} \frac{u'_2}{\bar{u}_2} \\ \frac{p'_2}{\bar{p}_2} \\ \frac{s'_2}{c_p} \end{bmatrix} = \begin{bmatrix} 1 & (1-\gamma^{-1})(T_{12}-1) & 0 \\ 0 & 1 & 0 \\ 0 & (1-\gamma^{-1})(T_{12}-1) & 1 \end{bmatrix} \begin{bmatrix} \frac{u'_1}{\bar{u}_1} \\ \frac{p'_1}{\bar{p}_1} \\ \frac{s'_1}{c_p} \end{bmatrix}$$
$$+ \begin{bmatrix} 1-T_{12} \\ 0 \\ 1-T_{12} \end{bmatrix}\frac{\phi'}{\bar{\phi}} + \begin{bmatrix} T_{12}-1 \\ 0 \\ 0 \end{bmatrix}\frac{u'_s}{\bar{u}_1} \qquad (73)$$

There are usually no entropy fluctuations upstream of a flame, i.e. $s'_1 = 0$, and the last line of this equation can then be written as

$$\frac{s'_2}{c_p} = \underbrace{(1-\gamma^{-1})(T_{12}-1)\frac{p'_1}{\bar{p}_1}}_{=O(M)} + \underbrace{(1-T_{12})\frac{\phi'}{\bar{\phi}}}_{=O(1)} \qquad (74)$$

At low Mach numbers, the first term on the right hand side can be neglected; this leaves only the second term, which can be rewritten as (see Strobio Chen et al.[61])

$$s'_2 = \left(1 - \frac{\bar{T}_1}{\bar{T}_2}\right)\frac{\phi'}{\bar{\phi}} \qquad (75)$$

This shows that (to leading order) entropy waves can only be generated by inhomogeneities in the mixture concentration crossing a temperature jump, but not by acoustic fluctuations.

This finding was corroborated in Strobio Chen et al.[62] by numerical simulations, based on the 2D compressible Navier–Stokes equations, of a laminar slit flame (studied experimentally by Kornilov et al.[67] in a low Mach number flow ($M \approx 10^{-3}$)). In the numerical simulations, transfer functions were calculated relating the imposed quantities u'_1, ϕ' to the response quantities Q' (total heat release rate; units W) and s'_2 in the frequency domain

$$\frac{\hat{Q}(\omega)}{\bar{Q}} = F_u(\omega)\frac{\hat{u}_1(\omega)}{\bar{u}} + F_\phi(\omega)\frac{\hat{\phi}(\omega)}{\bar{\phi}} \qquad (76)$$

$$\frac{\hat{s}_2(\omega)}{c_p} = E_u(\omega)\frac{\hat{u}_1(\omega)}{\bar{u}} + E_\phi(\omega)\frac{\hat{\phi}(\omega)}{\bar{\phi}} \qquad (77)$$

Results for the transfer functions F_u, F_ϕ, E_u, E_ϕ (gain and phase) were obtained for the frequency range $(0,\ldots 1000\,\text{Hz})$. The transfer functions all showed qualitatively similar behaviour (their gain described low-pass filter behaviour; their phase was more or less linearly dependent on frequency). However, there was a major quantitative difference: F_u, F_ϕ and E_ϕ had a magnitude of order 1, whereas E_u had a magnitude of order 10^{-3} (also the order of the Mach number) lower than 1. This is in line with the analytical result mentioned earlier: at low Mach numbers, entropy waves can only be generated by fluctuations in the composition of the premix. This result is important for 'technically premixed' flames, which are characterised by such fluctuations.

A summary of all the findings is given graphically in Figure 36. Acoustic fluctuations upstream of the flame induce kinematic fluctuations (volume consumption and flame position), which in turn induce fluctuations in the heat release rate. Fluctuations in mixture composition play a more profound role: like acoustic fluctuations, they induce kinematic fluctuations, which in
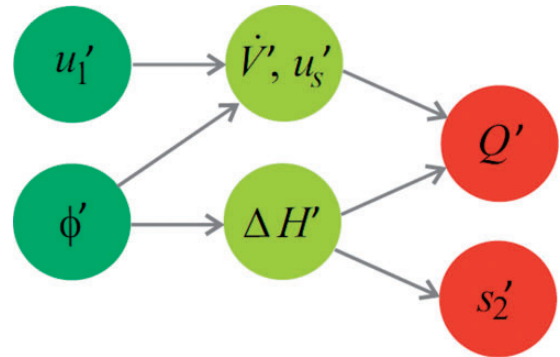

Figure 36. Causal links between upstream perturbations (u'_1, ϕ'), flame front kinematics (u'_s, $\dot{V}'$), thermochemical properties ($\Delta H'$), and source terms for acoustic and entropy waves (Q', s'_2; after Figure 5.1 in Strobio Chen[63]).

turn, induce fluctuations in the heat release rate. In addition, they modulate the heat of reaction, and this has two consequences: it contributes to the fluctuations in heat release rate, and it generates entropy waves. This is the only mechanism that generates entropy waves in low Mach number flow. This is a new finding, which is not predicted by studies assuming a stationary flame front.

9. Prediction of thermoacoustic instabilities with efficient numerical codes

Several numerical methodologies with varying degrees of resolution and corresponding computational effort are available in the literature for the prediction of thermoacoustic instabilities.

At the top of the range is direct numerical simulation (DNS), which is a first-principles approach that fully resolves the finest spatial and temporal details of turbulent combustion. It is increasingly used as a tool to gain physical insight into detailed aspects of turbulent combustion. However, the computational resources required by DNS are very high, and they exceed the capacity of most computers.

A less powerful, but computationally affordable methodology is the finite element method developed by Nicoud and Wieczorek.[68,69] Their approach is based on the Euler equations for compressible flow, together with the perfect gas equation, which are linearised and transformed into the frequency domain. The problem is closed mathematically by a model for the local heat release rate in terms of local field quantities (typically the velocity perturbation). The resulting equations are then reformulated as an eigenvalue problem

$$\mathbf{A}\mathbf{v} = -i\omega\mathbf{v} \qquad (78)$$

where ω is the complex eigenfrequency (times a factor of 2π), and $\mathbf{v}$ is the corresponding eigenvector. It has the following components

$$\mathbf{v} = [\hat{\rho},\ \hat{u}_i,\ \hat{s}]^\mathrm{T} \qquad (79)$$

where $\hat{\rho}$ is density, $\hat{u}_i$ ($i = 1, 2, 3$) are the three components of the velocity vector, and $\hat{s}$ is entropy; the hats (^) denote frequency-domain quantities. The elements of the matrix $\mathbf{A}$ are operators, they are given explicitly in Nicoud and Wieczorek.[68]

The Euler equations are a special case of the Navier–Stokes equations in that they are valid only for the case of inviscid flow. It is therefore impossible to simulate effects involving vortices with this approach.

This shortcoming is being addressed by the work currently in progress at KTH. Na et al.[70–72] repeated the procedure in Nicoud and Wieczorek[68] with the linearised Navier–Stokes equations (for adiabatic flow) instead of the Euler equations. An eigenvalue problem of the same form as (78) was obtained, where $\mathbf{v}$ is as in (79). The matrix $\mathbf{A}$ now has elements that include a dependence on the dynamic viscosity μ.

The eigenvalue problem was solved by Na et al.[70,72] with the finite element package COMSOL Multiphysics, following the approach taken in Gikadi:[73] the discretisation was performed with Lagrangian shape functions of order 2, and the iterative eigenvalue solver Arnoldi (available in the ARPACK library) was used to determine the eigenvalues ω. The method was validated by applying it to the well-known case of the Rijke tube.

The methodology will provide a new numerical tool for the study of thermoacoustic instabilities. Although it is numerically inexpensive, it is very versatile: it allows one to simulate not only the feedback between the heat source and acoustic waves, but to include also vorticity waves and entropy waves. These waves may have a stabilising or destabilising influence on a combustion system, and it is therefore important to include them in simulations that aim to make stability predictions.

The methodology developed in Na et al.[70–72] is well-suited to the study of the three-way interaction between flames, sound and vortices. Results and physical insight gained from it are expected to be published before long.

10. The role of heat exchangers in thermoacoustic instabilities

Thermoacoustic instabilities can occur not only in industrial settings, but also in domestic appliances, in particular in a boiler. When this happens, there is an enhanced emission of noise, as well as increased pollution by combustion products, and the life-time of the appliance is reduced. It is therefore important to explore passive control strategies and to implement them in new boiler designs so that these are stable for all operating conditions.

A domestic boiler typically has a combustion chamber, which houses not only the flame, but also the tubes of a heat exchanger (HEX). Figure 37(a) shows a schematic illustration.

The premixed gas enters the combustion chamber from the inside of a cylinder (similar to a drinks can in size and shape) with a dense array of small perforations (the 'burner') all over its curved wall. It then passes through the perforations and is burnt in an array of small flames on the outside of the cylinder wall, each perforation anchoring a small flame (see Figure 37(b)). The burnt gas flows radially outwards and passes through the gaps between the
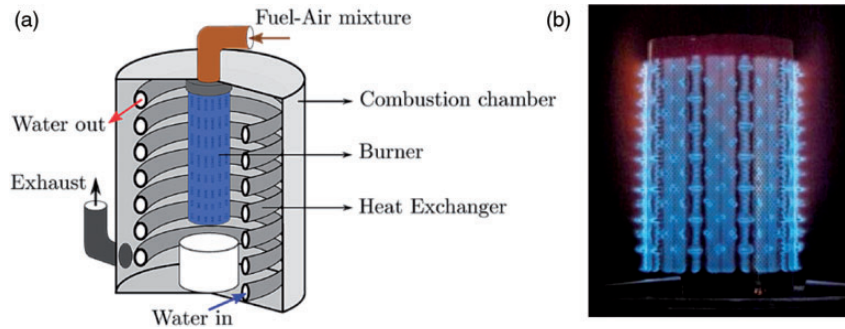
Figure 37. (a) Schematic of a domestic boiler with heat exchanger [Surendran[74]] and (b) Photograph of the burner with flames [Teerling[75]].
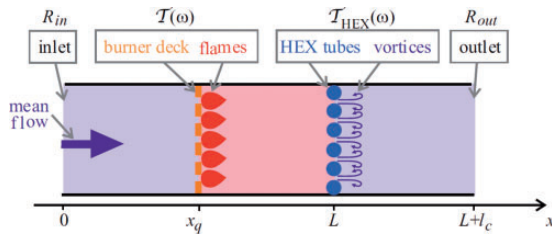

Figure 38. Schematic of idealised quasi-1D configuration for modelling purposes.

HEX tubes. It then approaches the outer casing of the combustion chamber and escapes through an exhaust pipe.

For modelling purposes, it is convenient to replace the cylindrical geometry by the quasi-1D geometry shown in Figure 38.

The end at $x = 0$ represents the line of symmetry and acts as an inlet for the premix. The burner, which comprises the burner deck (perforated plate) and an array of flames, is situated at $x = x_q$. The HEX tube row is at $x = L$. The outlet at $x = L + l_c$ represents the outer casing of the combustion chamber.

Despite the simplifications, the configuration shown in Figure 38 is a multi-component configuration. Several physical processes are expected to occur at the individual components (such as vortex shedding downstream of the HEX tubes); also interactions between them are likely.

This section will describe the modelling activities of TANGO performed with the aim to predict the stability behaviour of the multi-component configuration, and ultimately to find boiler designs which are guaranteed to be stable. Section 10.1 presents three pilot studies to explore three promising instability control strategies; these are based on literature models, which were used provisionally to describe certain components. The next two sections describe the development of dedicated models: section 10.2 presents models for the HEX,

and section 10.3 deals with the interaction between HEX and burner. Stability predictions for the complete system are given in section 10.4.

10.1. Pilot studies to explore the potential of the HEX for instability control

The presence of the HEX tube row offers several possibilities of passive control.

1. Acoustic waves are reflected and transmitted by the HEX, and hence the acoustic field in the combustion chamber is disrupted. If the disruption is such that acoustic waves are trapped in the cavity between the HEX and the outer casing of the combustion chamber, they are not available for the thermoacoustic feedback with the flame. As a consequence, the instability is weakened, it might even be completely suppressed. This possibility is explored in section 10.1.1.
2. The heat transfer from the hot gases to the HEX tubes is generally not steady, but has a *fluctuating* component. The HEX is then acoustically active. Whether it acts as an acoustic source or as an acoustic sink is determined by the Rayleigh criterion: If the heat transfer rate oscillations $Q'_{HEX}(t)$ are (to some degree) in phase with the acoustic pressure $p'_{HEX}(t)$ at the HEX, then the HEX behaves like an acoustic source, adding energy to the acoustic field. If $Q'_{HEX}(t)$ and $p'_{HEX}(t)$ are (to some degree) in antiphase, the HEX acts as an acoustic sink; it then absorbs acoustic energy and so has a stabilising effect. The potential of this control strategy is explored in section 10.1.2.
3. The HEX tubes are not completely rigid, but have walls that can perform structural vibrations and experience structural damping. Also, they interact with the surrounding fluids (liquid inside, gas outside the tubes). They form a complex fluid-loaded structure, which has resonances

at certain frequencies. Therefore, the tubes could in principle rob energy from the acoustic waves in the combustion chamber and weaken a thermo-acoustic instability. The feasibility of this mechanism for instability control is investigated in section 10.1.3.

10.1.1. HEXs with bias flow and cavity backing. The configuration of a tube row, which has a mean flow through the gaps and is situated near a rigid surface (see Figure 38) is closely related to the configuration studied by Dowling and Hughes:[76] a plate perforated with an array of parallel slits has a bias flow through the slits and is placed in front of a rigid plate. They found[76] that acoustic energy is absorbed by mechanisms linked to the bias flow (vortex shedding, modelled by a pair of vortex sheets) and that the absorption can be greatly enhanced when the slit plate is placed in front of a rigid plate so that a cavity forms between the two plates. It is possible to absorb *all* of the acoustic energy of a given frequency if the cavity is at resonance at that frequency. This can be achieved by suitable choice of the cavity depth; also, the velocity of the mean flow through the slits needs to be chosen appropriately.

Given that a cavity-backed slit plate can act as a very effective form of passive noise control, it is conceivable
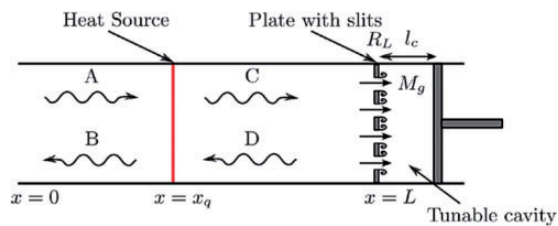
that it might also provide passive instability control. This possibility was explored by Surendran and Heckl.[77,78] They developed a theoretical model (effectively a network model) for the idealised combustion system shown in Figure 39.

The combustion system is effectively a quarter-wave resonator with a compact heat source at $x = x_q$. The heat release rate is described by an $n\tau$-law. One-dimensional acoustic waves propagate on either side of the heat source, which acts like an acoustic monopole and induces a velocity jump across the flame; this is expressed in terms of the heat release rate. The acoustic pressure is continuous.

The cavity-backed slit plate is modelled by the reflection coefficient R_L, which is the ratio between the pressure amplitude of the reflected wave at $x = L$ to that of the incident wave. An analytical expression for R_L was derived in Dowling and Hughes[76] in terms of the following parameters: width of slits, spacing of slits, cavity depth and Mach number.

Surendran and Heckl[77,78] determined the stability behaviour of the complete system by calculating its complex eigenfrequencies. The parameters in the $n\tau$-law were chosen such that mode 1 was unstable for all heat source positions between $x = 0$ and $x = L$ if the cavity-backed slit plate was absent. Stability maps were produced for this mode in the $l_c - x_q$ parameter plane. Examples are shown in Figure 40, for the three bias-flow Mach numbers $M_g = 0.001$, 0.005, and 0.01. The mean temperature throughout the combustor was uniform (288 K). The slits of the slit plate were 0.002 m wide and spaced 0.02 m apart (centre-to-centre).

The figure clearly shows the stabilising effect of the mean flow and the cavity. These results are encouraging, but more detailed studies are needed. In particular, the tubes have a smooth, rather than a sharp-edged, cross-section; therefore the model in Dowling and Hughes[76] (which relies on the Kutta condition to describe the flow field) may not be appropriate for HEX modelling purposes. Also, the mean temperature

Figure 39. The modelled combustion system comprising open end, compact heat source, slit plate, cavity and closed end (from Figure 1 in Surendran and Heckl[77]).
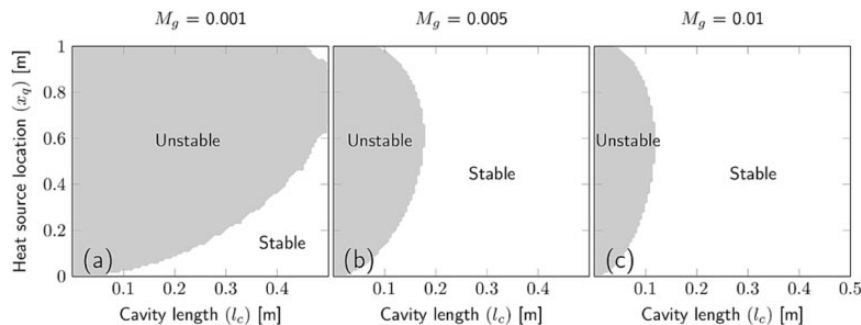
Figure 40. Stability maps in the $l_c - x_q$ plane for a combustion system with three different Mach numbers (from Figure 8 in Surendran and Heckl[78]).

is not uniform in the actual case: the flow is cold upstream of the heat source, hot in the region between the heat source and the HEX, and again cold downstream of the HEX. As a consequence, the speed of sound may vary considerably throughout the combustion chamber, cause significant changes to the acoustic field, and affect the stability behaviour.

10.1.2. The HEX as active acoustic element. The burner acts as a heat *source*, transferring heat energy at a rate Q_f to the flow that passes it. The HEX tube row acts as a heat *sink*, absorbing heat energy at a rate Q_{HEX} from the flow that passes it. Due to the fluctuating nature of their heat transfer rates, both elements are acoustically active. A fundamental study of a combustion system with two acoustically active elements was performed by Hosseini et al.[79,80] who considered the basic configuration shown in Figure 41 (essentially a Rijke tube supplemented by a heat sink).

The heat release rate fluctuations of both elements were described by $n\tau$-laws. The heat source had coupling coefficients n_1 and time-lag τ_1; the equivalent parameters for the heat sink were n_2 and τ_2. The mean temperature was assumed to be uniform in each of the three regions shown in Figure 41. It jumped from $\bar{T}_1$ (cold) to $\bar{T}_2$ (hot) across the heat source, and from $\bar{T}_2$ back down to $\bar{T}_1$ across the heat sink.

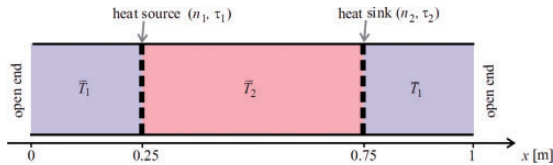The complex eigenfrequencies were calculated with the numerical Helmholtz solver of COMSOL

Multiphysics, and the stability behaviour was ascertained from the imaginary part. The key parameters that were found to affect the stability behaviour are the time-lags τ_1 and τ_2, the jump in mean temperature $\bar{T}_2 - \bar{T}_1$, and the compactness of the HEX. No simple trends could be established: the heat sink can enhance as well as suppress instabilities.

In conclusion, this study showed that a HEX is a potential tool for instability control. However, a comprehensive theoretical model is necessary to establish the correct parameter space. This information can then be used by designers to develop a stable combustion chamber that includes both heating and cooling elements.

10.1.3. HEX tubes with structural resonances. HEX tubes are flexible fluid-loaded structures, which are subject to resonance at several frequencies and also to damping. It is conceivable that a thermoacoustic instability is influenced significantly if its frequency is similar to one of the resonance frequencies of the HEX tubes. This mechanism was exploited in a short study by Surendran and Heckl.[81,82]

The individual tubes of the tube row were modelled as cylindrical shells (diameter d, wall thickness h) filled with liquid and surrounded by gas. Their motion in the radial, axial and azimuthal direction is known in terms of a set of 4th-order PDEs (see section 7.12 of Junger and Feit [83]). The row of tubes (spacing η) was modelled analytically as a diffraction grating, following the work by Huang and Heckl.[84] The reflection and transmission coefficients were calculated as a function of frequency for a HEX geometry with $d = 0.017\,\mathrm{m}$, $h = 0.001\,\mathrm{m}$, $\eta = 0.0225\,\mathrm{m}$. The liquid inside was water and the surrounding gas was air. The results are shown in Figure 42.

The vertical dashed line marks the critical frequency where the acoustic wavelength becomes equal to the tube spacing and the reflected and transmitted waves cease to be 1D.
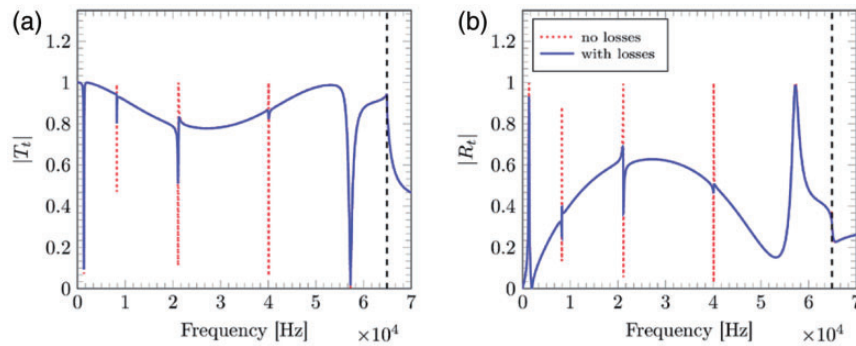

Figure 41. Rijke tube with acoustically active heat source and heat sink (after Figure 1 in Hosseini et al.[79]).

Figure 42. Reflection and transmission coefficient of a tube row with $d = 0.017\,\mathrm{m}$, $h = 0.001\,\mathrm{m}$, $\eta = 0.0225\,\mathrm{m}$ (from Figure 2.8 in Surendran[82]).

The sharp peaks in this figure are due to the resonances of the radial tube modes. Results are shown for two values of structural damping: $\sigma_s = 0$ (dashed red curve) and $\sigma_s = 0.005$ (solid blue curve). The structural losses have very little influence on the width of the peaks. This indicates that exploitation of the HEX tube resonances is not a promising strategy for instability control. It also indicates that the HEX tubes can be regarded as rigid.

Moreover, the resonance frequencies of the tubes must be in the low-frequency range, where thermoacoustic instabilities tend to occur, if the tube resonances are to be exploited for instability control. This is difficult to achieve for the small tube diameters ($d = 2 \ldots 5 \, \text{mm}$) that are typical for HEX tubes in domestic boilers.

10.2. Modelling the HEX as a thermoacoustic network element

From an acoustic point of view, the HEX plays two roles:

1. it scatters acoustic waves that impinge on it
2. it acts as an acoustic source (or sink), which radiates (or absorbs) acoustic waves due to the fluctuations in its heat transfer rate.

The scattering aspects are considered in section 10.2.1, and the heat transfer aspects in section 10.2.2. In section 10.2.3, the two aspects are considered together, and a combined model is presented.

10.2.1. Acoustic scattering at the HEX. The HEX models used in our pilot studies were over-simplified. The model in Dowling and Hughes,[76] used in section 10.1.1 for a slit plate with bias flow, relies on the Kutta condition, i.e. it assumes that the scatterers have sharp edges. The model in Huang and Heckl,[84] used in section 10.1.3 for the scattering by a tube row, does not include the bias flow. It was therefore necessary to develop a new model to take into account the smooth geometry of the HEX tubes, together with the flow through the gaps between the tubes. This was done by Surendran et al.,[85,86] who regarded the HEX tubes as rigid cylinders with bias flow. Their study had a theoretical and experimental component.

In the theoretical part, they considered two half-cylinders in a hard-walled duct as shown in Figure 43. This is equivalent to an infinitely extended row of cylinders, as suggested by the concept of image sources.

The configuration shown in Figure 43 was modelled by a quasi-steady approach, first proposed by Ronneberger.[87] The key assumption in quasi-steady modelling is

$$St = \frac{f}{u_g/r} \ll 1 \qquad (80)$$

where St is the Strouhal number, f is the frequency of the acoustic wave, u_g is the velocity in the gap between the cylinders, and r is the radius of the cylinders. Equation (80) means that in a short time interval, acoustic waves can be regarded as 'frozen', while aerodynamic effects evolve.

In Surendran et al.,[85,86] the duct (of height h_p) is divided into three regions (①, ⓙ and ②) as shown in Figure 43. The notation is p for pressure, u for velocity and ρ for density; the subscripts 1, j and 2 denote the region. Regions ① and ② contain 1D flow. The 2D flow is confined to region ⓙ (shaded region in Figure 43), where the following processes take place. The flow passes through the gap (of height h_g) between the cylinders, and it separates from the cylinder surfaces to form a jet with cross-sectional height h_j. Further downstream (beyond the plane marked by a dashed line in Figure 43), the jet disintegrates into a turbulent mixing region, where its kinetic energy is dissipated, while some pressure recovery occurs.

In addition to (80), the following assumptions were made:

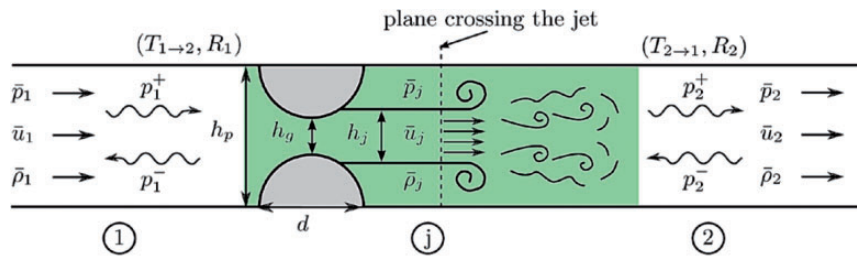– The acoustic wavelength is large enough so that the 2D flow region can be regarded as compact,

Figure 43. Schematic of two half-cylinders in a flow duct (from Figure 4 in Surendran et al.[86]).

i.e. the acoustic field quantities do not change phase across region ①.

- The Mach number is small enough so that the flow through the gap remains subsonic.
- The flow from region ① into the jet is isentropic and irrotational, but the flow beyond the jet is not.
- Viscous flow effects, other than the flow separation at the cylinder surfaces, are negligible.
- Heat transfer, viscous losses and frictional losses at the duct wall are negligible.

The following conservation equations (compressible flow) were then applied to three hypothetical control volumes.

- Control volume between the ①–① interface and the plane perpendicular to the jet (dashed line in Figure 43)

$$h_p \rho_1 u_1 = h_j \rho_j u_j \text{ (mass conservation)} \tag{81a}$$

$$\frac{1}{2} u_1^2 + \frac{\gamma}{\gamma - 1} \frac{p_1}{\rho_1} = \frac{1}{2} u_j^2 + \frac{\gamma}{\gamma - 1} \frac{p_j}{\rho_j} \text{ (energy conservation)} \tag{81b}$$

$$\frac{p_1}{p_j} = \left(\frac{\rho_1}{\rho_j} \right)^{\gamma} \text{ (isentropic gas relation)} \tag{81c}$$

- Control volume between the plane crossing the jet and the ①–② interface

$$h_j \rho_j u_j = h_p \rho_2 u_2 \text{ (mass conservation)} \tag{82a}$$

$$h_p p_j + h_j \rho_j u_j^2 = h_p p_2 + h_p \rho_2 u_2^2 \text{ (momentum conservation)} \tag{82b}$$

- Control volume enclosing region ①

$$\frac{1}{2} u_1^2 + \frac{\gamma}{\gamma - 1} \frac{p_1}{\rho_1} = \frac{1}{2} u_j^2 + \frac{\gamma}{\gamma - 1} \frac{p_j}{\rho_j} \text{ (energy conservation)} \tag{83}$$

The flow separation location is required to determine the height of the jet. This is found by solving the von Kármán equations with the Thwaites method (see Appendix A in Surendran et al.[86]). The jet height depends on the following parameters: diameter and spacing of the cylinders, upstream Mach number, and on the viscosity and density of the fluid.

The set of equations (81) to (83) was linearised with respect to the acoustic field quantities, and these were decomposed into forward and backward travelling waves, with pressure p_1^+, p_1^- on the upstream side, and p_2^+, p_2^- on the downstream side of region ①. They were then written in terms of the total enthalpy $(1 \pm M) p^{\pm}/\bar{\rho}$, which is the natural choice of acoustic variable when a mean flow is present. The final result is

$$\begin{bmatrix} (1 + M_2) p_2^+ \\ (1 - M_1) p_1^- \end{bmatrix} = \begin{bmatrix} T_{1\to2} & R_2 \\ R_1 & T_{2\to1} \end{bmatrix} \begin{bmatrix} (1 + M_1) p_1^+ \\ (1 - M_2) p_2^- \end{bmatrix} \tag{84}$$

(for details of the derivation see Surendran[88]). M_1, M_2 are the Mach numbers corresponding to the mean velocities $\bar{u}_1$, $\bar{u}_2$. The matrix elements T and R denote, respectively, the transmission and reflection coefficients of region ①. For waves incident from the upstream side, the coefficients are denoted by $T_{1\to2}$ and R_1; for waves incident from the downstream side, the notation is $T_{2\to1}$ and R_2.

The coefficients depend on the same parameters as the jet height. Their Mach number dependence is shown by the solid curves in Figure 44 for the case $d = 16$ mm, $h_p = 20$ mm. It can be seen that with increasing Mach number, the transmission coefficients decrease, while the reflection coefficients increase.

The following two questions were addressed in an experimental validation exercise:

1. Up to what Strouhal number is the quasi-steady model valid?
2. Is the model, which has been derived for two half-cylinders in a duct, valid for a row of *several* cylinders in a duct?

The experiments were performed in the flow-duct rig of the Marcus Wallenberg Laboratory at KTH, which has a cross-sectional area of 120 mm × 25 mm. The mean flow velocity was varied in the range $\bar{u}_1 = 0, \ldots 15.5$ m/s. A multi-microphone technique was used to measure the transmission and reflection coefficients at three frequencies ($f = 150, 250, 350$ Hz). Further experimental details are given in Surendran et al.[86]

In order to answer question (1), the dependence of the coefficients on the Strouhal number was measured. As expected, there was good agreement between the theoretical and experimental results at low Strouhal numbers, but the agreement started to break down if $St > 0.16$. Nevertheless, this is consistent with our initial modelling assumption $St \ll 1$.

In order to answer question (2), a row of six cylinders was inserted into the duct. With a diameter of 16 mm and a centre-to-centre distance of 20 mm, they were equivalent to the modelled configuration.
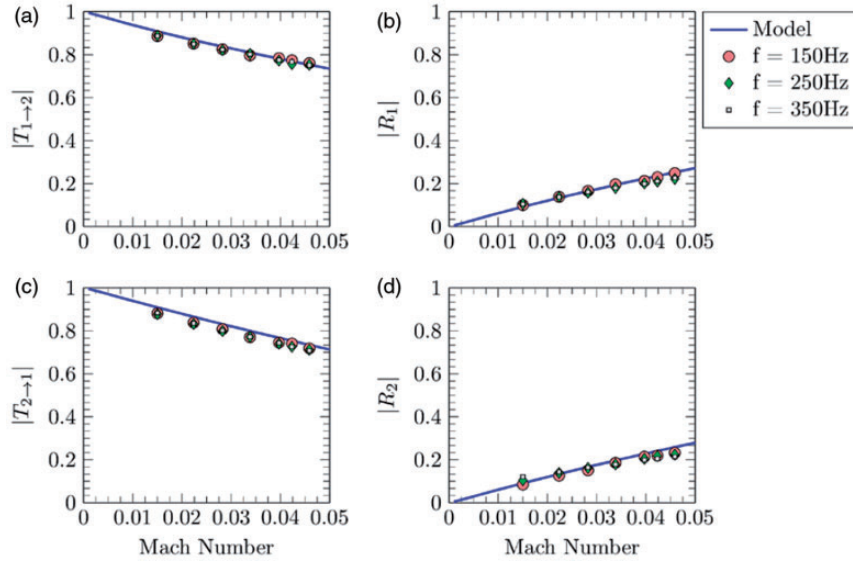
Figure 44. Magnitude of transmission and reflection coefficients as a function of upstream Mach number. Solid curve: predicted results for $d = 16$ mm, $h_p = 20$ mm. Markers: measured results for an equivalent cylinder row (from Figure 11 in Surendran et al.[86]).

The measured transmission and reflection coefficients are shown by the markers in Figure 44. All three frequencies give similar results, and these agree very well with the predicted results. The use of the quasi-steady model for a row of several cylinders is therefore fully justified.

10.2.2. Fluctuating heat transfer rate at the HEX. The heat release rate of a flame is commonly described by a FTF, which is the ratio (in the frequency domain) of the global heat release rate and the acoustic velocity at a reference position upstream of the flame (see e.g. equation (9)). The same concept can be applied to describe the heat transfer rate from a HEX

$$\mathcal{T}_{HEX}(\omega) = \frac{\hat{Q}_{HEX}(\omega)/\bar{Q}}{\hat{u}_{ref}(\omega)/\bar{u}} \tag{85}$$

This transfer function was determined in two independent studies by Surendran et al.[89,90] and Strobio Chen et al.[91] Both used a CFD solver to calculate heat transfer rate (integrated over the surface of the HEX) in response to an imposed velocity perturbation. This was Fourier-transformed into the frequency domain, and the HEX transfer function was then calculated from (85).

Surendran et al.[89,90] considered HEX tubes of circular cross-section (see Figure 45(a)) and used incompressible CFD. Strobio Chen et al.[91] considered HEX tubes with rectangular cross-section (see Figure 45(b)) and used compressible CFD.

The predicted HEX transfer functions (gain only) are shown in Figure 46 as a function of frequency. Figure 46(a) gives Surendran's results for three different

mean velocities ($\bar{u}_1 = 0.5$, 1.0, 1.5 m/s) and corresponding mean temperatures ($\bar{T}_1 = 415$, 610, 750 K upstream of the HEX). Figure 46(b) gives Strobio Chen's results for the mean velocity $\bar{u}_1 = 0.89$ m/s and mean temperature $\bar{T}_1 = 1200$ K. The frequency axis in Figure 46(b) is labelled in terms of the Helmholtz number; the range depicted corresponds to the frequency range 0 ... 1600 Hz.

The two geometries have qualitatively similar gain curves: both decrease with increasing frequency, indicating that the HEX acts like a low-pass filter.

10.2.3. Complete model for the HEX. The two physical processes studied individually in the previous two sub-sections, take place together at the HEX. It is therefore necessary to have a combined model. Such a model was developed analytically by Surendran et al.[88,90] and numerically by Strobio Chen et al.[92]

Surendran et al.[88,90] adopted a network approach, where each of the two processes was represented by a network element: the acoustic scattering was described by the coefficients R_1, R_2, $T_{1\rightarrow2}$, $T_{2\rightarrow1}$ of the scattering matrix given in (84); the fluctuating heat transfer rate was described by the HEX transfer function given by (85).

At first, the two network elements were assumed to be separated by a distance Δx, with 1D acoustic waves propagating between them (see Figure 47). The total scattering matrix was defined by the reflection and transmission coefficients of the two elements combined

$$\begin{bmatrix} p_d^+ \\ p_u^- \end{bmatrix} = \begin{bmatrix} T_{u\rightarrow d} & R_d \\ R_u & T_{d\rightarrow u} \end{bmatrix} \begin{bmatrix} p_u^+ \\ p_d^- \end{bmatrix} \tag{86}$$
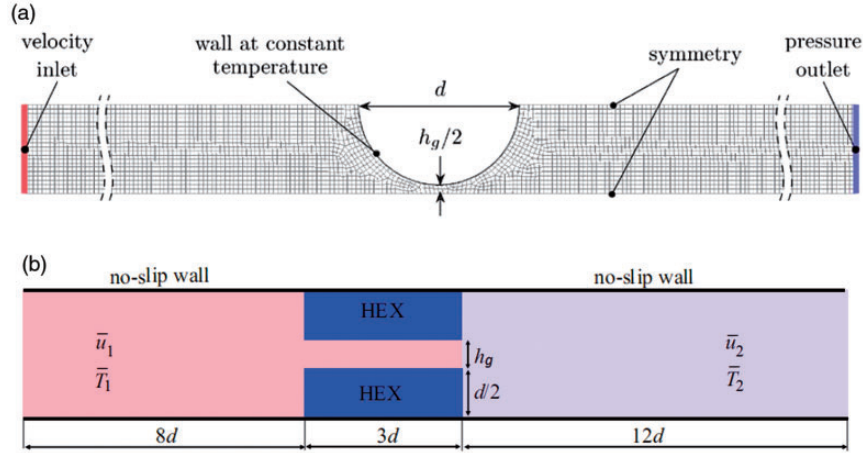
Figure 45. Geometry of the HEX used for CDF simulations. (a) Circular HEX tube. (from Figure 3 in Surendran et al.[90]) and (b) Rectangular HEX tube (after Figure 2 in Strobio Chen et al.[91]).
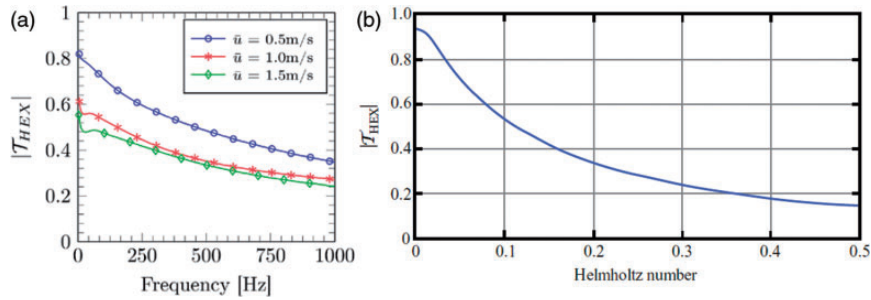

Figure 46. Numerical results for the gain of the HEX transfer function. (a) Results for the circular geometry in Figure 45(a) with $d = 3$ mm and $h_g = 0.3$ mm (from Figure 4(a) in Surendran et al.[90]) and (b) Results for the rectangular geometry in Figure 45(b) with $d = 12.8$ mm and $h_g = 0.8$ mm (after Figure 3(a) in Strobio Chen et al.[91]).

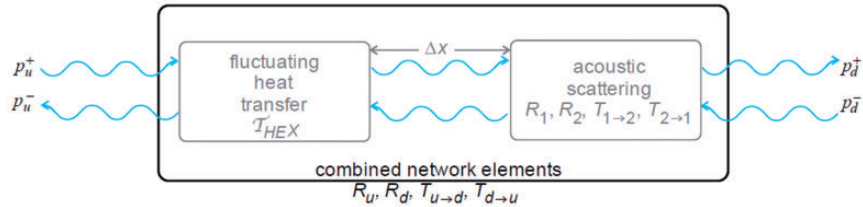
Figure 47. Network comprising three elements: heat sink with fluctuating heat transfer rate, duct of length Δx, tube row reflecting and transmitting acoustic waves (based on Figure 6 in Surendran et al.[90]).

p_u^-, p_d^+ denote the outgoing waves, p_u^+, p_d^- denote the incoming waves (see Figure 47).

The matrix components were calculated analytically, and then the limit $\Delta x \to 0$ was taken. They depend on the following parameters: mean flow velocity, diameter and spacing of the cylindrical scatterers, temperature jump across the HEX, and viscosity and density of the cold gas. All four matrix components were found to have a weak dependence on the frequency.

The dependence on the mean velocity was mixed: as the mean velocity was increased in the range $\bar{u} = 0.5 \ldots 1.5$ m/s, the transmission coefficients took values in the ranges $|T_{u \to d}| = 0.9 \ldots 1.3$ and $|T_{d \to u}| = 1.1 \ldots 0.7$, and the reflection coefficients took values $|R_u| = 0 \ldots 0.3$ and $|R_d| = 0 \ldots 0.3$.

These results are in line with those of Strobio Chen et al.[92] They used compressible CFD, i.e. they modelled the two processes of heat transfer fluctuations and
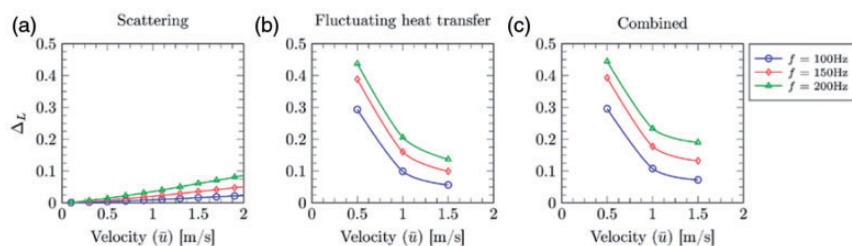
Figure 48. Absorption coefficient Δ_L of a cavity-backed row of HEX tubes for three different HEX models: (a) acoustic scattering only. (b) fluctuating heat transfer only and (c) acoustic scattering and fluctuating heat transfer combined (from Figure 10 in Surendran et al.[93]).

acoustic scattering as occurring together. Their simulations for the same geometry predicted transmission coefficients close to 1 and reflection coefficients close to 0. These findings seem to suggest that a HEX tube row is nearly transparent for acoustic waves, and hence ineffective as an absorber of acoustic waves.

However, when backed by a cavity, the situation changes considerably. This is illustrated in Figure 48, which shows the absorption coefficient Δ_L (defined by $\Delta_L = 1 - |R_L|^2$, where R_L is the reflection coefficient of the HEX tube row *with* cavity backing) as a function of mean velocity at the frequencies $f = 100, 150, 200$ Hz. The geometry is described by the parameters $d = 3$ mm, $\eta = 3.3$ mm and $l_c = 0.25$ m (cavity length). Three different cases are shown to illustrate the roles played by the HEX: acoustic scattering only (Figure 48(a)), fluctuating heat transfer only (Figure 48(b)), acoustic scattering and fluctuating heat transfer combined (Figure 48(c)).

The influence of the fluctuating heat transfer dominates, and the added influence of the acoustic scattering becomes significant only for large velocities. It is evident from Figure 48(c) that the absorption coefficient can reach values close to 0.5. So while the HEX on its own seems to be a poor sound absorber, it becomes very efficient when backed by a cavity. This finding bodes well for the strategy of exploiting the HEX for instability control.

10.3. Modelling of the interaction between burner and HEX

For practical reasons it is desirable to make boilers as compact as possible. This can be achieved by reducing the distance between the burner and the HEX. An added benefit of this measure would be the reduction of NO_x emissions.

However, as the HEX is brought closer to the burner, the two components become more prone to interaction. The key interaction mechanisms are
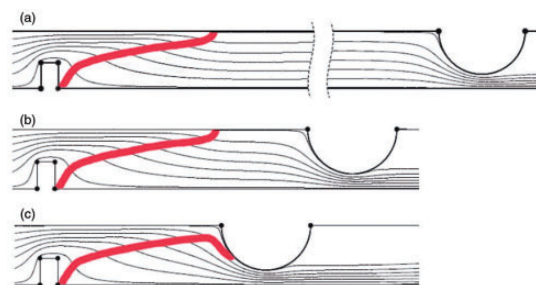
1. distortion of the flow profile, and

Figure 49. Flow streamlines (thin black curves) and flame shapes (thick red curves) for three successively decreasing burner-HEX distances. (a) Flow distorted by the burner/flame regains its 1D profile upstream of the HEX; flame does not impinge. (b) Flow upstream of the HEX does not regain its 1D profile; flame does not impinge and (c) Flow upstream of the HEX does not regain its 1D profile; flame impinges on the HEX (after Figure 2 in Hosseini et al.[94]).

2. flame impingement.

The level of interaction is governed by the distance between the burner and the HEX, as illustrated in Figure 49.

The studies were largely numerical and aimed to simulate the laboratory configuration shown in Figure 50, which is representative of many heating appliances. The design is effectively 2D. The burner deck is represented by a slit plate. A methane–air premix passes through the slits from below. Anchored on the slit plate is a row of parallel Bunsen-type wedge-shaped flames. These are shown in cross-section in Figure 50(b). The combustion products flow upwards past the HEX tubes, where they transfer heat energy to the tubes and cool down in the process. The cooled gases flow further upwards and leave the domain of interest.

Detailed studies of the two interaction mechanisms are reported in the next two subsections: 10.3.1 covers hydrodynamic interaction, and 10.3.2 is about flame impingement.

10.3.1. Hydrodynamic interaction. Numerical simulations were conducted by Hosseini et al.[94–96] to elucidate whether the burner and the HEX can be decoupled and modelled by independent transfer functions. Their numerical domain is shown in Figure 51.

Symmetry was used in order to reduce the numerical domain and to model the effects of the neighbouring flames and HEX tubes. The inlet boundary was set to a constant velocity of 0.8 m/s; the outlet boundary to constant pressure (atmospheric). The burner deck and HEX were modelled as isothermal boundaries with temperatures of 793 K and 343 K, respectively. These values were chosen because they match the measured values of the test rig.

A 2D mesh was generated with the software package Gambit. The grid size was 20 μm near the flame to resolve the flame thickness ($\delta \approx 500\,\mu m$), and 40 μm near the HEX tube to resolve the thermal boundary layer thickness ($\delta_t \approx 600\,\mu m$). Elsewhere, the grid size was 160 μm.

The commercial CFD code, ANSYS Fluent (release 17.0),[98] was used for the CFD simulations. The flow was assumed to be laminar and the fluid to be an incompressible perfect gas. These assumptions were justified because the Reynolds number and Mach number are both small. The methane–air pre-mixture was lean with an equivalence ratio of 0.8. The combustion was modelled using the code in Fluent for finite-rate chemistry with a two-step reaction mechanism

$$CH_4 + 1.5\,O_2 \rightarrow CO + 2\,H_2O \qquad (87a)$$

$$CO + 0.5\,O_2 \ \rightleftharpoons \ CO_2 \qquad (87b)$$
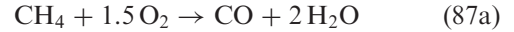
The rate constant for each reaction was calculated from the Arrhenius equation, with the pre-exponential factors chosen in such a way that the laminar flame speed predicted by 1D simulations fitted the experimental data by earlier authors. Details can be found in chapter 3.4 of Hosseini.[95] Fluent provided further input: the specific heats of the individual species were obtained from temperature-dependent polynomials; the viscosity and thermal conductivity were obtained from kinetic theory; the corresponding properties of the mixture were then available from the mixing law. The local rate of heat release was determined by multiplying the reaction rate by the enthalpy of formation, Δh_f^0.

In order to characterise the burner and the HEX in terms of their unsteady heat transfer, transient simulations were performed (by imposing a velocity jump at the inlet). The heat release rate of the flame was then calculated by integrating the local heat release rate over the volume of the flame. The heat absorption rate of the HEX was calculated by integrating the heat flux across the HEX surface.

The transfer function for the HEX (see equation (85)) is defined for a 1D velocity field. By introducing the velocity average over a cross-section at a chosen location between the flame and the HEX, Hosseini et al.[94] extended the definition to non-uniform velocity fields. They subsequently calculated the HEX transfer function, with velocity averages taken at different locations. Their flame was 5 mm long, and the distance between the flame tip and HEX surface was 45 mm. Figure 52 shows the gain and phase of their HEX transfer function for three different averaging cross-sections; these were located at 2 mm, 25 mm, 42 mm from the
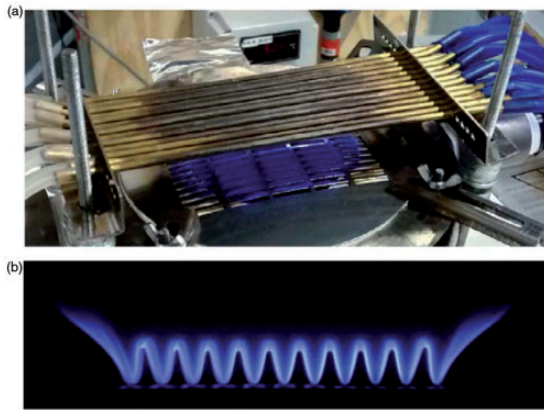

Figure 50. (a) Laboratory test rig comprising slit burner and HEX tubes and (b) Cross-section through the slit flame (from Figure 1(a) in Hosseini et al.[94]).
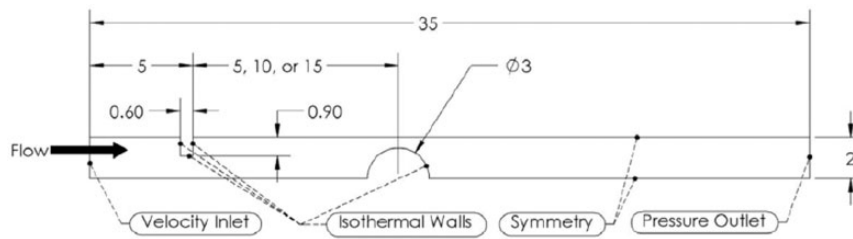

Figure 51. Numerical domain and boundary conditions; the dimensions are in millimetres (from Figure 2 in Hosseini et al.[97]).

flame tip. The flow is non-uniform at the 2 mm location, but uniform at the two more distant locations.

The curves for the different locations are almost identical, and they are all in acceptable agreement with the no-burner case.

Several other simulations with various burner-HEX distances were made, and the following conclusion was reached. For distances comparable to the flame length and large enough to avoid flame impingement, a transfer function for the HEX can be defined on the basis of
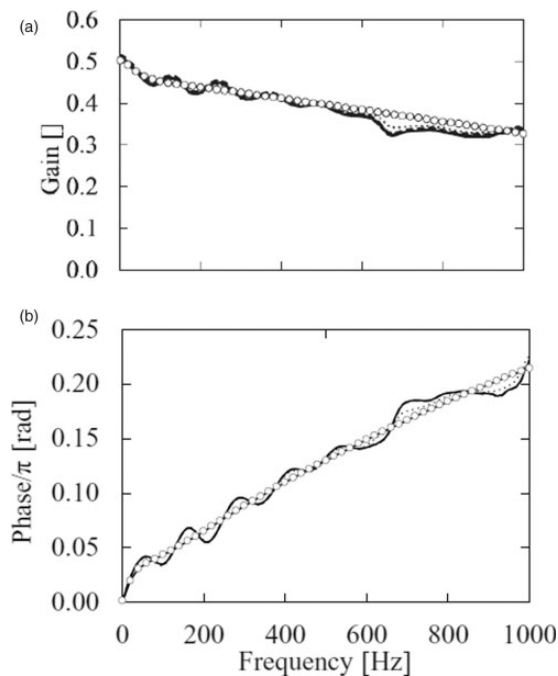

Figure 52. HEX transfer functions with average velocities taken at 2 mm ($\cdots\cdots$), 25 mm(- - - -), and 42 mm (_____) from the flame tip. The no-burner case is shown by markers ($\circ$). (a) Gain and (b) Phase (from Figure 11 in Hosseini et al.[94]).

an average velocity taken over a cross-sectional plane between the flame tip and the HEX surface. This transfer function is suitable for describing the HEX as an independent element in a network model.

In a parallel study, Strobio Chen et al.[92] applied compressible CFD to analyse the geometry shown in Figure 51. They simulated the burner-HEX configuration by two approaches:

1. by treating it as two separate elements, calculating the scattering matrix of each element with CFD, and then constructing the scattering matrix of the combined elements with a network model;
2. by treating it as a single unit and calculating its scattering matrix by CFD.

By comparing the results of these two approaches, they confirmed that the burner and the HEX can be treated as individual network elements as long as the flow field reaches a uniform velocity profile in the region between the flame tip and the HEX. This is in line with the findings by Hosseini et al.[94,97]

The calculations of the scattering matrix in Strobio Chen et al.[92] also revealed that the HEX enhances a pre-existing ITA mode (see section 10.4.1).

10.3.2. Interaction due to flame impingement. If the distance between the burner and HEX tube is decreased beyond the point considered in the previous section, two further effects set in: first the temperature profile upstream of the HEX becomes non-uniform, and then the flame impinges on the HEX surface. These two effects were studied by Hosseini et al.[94,95,97] They calculated the fields of temperature and reaction heat for increasing closeness of the HEX to the burner. Their results are shown in Figure 53 by pairs of 2D plots for the distances $Y = 10$, 8, 7 and 6 mm, where Y is the distance between the top of the burner deck and the
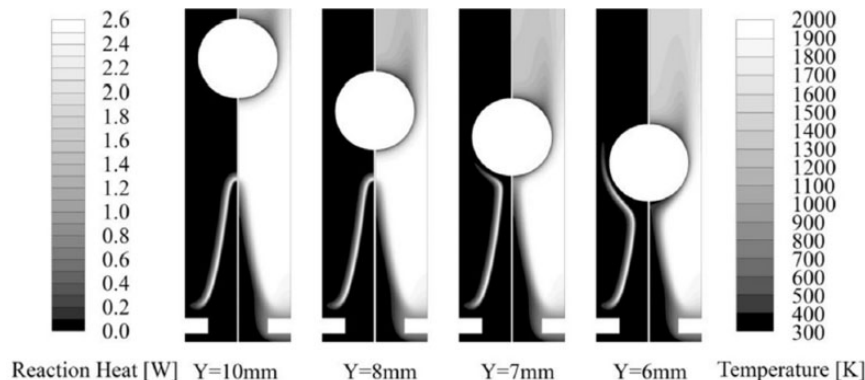

Figure 53. Thermodynamic fields for four burner-HEX distances: $Y = 10$, 8, 7 and 6 mm. Left side of each image: field of reaction heat. Right side of each image: temperature field (from Figure 12 in Hosseini et al.[94]).

centre of the HEX tube. The right sides of the plots show the temperature field and the left sides show the reaction heat.

The following observations were made from these plots. The temperature profile of the flow approaching the HEX is uniform only for the largest distance shown ($Y = 10$ mm), but not for the others. Flame quenching and impingement occur at $Y = 7$ and 6 mm. For the distance $Y = 7$ mm, the flame stretches and reaches into the distorted flow field surrounding the HEX tubes; a consequence of this increased length is an increase in the convective travelling time along the flame surface. For the distance $Y = 6$ mm, the flame stretches even further and reaches into the high-velocity region between adjacent HEX tubes; there the convection along the flame surface is faster, so the travelling time is reduced compared with the $Y = 7$ mm case.

These effects on the travelling time are reflected in the phase curve of the burner transfer function shown in Figure 54(a). The slope of this curve, which is an indicator of a time-lag, is less steep for $Y = 7$ mm than for $Y = 6$ mm. The gain of the burner transfer function for the impinging cases is generally smaller than for the non-impinging cases.

Figure 54(b) shows the gain and phase of the HEX transfer function. The extremely large gain is an artefact of defining a 1D reference velocity in a highly 2D flow field.

However, the phase curve of this transfer function is amenable to physical interpretation. For the non-impinging cases, the phase curves are around zero, whereas for the impinging cases, they are shifted upwards by about π. The phase values are exactly zero and π, respectively, at low frequencies, i.e. for the 'quasi-steady' case, where the velocity increases or decreases very slowly. A phase value of zero means that the velocity u and the heat absorption rate Q by the HEX are in phase: a slow increase in u leads to a slow increase in Q. A phase of π, however, means that u and Q are in anti-phase: an increase in u goes hand in hand with a *decrease* in Q.

The physical phenomena that correspond to these phase results can be explained by considering again the quasi-steady case: When the flow velocity increases, the flame becomes longer. This is equivalent to the HEX tube getting further into the flame and getting exposed to more cold unburnt flow (see right sides of Figure 53 for $Y = 7$ mm and $Y = 6$ mm). More exposure to unburnt flow means less heat flux. Overall, when impingement occurs, an increase in velocity leads to a decrease in the heat absorption rate, and this is reflected in the FTF by a phase value of π.

The phase of the heat absorption rate with respect to the acoustic field is of fundamental importance for the behaviour of the HEX as an active acoustic element. If Q is to some degree in phase with the acoustic pressure, the HEX acts as an acoustic source; if they are out of phase, it acts as an acoustic sink. In the first case, the HEX encourages, and in the second case it discourages a thermoacoustic instability.
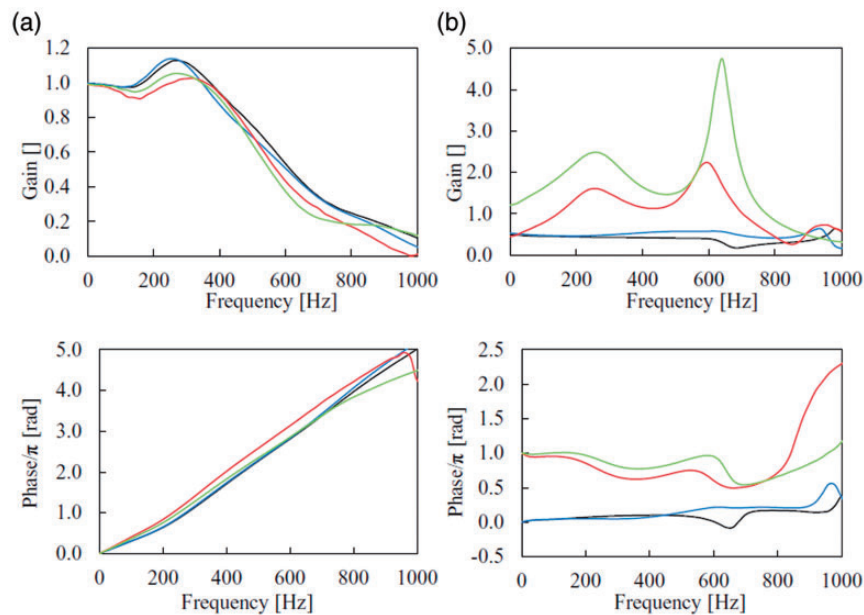

Figure 54. Gain and phase of the transfer functions for four burner-HEX distances: $Y = 10$ mm (—), $Y = 8$ mm (—), $Y = 7$ mm (—) and $Y = 6$ mm (—). (a) Transfer function of the burner and (b) Transfer function of the HEX (from Figures 13 and 14 in Hosseini et al.[94]).

10.4. Stability predictions for the complete boiler system

10.4.1. Stability predictions by Strobio Chen et al.
Strobio Chen[63] made stability predictions for a complete boiler system with the following elements. The flame was a pre-mixed methane–air flame with an equivalence ratio of 0.8. The geometry was characterised by the following parameters.

HEX tube diameter: 3 mm;
gap between adjacent HEX tubes: 1 mm;
thickness of burner deck: 0.6 mm,
width of slits in burner deck: 1.8 mm.
distance between inlet and burner deck: 0.6 mm;
distance between burner deck and centre of HEX tube: 10 mm;
distance between centre of HEX tube and outlet: 0.5015 m;

The burner and the HEX were each modelled as individual network elements (their distance was large enough so that the mean flow leaving the flame developed a uniform profile before it reached the HEX). The transfer matrices of these two elements were calculated with compressible CFD. It turned out that the flame had an intrinsic mode at 255 Hz.

The main parameters for the stability predictions were the inlet and outlet reflection coefficients, R_{in} and R_{out}. These were assumed to be purely real and were varied in the range $[-0.3 \ldots 0 \ldots + 0.3]$. An open end is described by a negative value, a closed end by a positive value, and the value zero corresponds to a completely non-reflecting end. Even for the non-zero values, the reflection was quite weak, given that the reflection coefficients did not exceed a magnitude of 0.3.

The choice of low R values was deliberate to expose any effects that the HEX might have on the stability of the intrinsic mode at 255 Hz. The stability maps are shown in Figure 55 for two cases. Part (a) of the figure shows the case of a single row of HEX tubes; part (b) shows the case where there is a second row of

HEX tubes, a distance of 10 mm downstream of the first row.

It is clear that the presence of the HEX tube rows have a de-stabilising effect. The case of a double tube row (shown in Figure 55(b)) has a larger region of instability than the case of a single tube row (shown in Figure 55(a)); this, in turn, has a larger region of instability than the no-HEX case (not shown).

The destabilising role of the HEX can be explained by the temperature jump that occurs across it. For the single tube row, the temperature jump is from 2000 K down to about 1300 K. For the double tube row, there is a second temperature jump from 1300 K to a much lower value (about 845 K).

The intrinsic mode, which is initially stable, becomes unstable if the HEX is made up of a *double* tube row.

10.4.2. Stability predictions by Surendran et al.
Surendran et al.[88,90] developed a network model for the complete system comprising the elements shown in Figure 56: open end at $x = 0$, compact flame at $x = x_q$ (described by a basic $n\tau$-law)), HEX at $x = L$ (described by the scattering matrix presented in section 10.2.3), cavity of length l_c, and rigid backing plate at $x = L + l_c$. The mean temperature jumps across the heat source from room temperature to a much higher value, and across
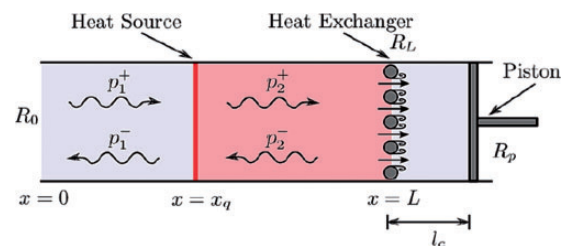

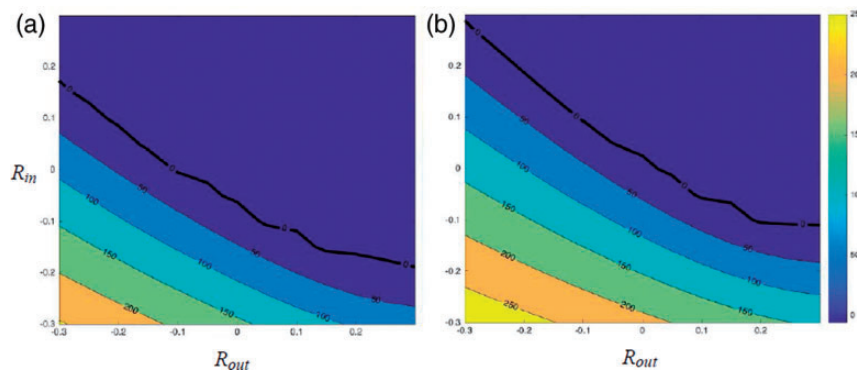**Figure 56.** Schematic of the modelled combustion system (from Figure 1 in Surendran et al.[90]).

Figure 55. Stability map obtained from network model in the $R_{out} - R_{in}$ parameter plane. (a) Single row of HEX tubes (from Figure 5.3 in Strobio Chen[63]) and (b) Double row of HEX tubes (from Figure 5.4 in Strobio Chen[63]). Positive growth rates indicate instability.

the HEX it jumps back down to a relatively low temperature.

Stability predictions were made in Surendran et al.[90,93] with a focus on the following parameters: cavity length, flame location, mean velocity of incoming flow and temperature jump. Some instructive examples are shown in Figure 57 in the form of stability maps in the $l_c - x_q$ parameter plane. Results are shown only for the first mode. Three different mean velocities were considered: $\bar{u} = 0.5$, 1.0 and 1.5 m/s. The HEX tubes had diameter $d = 3$ mm, and the gap between them was $h_g = 0.3$ mm wide.

The parameters in the $n\tau$-law were chosen such that mode 1 was unstable for all heat source positions between $x = 0$ and $x = L$ if the HEX was absent.

As discussed in section 10.2, the HEX plays two roles from a thermoacoustic point of view: (1) it acts as a heat sink with oscillating heat transfer rate, and (2) it acts as acoustic scatterer. Figure 57(a) shows the stability predictions for the case where both roles of the HEX were taken into account, whereas Figure 57(b) shows the case, where only the oscillating heat transfer rate of the HEX was considered.

Figure 57(a) clearly shows the stabilising effect of the cavity. However, the mean flow seems to have a destabilising effect. This contradicts the earlier finding, shown in Figure 40, that an increase in the mean flow velocity leads to an increase in the size of the stable regions. An explanation for this discrepancy is provided by Figure 57(b), which shows the corresponding

stability maps for the case where the acoustic scattering at the HEX has not been included. In this figure, the regions of instability are (slightly) larger than those in Figure 57(a).

One can conclude from a comparison of Figure 40 (acoustic scattering, no heat transfer oscillations), Figure 57(a) (acoustic scattering and heat transfer oscillations) and Figure 57(b) (heat transfer oscillations, no acoustic scattering) that the two roles of the HEX are in conflict from a stability point of view: the scattering process has a stabilising influence, while the heat transfer oscillations are destabilising. The two roles in combination lead to an enhancement of instability as the mean flow is increased. However, the unstable mode can still be passively controlled in a large range of cavity lengths.

The stability predictions were later extended to the case where the heat transfer rate from the HEX was nonlinear[99] and described by the Heckl correlation.[100] This correlation is a modified version of King's law, which describes the heat release rate from a hot wire in terms of the square root of the velocity. In a Rijke tube, this nonlinearity is known to have a stabilising effect when the oscillations driven by the hot wire gauze reach high amplitudes.

Surendran and Heckl[99] examined the case, where the flame was described by the basic (linear) $n\tau$-law, but the HEX was modelled by the nonlinear Heckl correlation.[100] Their stability predictions revealed that the combustion system became less stable as the amplitude

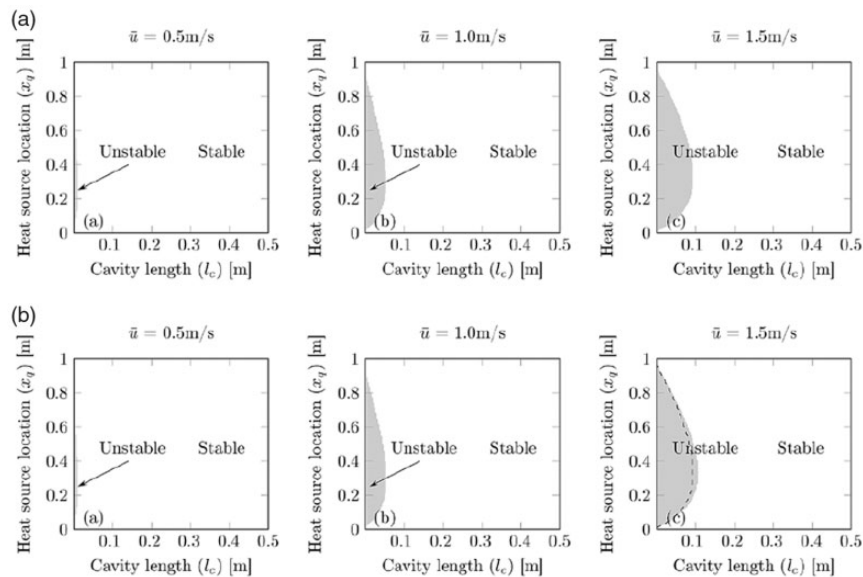**Figure 57.** Stability maps in the $l_c - x_q$ parameter plane for three different inlet velocities $\bar{u}$. (a) HEX modelled as oscillating heat sink and as acoustic scatterer (from Figure 14 in Surendran et al.[93]). (b) HEX modelled as oscillating heat sink only (from Figure 15 in Surendran et al.[93]). The dashed line in the right sub-figure of (b) marks the stability boundary of the sub-figure above it.

increased. An initial interpretation, which will need to be confirmed, is that the HEX tubes become less effective as an active acoustic element while the amplitude increases.

11. Summary and conclusions

Thermoacoustic instabilities are generated by a complex interplay between sound, unsteady combustion and vortical structures in an acoustic resonator. They are a fascinating topic because they are rich in physical phenomena that are still an enigma and waiting to be unravelled. They are also important from a practical point of view because they impede the development of low-pollution combustion systems.

The state-of-the-art in understanding thermoacoustic instabilities has advanced enormously in the last six decades; however, these instabilities are still notoriously hard to predict and control. Various approaches have been and are being used, each with specific advantages and drawbacks:

– Numerical simulations give accurate results, but only for specific geometries, and they tend to be very time-consuming.
– Analytical modelling provides fast predictions, but it relies critically on profound physical insight, which is often not available.
– Experimental approaches provide first-hand information, but unless they are guided by some theoretical model, they are a process of trial and error, which is expensive.

In TANGO, the rationale was to combine these approaches in a coordinated manner so as to take a big step closer to understanding, predicting and controlling thermoacoustic instabilities. TANGO was a Marie Curie Initial Training Network (ITN), which was active during the four-year period 2012–2016 and funded 15 young researchers. The acronym stands for 'Thermoacoustic and Aeroacoustic Nonlinearities in Green combustors with Orifice structures'. As suggested by this title, the two main research themes were thermoacoustics and aeroacoustics. The current paper highlights some of the research results in thermoacoustics (the advances in aeroacoustics are reported in a companion paper by Lopez Arteaga and Bodén[7]).

1. The research in TANGO was interdisciplinary and involved numerical, analytical and experimental approaches. Interactions between these approaches were a dominant feature, and they provided a fertile environment for exploring research topics from different perspectives.

2. Much has been learnt from experimental studies of the transitions from one dynamical state to another as a control parameter was varied. In a test-rig with a swirl-stabilised flame, the equivalence ratio was decreased from stoichiometric to lean values, giving rise successively to combustion noise, intermittent oscillations and thermoacoustic instability. An additional parameter was the amount of turbulence generated by flow restrictors upstream of the flame. Higher turbulence levels were found to disrupt the spatial distribution of the local heat release rate in the combustion chamber, and this caused a fragmentation of the region of positive RI. The consequences were an advanced onset of limit cycle oscillations, and a weakening of their amplitude.
   In a follow-up study involving a bluff-body stabilised turbulent combustor, it was revealed that pattern formation plays a key role in the highly intricate interactions between the wide spatio-temporal scales in the flame, the flow and the acoustic field.
   Experiments with a bluff-body stabilised V-flame revealed that two bifurcations can occur in succession as the flame position was moved from the open end at the top to the closed end at the bottom of a quarter-wave resonator: there was a primary bifurcation from stable flame to low-amplitude limit-cycle oscillations, and a secondary bifurcation to high-amplitude limit-cycle.

3. An early-warning system was developed for annular combustion systems to detect an impending thermoacoustic instability before the amplitude has had time to grow to dangerously high levels. This requires multiple sensors around the circumference of the annulus, whose signals are processed in real time. The early-warning system has been patented and has become a commercial product, which is actively marketed. It has been installed in several industrial-scale gas turbine engines and has demonstrated significant economic advantages: firstly, there is a much reduced risk of hardware damage by high-amplitude thermoacoustic oscillations; secondly, the range of 'safe' operating conditions is enlarged, so there is more flexibility to operate under conditions which are advantageous from an economic point of view and also in terms of emissions.

4. On the theoretical side, a systematic method was developed to turn a FDF (given by a finite number of data points obtained by measurements or numerical simulations) into analytical form. The frequency dependence as well as the amplitude

dependence were represented with good accuracy by entirely analytical functions. In fact, all the main features of a typical FDF were successfully captured: gain of unity at zero frequency, low-pass filter behaviour, and excess gain in a certain low-frequency range.

The analytical expressions derived by this method show the key time-lags for the combustion dynamics in explicit form. This is very useful for gaining physical insight into thermoacoustic instabilities because these respond, as is well known, very sensitively to time-lag changes. The method can also be applied to other transfer functions, such as the transfer function relating the heat absorption rate of a HEX to the flow velocity.

5. The tailored Green's function is a powerful tool to model thermoacoustic instabilities involving compact flames. It is the response by the fluid in a combustion chamber (without unsteady flame) to an impulse point source, and therefore it is a superposition of the chamber modes. The amplitudes and frequencies of these modes are known in analytical form for quasi-1D geometries. In the linear regime, the Green's function approach is equivalent to a network-modelling approach. However, the Green's function approach is primarily performed in the time-domain, and it can also be used for high-amplitude scenarios, where nonlinear effects involving the flame come into play.

In TANGO, the tailored Green's function was used to model several nonlinear processes: The limit cycle amplitudes and frequencies were calculated for various nonlinear heat release laws. Simulations were conducted to mimic experiments where a system parameter was varied and hysteresis was observed; this shed light on an experimental observation of hysteretical behaviour that occurred when the flame position was varied in one direction and then back again. Moreover, the nonlinear interaction between two modes was studied. Finally, the Green's function was combined with flame models obtained from CDF calculations to make fast and accurate stability predictions.

6. Attention has also focussed on ITA modes. A flame governed by a time-lag law generates intrinsic modes, no matter whether it is situated in an acoustic resonator or in an anechoic environment. The time-lag is a key parameter that determines the frequency and growth rate of these modes. They can become unstable, especially if the time-lag is small. The time-lag can be manipulated by changing the time-scale of convective transport phenomena (such as swirl waves or vorticity waves) that affect the flame. For example, decreasing the distance travelled by a swirl wave or increasing the convection speed shifts the resonance frequencies of the ITA modes to higher values.

In an acoustic resonator, an interplay is likely to occur between ITA modes and the resonator modes. This is a potential mechanism for mode-switching. If acoustic damping is added to the resonator, this would control the resonator modes; however, it might be counter-productive in terms of controlling the ITA modes.

7. Fundamental insight was gained into transport phenomena affecting premixed flames: Swirl waves are dispersive; their phase speed depends not only on frequency, but also on the azimuthal component of the mean velocity. The fluctuating part of the velocity vector has components in all three spatial directions (radial, azimuthal and axial in a cylindrical duct); they have a radial profile, which is given by Bessel functions.

The interaction between a laminar premixed flame and a swirl wave is dominated by flame front modulations, leading to fluctuations in the heat release rate. The interaction between a laminar premixed flame and *equivalence ratio* fluctuations is characterised by two time-scales (convective and restoration time-scale); if molecular diffusion is present a third time-scale (diffusion time-scale) comes into the picture. In comparison with perfectly premixed flames, the response to equivalence ratio fluctuations of a *partially* premixed flame can be quite different; this could have significant implications in terms of thermoacoustic instabilities.

8. Deeper understanding was obtained on the effects of a *moving* premixed flame front: temperature inhomogeneities downstream of the flame are associated exclusively with inhomogeneities in the fuel concentration. Moreover, paradoxical conclusions, based on the assumption of a flame front at rest, were resolved.

9. A new, numerically inexpensive, methodology based on the linearised Navier–Stokes equations was developed to make stability predictions for combustions systems that include not only acoustic waves, but also vorticity and entropy waves.

10. The combustion chamber of a condensing boiler typically includes a row of heat absorbing tubes, which form the HEX. Such a combustion chamber is a complex system, comprising the burner deck,

which anchors an array of flames, and one (or more) rows of HEX tubes backed by the outer casing of the combustion chamber. Several physical processes and interactions take place in this configuration. Detailed quantitative models were developed in TANGO and a significant amount of new physical insight was gained.

The HEX tube row, which acts like a slit plate with bias flow, is a very efficient sound absorber in the vicinity of a hard wall (the outer casing of the combustion chamber). This phenomenon has a strong stabilising effect on the complete system and can be exploited for passive instability control. However, the HEX tube row is also an active acoustic element in that it acts as a heat sink with a fluctuating heat transfer; in that role, it may have a stabilising or destabilising effect.

If the HEX tubes are close to the flame, they influence the flame dynamics in ways that are generally undesirable. This is most serious if the flame impinges on the HEX tubes. Then the heat transfer fluctuations of the flame and of the HEX might synchronise in such a way that a pre-existing thermoacoustic instability is exacerbated. Also the capacity of the HEX as a heat absorber is reduced.

In summary, substantial advances were made in the understanding of the web of physical mechanisms and interactions involved in thermoacoustic instabilities. This will, no doubt, help with the design of greener combustion systems. However, many fundamental and practical problems remain and will require further research.

An example for further research on the fundamental front is the nonlinear three-way interaction between flame, sound and vortices. This is responsible for effects, such as intermittency, intrinsic modes and vortex-acoustic lock-on, that have been observed in several combustion test rigs, but the exact physical mechanisms are still not fully understood. On the theoretical front, there is potential to combine CFD simulations with a Green's function approach and to develop hybrid numerical-analytical methods. These would provide a shortcut to avoid the substantial computational expense of purely numerical simulations.

Further developments are anticipated also on the practical front. For example, the early-warning system developed within TANGO for instabilities in an annular combustor could be adapted for application in other combustion systems. Also, the insight gained on the physical effects of a HEX in a combustion chamber could be exploited to design boiler systems that are immune to thermoacoustic instabilities.

ORCID iD

Maria Heckl http://orcid.org/0000-0002-0192-7508

References

1. Candel S. Combustion dynamics and control: progress and challenges. *Proc Combust Inst* 2002; 29: 1–48.
2. Lieuwen TC. Modeling premixed combustion–acoustic wave interactions: a review. *J Propul Power* 2003; 19: 765–781.
3. Huang Y and Yang V. Dynamics and stability of lean-premixed swirl-stabilized combustion. *Prog Energy Combust Sci* 2009; 35: 293–364.
4. Lieuwen TC and Yang V. *Combustion instabilities in gas turbine engines*. Reston, VA: American Institute of Aeronautics and Astronautics, 2005.
5. Poinsot T and Veynante D. *Theoretical and numerical combustion*, 2nd ed. Philadelphia, PA: Edwards, 2005.
6. Culick FEC. Unsteady motions in combustion chambers for propulsion systems. Research and Technology Organisation, NATO, RTO-AG-AVT-039, 2006.
7. Lopez Arteaga I and Bodén H. Advances by the Marie Curie project TANGO in aeroacoustics of structures with orifices. *Int J Spray Combust Dyn*. Under review.
8. Mukherjee N, Heckl M, Bigongiari A, et al. Nonlinear dynamics of a laminar V-flame in a combustor. In: *Proceedings of the 22nd International Congress on Sound and Vibration*, Florence, Italy, 12–16 July 2015.
9. Kabiraj L, Saurabh A, Wahi P, et al. Route to chaos for combustion instability in ducted laminar pre-mixed flames. *Chaos* 2012; 22: paper number 023129.
10. Sujith RI. Influence of high-amplitude oscillations on transport processes. Personal communication, 17 April 2018.

11. Mukherjee NK. Nonlinear dynamics of a V-flame in a combustor. Presentation at the 5th TANGO project meeting, TU Eindhoven, 30–31 March 2015.

12. Ananthkrishnan N, Sudhakar K, Sudershan S, et al. Application of secondary bifurcations to large-amplitude limit cycles in mechanical systems. *J Sound Vibr* 1998; 215: 183–188.

13. George NB, Unni V, Raghunathan M, et al. Effect of varying turbulence intensity on thermoacoustic instability in a partially premixed combustor. In: *Proceedings of the 23rd International Congress on Sound and Vibration*, Athens, Greece, 10–14 July 2016.

14. George NB, Unni VR, Manikandan R, et al. Spatiotemporal dynamics during the transition to thermoacoustic instability: effect of varying turbulence intensities. *Int J Spray Combust Dyn* 2018; 10: 337–350.

15. Komarek T and Polifke W. Impact of swirl fluctuations on the flame response of a perfectly premixed swirl burner. *J Eng Gas Turb Power Trans ASME* 2010; 132: paper number 061503.

16. George NB, Unni V, Raghunathan M, et al. Pattern formation during transition from combustion noise to thermoacoustic instability via intermittency. *J Fluid Mech* 2018; 849: 615–644.

17. Nair V and Sujith RI. Multifractality in combustion noise: predicting an impending combustion instability. *J Fluid Mech* 2014; 747: 635–655.

18. Lieuwen T. Online combustor stability margin assessment using dynamic pressure data. *J Eng Gas Turb Power Trans ASME* 2005; 127: 478–482.

19. Rouwenhorst D, Widhopf-Fenk R and Hermann J. Combustion dynamic monitoring of an azimuthal mode in a can-annular gas turbine (in German). In: *VGB conference on "Gas Turbines and Operation of Gas Turbines"*, Friedrichshafen, Germany, 7-8 June 2017.

20. Rouwenhorst D, Hermann J and Polifke W. Bifurcation study of azimuthal bulk flow in annular combustion systems with cylindrical symmetry breaking. *Int J Spray Combust Dyn* 2017; 9: 438–451.

21. Rouwenhorst D, Hermann J and Polifke W. Online monitoring of thermoacoustic eigenmodes in annular combustion systems based on a state-space model. *J Eng Gas Turb Power* 2017: 139: paper number 021502.

22. Rouwenhorst D, Hermann J and Polifke W. Online monitoring of thermoacoustic eigenmodes in annular combustion systems based on a state space model. In: *Proceedings of the ASME Turbo Expo 2016*, Seoul, South Korea, 13–17 June 2016, paper GT2016-5667.

23. Rouwenhorst D, Hermann J and Polifke W. In situ identification of thermoacoustic stability in annular combustors. *Int J Spray Combust Dyn* 2018; 10: 351–361.

24. Gopinathan SM, Bigongiari A and Heckl MA. Time-domain representation of a flame transfer function with generalised $n\tau$-law featuring a time-lag distribution. In: *Proceedings of the 23rd International Congress on Sound and Vibration*, Athens, Greece, 10–14 July 2016.

25. Gopinathan SM, Bigongiari A and Heckl MA. Flame modelling by transfer function and coupling coefficients featuring time-lag distribution. *Combust Theor Modell*. Under review.

26. Schuller T, Durox D and Candel S. A unified model for the prediction of laminar flame transfer functions: comparisons between conical and V-flame dynamics. *Combust Flame* 2003; 134: 21–34.

27. Gopinathan SM, Bigongiari A, Iurashev D, et al. Nonlinear analytical flame models. *Int J Spray Combust Dyn* 2018; 10: 264–276.

28. Noiray N, Durox D, Schuller T, et al. A unified framework for nonlinear combustion instability analysis based on the flame describing function. *J Fluid Mech* 2008; 615: 139–167.

29. Polifke W. Black-box system identification for reduced order model construction. *Ann Nucl Energy* 2014; 67: 109–128.

30. Bigongiari A, Heckl MA and Iurashev D. Coupled CFD – Green's function approach for prediction of combustion instabilities in gas turbines. In: *Proceedings of the 24th International Congress on Sound and Vibration*, London, UK, 23–27 July 2017.

31. Bigongiari A, Iurashev D, Campa G, et al. Study of the stability of a laboratory swirl burner using a Green's function approach in combination with a flame-speed-closure model. *J Eng Gas Turb Power*. In preparation.

32. Lipatnikov AN and Chomiak J. Turbulent flame speed and thickness: phenomenology, evaluation and application in multi-dimensional simulations. *Prog Energy Combust Sci* 2002; 28: 1–74.

33. Iurashev D, Campa G, Anisimov VV, et al. Three-step approach for prediction of limit cycle pressure oscillations in combustion chambers of gas turbines. *Combust Theor Modell* 2017; 21: 1148–1175.

34. Iurashev D, Campa G and Anisimov VV. Response of swirl-stabilized perfectly premixed flame to high-amplitude velocity excitations. In: *Proceedings of the 23rd International Congress on Sound and Vibration*, Athens, Greece, 10–14 July 2016.

35. Iurashev D. *Numerical and analytical study of combustion instabilities in industrial gas turbines*. PhD Thesis, Ansaldo Energia and University of Genoa, Italy, 2017.

36. Zinn BT and Lores ME. Application of the Galerkin method in the solution of nonlinear axial combustion instability problems in liquid rockets. *Combust Sci Technol* 1971; 4: 269–278.

37. Heckl MA and Howe MS. Stability analysis of the Rijke tube with a Green's function approach. *J Sound Vibr* 2007; 305: 672–688.

38. Crespo Anadón J, Campa G and Bigongiari A. Comparison of Green's function results on the prediction of thermoacoustic instabilities in a gas turbine combustor against experiments. In: *Proceedings of the 23rd International Congress on Sound and Vibration*, Athens, Greece, 10–14 July 2016.

39. Bigongiari A and Heckl MA. A Green's function approach to the rapid prediction of thermoacoustic instabilities in combustors. *J Fluid Mech* 2016; 798: 970–996.

40. Gopalakrishnan EA and Sujith RI. Influence of system parameters on the hysteresis characteristics of a horizontal Rijke tube. *Int J Spray Combust Dyn* 2014; 6: 293–316.

41. Bigongiari A and Heckl M. Analysis of the interaction of thermoacoustic modes with a Green's function approach. *Int J Spray Combust Dyn* 2018; 10: 326–336.

42. Bomberg S, Emmert T and Polifke W. Thermal versus acoustic response of velocity sensitive premixed flames. *Proc Combust Inst* 2015; 35: 3185–3192.

43. Hoeijmakers M, Kornilov V, Arteaga IL, et al. Intrinsic instability of flame-acoustic coupling. *Combust Flame* 2014; 161: 2860–2867.

44. Mukherjee N, Heckl M and Shrira V. Analysis of flame-intrinsic instability in a resonator. In: *Proceedings of the 23rd International Congress on Sound and Vibration*, Athens, Greece, 10–14 July 2016.

45. Mukherjee N and Shrira V. Intrinsic flame instabilities in combustors: analytic description of a 1-D resonator model. *Combust Flame* 2017; 185: 188–209.

46. Mukherjee NK. Analytic description of flame intrinsic instability in 1-D model of open-open combustors with ideal and non-ideal end boundaries. *Int J Spray Combust Dyn* 2018; 10: 287–314.

47. Hosseini N, Kornilov V, Lopez Arteaga I, et al. Intrinsic thermoacoustic modes and their interplay with acoustic modes in a Rijke burner. *Int J Spray Combust Dyn* 2018; 10: 315–325.

48. Albayrak A, Steinbacher T, Komarek T, et al. Convective scaling of intrinsic thermoacoustic eigenfrequencies of a premixed swirl combustor. *J Eng Gas Turb Power* 2018; 140: paper 041510.

49. Silva CF, Emmert T, Jaensch S, et al. Numerical study on intrinsic thermoacoustic instability of a laminar premixed flame. *Combust Flame* 2015; 162: 3370–3378.

50. Iurashev D, Campa G, Anisimov VV, et al. Two-step approach for pressure oscillations prediction in gas turbine combustion chambers. *Int J Spray Combust Dyn* 2017; 9: 424–437.

51. Emmert T, Bomberg S, Jaensch S, et al. Acoustic and intrinsic thermoacoustic modes of a premixed combustor. *Proc Combust Inst* 2017; 36: 3835–3842.

52. Cho JH and Lieuwen T. Laminar premixed flame response to equivalence ratio oscillations. *Combust Flame* 2005; 140: 116–129.

53. Albayrak A and Polifke W. On the propagation velocity of swirl flames in annular flows. In: *Proceedings of the 22nd International Congress on Sound and Vibration*, Florence, Italy, 12–16 July 2015.

54. Albayrak A and Polifke W. Propagation velocity of inertial waves in cylindrical swirling flow. In: *Proceedings of the 23rd International Congress on Sound and Vibration*, Athens, Greece, 10–14 July 2016.

55. Albayrak A, Bezgin DA and Polifke W. Response of a swirl flame to inertial waves. *Int J Spray Combust Dyn* 2018; 10: 277–286.

56. Albayrak A, Blumenthal RS, Ulhaq A, et al. An analytical model for the impulse response of laminar premixed flames to equivalence ratio perturbations. *Proc Combust Inst* 2017; 36: 3725–3732.

57. Albayrak A and Polifke W. An analytical model based on the G-equation for the response of technically premixed flames to perturbations of equivalence ratio. *Int J Spray Combust Dyn* 2018; 10: 103–110.

58. Albayrak A. Swirl wave propagation in an annular duct. Personal communication, 21 August 2018.

59. Blumenthal RS, Subramanian P, Sujith RI, et al. Novel perspectives on the dynamics of premixed flames. *Combust Flame* 2013; 160: 1215–1224.

60. Strobio Chen L, Bomberg S and Polifke W. On the jump conditions for flow perturbations across a moving heat source. In: *Proceedings of the 21st International Congress on Sound and Vibration*, Beijing, China, 13–17 July 2014.

61. Strobio Chen L, Bomberg S and Polifke W. Propagation and generation of acoustic and entropy waves across a moving flame front. *Combust Flame* 2016; 166: 170–180.

62. Strobio Chen L, Steinbacher T, Silva C, et al. On generation of entropy waves by a premixed flame. In: *Proceedings of the ASME Turbo Expo 2016*, Seoul, South Korea, 13–17 June 2016, paper number GT2016-57026.

63. Strobio Chen L. *Scattering and generation of acoustic and entropy waves across moving and fixed heat sources*. PhD thesis, Technische Universität München, Germany, 2016.

64. Chu B-T. On the generation of pressure waves at a plane flame front. In: *4th Symposium (international) on Combustion*, MIT, USA, 1–5 September 1952: 603–612.

65. Chu BT. Stability of systems containing a heat source – the Rayleigh criterion. *NACA Research Memorandum RM 56D27*, 1956, pp.1–25.

66. Dowling AP. The calculation of thermoacoustic oscillations. *J Sound Vibr* 1995; 180: 557–581.

67. Kornilov VN, Rook R, Boonkkamp JHMtT, et al. Experimental and numerical investigation of the acoustic response of multi-slit Bunsen burners. *Combust Flame* 2009; 156: 1957–1970.

68. Nicoud F and Wieczorek K. About the zero Mach number assumption in the calculation of thermoacoustic instabilities. *Int J Spray Combust Dyn* 2009; 1: 67–111.

69. Wieczorek K. *Numerical study of Mach number effects on combustion instability*. PhD Thesis, Université Montpellier II, France, 2010.

70. Na W. *Frequency domain linearized Navier–Stokes equations methodology for aero-acoustic and thermoacoustic simulations*. Licentiate Thesis, KTH Engineering Sciences, Sweden, 2015.

71. Na W, Efraimsson G and Boij S. Prediction of thermoacoustic instabilities in combustors using linearized Navier-Stokes equations in frequency domain. In: *Proceedings of the 22nd International Congress on Sound and Vibration*, Florence, Italy, 12–16 July 2015.

72. Na W, Efraimsson G and Boij S. Numerical prediction of thermoacoustic instabilities with a V-flame. In: *Proceedings of the 23rd International Congress on Sound and Vibration*, Athens, Greece, 10–14 July 2016.

73. Gikadi J. *Prediction of acoustic modes in combustors using linearized Navier–Stokes equations in frequency space.*

PhD Thesis, Technische Universität München, Germany, 2013.

74. Surendran A. Image of a domestic boiler with heat exchanger. Personal communication, 31 May 2018.

75. Teerling J. Photograph of the burner of a Bekaert domestic boiler. Personal communication, 5 July 2012.

76. Dowling AP and Hughes I.J. Sound absorption by a screen with a regular array of slits. *J Sound Vibr* 1992; 156: 387–405.

77. Surendran A and Heckl M. Passive instability control by using a heat exchanger as acoustic sink. In: *Proceedings of the 22nd International Congress on Sound and Vibration*, Florence, Italy, 12–16 July 2015.

78. Surendran A and Heckl MA. Passive instability control by a heat exchanger in a combustor with non-uniform temperature. *Int J Spray Combust Dyn* 2017; 9: 380–393.

79. Hosseini N, Teerling OJ, Kornilov V, et al. Thermoacoustic instabilities in a Rijke tube with heating and cooling elements. In: *Proceedings of the 8th European combustion meeting,* Dubrovnik, Croatia, 18–21 April 2017.

80. Hosseini N, Kornilov V, Teerling OJ, et al. Investigating the effects of a heat exchanger on the thermoacoustics in a Rijke tube. In: *Proceedings of the COMBURA symposium 2016*, Soesterberg, the Netherlands, 5–6 October 2016.

81. Surendran A and Heckl M. Analytical study of a Rijke tube with heat exchanger. In: *Proceedings of the 21st International Congress on Sound and Vibration*, Beijing, China, 13–17 July 2014.

82. Surendran A. *Stability of Rijke tube with heat exchanger and cavity: without mean flow*. Internal Report, Keele University, 10 October 2014.

83. Junger MC and Feit D. *Sound, structures, and their interaction*. Cambridge, MA: MIT Press, 1986.

84. Huang XY and Heckl MA. Transmission and dissipation of sound waves in tube bundles. *Acustica* 1993; 78: 191–200.

85. Surendran A, Heckl MA, Boij S, et al. Aeroacoustic response of an array of tubes with bias flow. In: *Proceedings of the 23rd International Congress on Sound and Vibration*, Athens, Greece, 10–14 July 2016.

86. Surendran A, Heckl MA, Peerlings L, et al. Aeroacoustic response of an array of tubes with and without bias-flow. *J Sound Vibr* 2018; 434: 1–16.

87. Ronneberger D. Experimentelle Untersuchungen zum akustischen Reflexionsfaktor von unstetigen Querschnittsänderungen in einem luftdurchströmten Rohr (Experimental investigations of the acoustic reflection coefficient of discontinuous changes of cross-section in a duct with air flow). *Acustica* 1967; 19: 222–235.

88. Surendran A. *Passive control of thermoacoustic instabilities in idealised combustion systems using heat exchangers*. PhD Thesis, Keele University, UK, 2017.

89. Surendran A, Heckl M, Hosseini N, et al. Use of heat exchanger for passive control of combustion instabilities. In: *Proceedings of the 23rd International Congress on Sound and Vibration*, Athens, Greece, 10–14 July 2016.

90. Surendran A, Heckl MA, Hosseini N, et al. Passive control of instabilities in combustion systems with heat exchanger. *Int J Spray Combust Dyn* 2018; 10: 362–379.

91. Strobio Chen L, Witte A and Polifke W. Thermo-acoustic characterisation of a heat exchanger in cross flow using compressible and weakly compressible numerical simulation. In: *Proceedings of the 22nd International Congress on Sound and Vibration*, Florence, Italy, 12–16 July 2015.

92. Strobio Chen L, Polifke W, Hosseini N, et al. Acoustic scattering behaviour of a 2D flame with heat exchanger in cross-flow. In: *Proceedings of the 23rd International Congress on Sound and Vibration*, Athens, Greece, 10–14 July 2016.

93. Surendran A, Heckl MA, Hosseini N, et al. Passive control of instabilities in combustion systems with heat exchanger [Corrigendum]. *Int J Spray Combust Dyn* 2018; 10: 393–398.

94. Hosseini N, Kornilov V, Teerling OJ, et al. Evaluating thermoacoustic properties of heating appliances considering the burner and heat exchanger as acoustically active elements. *Combust Flame* 2018; 181: 486–495.

95. Hosseini N. *Thermoacoustic instabilities in heating appliances with premixed burner and heat exchanger*. PhD Thesis, Technische Universiteit Eindhoven, the Netherlands, 2019.

96. Hosseini N, Kornilov V, Teerling OJ, et al. Transfer function calculations of segregated elements in a simplified slit burner with heat exchanger. In: *Proceedings of the 22nd International Congress on Sound and Vibration*, Florence, Italy, 12–16 July 2015.

97. Hosseini N, Kornilov V, Teerling OJ, et al. Development of a numerical model for obtaining flame transfer function in a simplified slit burner with heat exchanger. In: *Proceedings of the 21st International Congress on Sound and Vibration*, Beijing, China, 13–17 July 2014.

98. ANSYS Fluent, Release 17.0. Help system, species transport and finite rate chemistry. ANSYS Inc., 2017.

99. Surendran A and Heckl MA. Linear and nonlinear stability predictions for a domestic boiler with a heat exchanger for passive instability control. In: *Proceedings of the 24th International Congress on Sound and Vibration*, London, UK, 23–27 July 2017.

100. Heckl MA. Non-linear acoustic effects in the Rijke tube. *Acustica* 1990; 72: 63–71.

Appendix 1: Notation

a	velocity amplitude
A	flame surface
A_r	pre-exponential factor in Arrhenius law
c	speed of sound
c_p, c_v	specific heats at constant pressure and constant volume
d	diameter of HEX tubes
E	energy
E_a	activation energy
f	frequency (in Hz)
f, g	forward and backward travelling pressure waves
G	Green's function
$h(t)$	impulse response of the flame
h_g	width of gap between HEX tubes
H	Heaviside function
i	imaginary unit
J_0, J_1	Bessel functions of the first kind and of orders 0 and 1
k	wave number
k_r, k_z	radial and axial wave number (in section 7)
l_c	cavity length
L	length of duct or combustion chamber
M	Mach number
n	interaction index
p	pressure
q	local heat release rate
Q	global heat release rate (in W)
r	radial coordinate
r_0	radius of conical flame at its base
R	reflection coefficient
R	specific gas constant (in section 7)
s	entropy per unit mass
S	cross-sectional area of duct
S_L	laminar flame speed
St	Strouhal number
t	time
T	transmission coefficient
$\bar{T}$	mean temperature
$\mathcal{T}(\omega)$	flame transfer function
$\mathcal{T}(\omega, a)$	flame describing function
u	velocity
v_p	phase speed
x_q	location of (compact) flame
x, y, z	cartesian space coordinates
Y	vertical distance
Y_F	mass fraction of fuel in premix
Y_0, Y_1	Bessel functions of the second kind and of orders 0 and 1
α	swirl angle

γ	specific heat ratio
Γ	circulation strength
δ	delta function
ΔH	heat of reaction
Δh_f^0	enthalpy of formation (per unit mass)
$\varepsilon = a/\bar{u}$	relative strength of velocity perturbation
η	spacing of HEX tubes
θ	azimuthal angle
κ	thermal conductivity
λ	wavelength
μ	dynamic viscosity
ξ	impedance ratio
ρ	density
σ	standard deviation in Gauss distribution
τ	time-lag
ϕ	equivalence ratio
φ	velocity potential
ω	angular frequency
$\dot{\omega}_F$	reaction rate

Other notation

u	vector
u'	fluctuating component of the flow quantity u
$\bar{u}$	mean component of the flow quantity u
U	matrix

Abbreviations

BRS burner	beschaufelter Ring-Spalt burner (swirl burner designed at TU Munich)
CFD	computational fluid dynamics
FTF	flame transfer function
FDF	flame describing function
HEX	heat exchanger
IR	impulse response
Section	11 7
ITA mode	intrinsic thermoacoustic mode
ITN	Initial Training Network
LRF	linearised reactive flow
RI	Rayleigh index
rms	root mean square
SPL	sound pressure level

Appendix 2: TANGO participants

Table 4. List of TANGO fellows, their supervisors, host institutions and time in TANGO.

TANGO Fellow	Supervisor	Host institution and country	Time in TANGO	Section in which their work is described
Alp Albayrak	Wolfgang Polifke	TU Munich, Germany	36 months	6.3, 7.1, 7.2, 7.3
Dr Alessandra Bigongiari	Maria Heckl	Keele University, UK	28 months	2.1, 4.1, 4.3, 4.4, 5.3, 5.4, 5.5
Javier Crespo Anadón	Giovanni Campa	Ansaldo Energia, Genova, Italy	10 months	5.2
Nitin Babu George	RI Sujith	IIT Madras, India	12 months	2.2
Dr Sreenath M Gopinathan	Maria Heckl	Keele University, UK	4 months	4.1, 4.2, 4.3, 4.4
Naseh Hosseini	Joàn Teerling	Bekaert Combustion Technology, NL	36 months	6.2, 10.1, 10.3
Dmytro Iurashev	Giovanni Campa	Ansaldo Energia, Genova, Italy	36 months	4.2, 4.3, 4.4, 5.5, 6.4
Nalini Mukherjee	Maria Heckl	Keele University, UK	36 months	2.1, 6.1
Wei Na	Gunilla Efraimsson	KTH, Sweden	26 months	9 and in Lopez Arteaga and Bodén[7]
Luck Peerlings	Susann Boij and Hans Bodén	KTH, Sweden	36 months	see Lopez Arteaga and Bodén[7]
Driek Rouwenhorst	Jakob Hermann	IfTA GmbH, Munich, Germany	36 months	3.1, 3.2
Lin Strobio Chen	Wolfgang Polifke	TU Munich, Germany	36 months	8, 10.2, 10.3, 10.4
Aswathy Surendran	Maria Heckl	Keele University, UK	36 months	10.1, 10.2, 10.4
Muttalip Temiz	Ines Lopez Arteaga	TU Eindhoven, NL	36 months	see Lopez Arteaga and Bodén[7]
Jonathan Tournadre	Paula Martinez-Lera	Siemens Industry Software, Belgium	36 months	see Lopez Arteaga and Bodén[7]

The last column gives the sections in which the work of the individual fellows is described in the current paper.